UNIVERSITY OF CALIFORNIA SAN DIEGO

Luminescent Hydroxyapatite: Degradation Study and Osteogenic Potential

A Dissertation submitted in partial satisfaction of the requirements
for the degree Doctor of Philosophy

in

Materials Science and Engineering

by

Fabian M. Martinez Pallares

Committee in charge:

Professor Olivia A. Graeve, Chair
Professor Renkun Chen
Professor Seth Cohen
Professor Marc Meyers
Professor Padmini Rangamani

2024

The Dissertation of Fabian M. Martinez Pallares is approved, and it is acceptable in quality and form for publication on microfilm and electronically.

University of California San Diego

2024

DEDICATION

I dedicate this dissertation to my dear wife Elisa and our wonderful children, Regina and Roman, whose unwavering support and love have been my foundation.

Elisa, your endless love, support, and patience kept me going, even when things got tough. Regina and Roman, your boundless curiosity, contagious laughter, and endless hugs have been the guiding lights that illuminated even the darkest of research nights. Your encouragement and understanding throughout this journey have been my greatest source of strength, reminding me of the importance of balance and family amidst the rigors of academia. Together, you have been my anchor, grounding me in love and purpose, and for that, I am eternally grateful.

Los amo

TABLE OF CONTENTS

LIST OF FIGURES

LIST OF TABLES

ACKNOWLEDGEMENTS

Firstly, I would like to acknowledge and express my deepest gratitude to my advisor, Professor Olivia Graeve, for her support, invaluable guidance, and boundless patience throughout this journey. Her expertise, encouragement, and dedication have been instrumental in shaping my research and academic growth. I am profoundly grateful for her mentorship and inspiration, which have been pivotal in shaping my academic and professional endeavors.

I am deeply grateful to my mentors, Katya Evdokimenko, Manuel Herrera, and Karla Juarez, whose guidance, support, and expertise have been invaluable throughout my academic journey. Their mentorship has provided me with invaluable insights, skills, and knowledge that have greatly contributed to my growth as a researcher and scholar. Their solid support, encouragement, and willingness to share their expertise have been instrumental in navigating challenges and achieving success in my academic pursuits. I am truly fortunate to have had the opportunity to learn from such dedicated and inspiring mentors and friends.

I'm deeply grateful for the solidarity and support from my friends at UCSD and CNyN. Their encouragement and willingness to collaborate have made my research journey unforgettable. Sharing insights and lending a helping hand, they have created a vibrant and supportive atmosphere that has been invaluable to me.

To Lidia, I deeply appreciate all the moments we've shared together in the lab, collaborating, learning, and growing as researchers. Your dedication, enthusiasm, and openness to exploring new ideas have truly inspired me. It has been an honor to mentor such a talented individual, and I am confident that your passion and commitment will lead to significant achievements in both your academic and professional pursuits.

Finalmente, quiero expresar mi más profundo agradecimiento a mis padres y a mi hermano pequeño por su apoyo incondicional, sabios consejos y enorme esfuerzo, los cuales han sido fundamentales en mi desarrollo personal. Les estoy sinceramente agradecido.

Chapter 2, in part, has been submitted for publication of the material as it may appear in ACS Applied Bio Materials, 2024. Martinez-Pallares, Fabian; Herrera-Zaldivar, Manuel; Graeve, Olivia A. The dissertation author was the primary author of this paper.

Chapter 3, in part, is currently being prepared for submission for publication of the material. Martinez-Pallares, Fabian; Juarez-Moreno, Karla; Vazquez, Lidia; Herrera-Zaldivar, Manuel; Graeve, Olivia A. The dissertation author was the primary researcher and author of this paper.

VITA

2010	Bachelor of Science in Chemical Engineering, Instituto Politecnico Nacional, Mexico.
2011 - 2012	Research and Development Engineer, Zirkonzahn, Italy.
2014	Master of Science in Chemical Engineering, Instituto Politecnico Nacional, Mexico.
2014 - 2015	Graduate Research Assistant, Laboratorio de catálisis y Materiales, Mexico.
2017 - 2023	Associate Lecturer / Teaching Assistant, University of California San Diego.
2022	Micro Master of Business Administration – Rady School of Management, University of California San Diego
2024	Doctor of Philosophy in Materials Science and Engineering, University of California San Diego.

PUBLICATIONS

F. M. Martinez, Manuel Herrera, O. A. Graeve, Decomposition of luminescent hydroxyapatite scaffolds in simulated body fluid, *ACS Applied Bio Materials*, (Submitted in revision).

F. M. Martinez, Karla Juarez-Moreno, Lidia Vazquez, Manuel Herrera, O. A. Graeve, "In vitro differentiation of pre-osteoblast like cells (MC3T3-E1) in luminescent hydroxyapatite" (To be submitted).

Ekaterina Novitskaya, Mahdi Amachraa, **Fabián Martínez-Pallares**, Gómez-Vidales Virginia, Shyue Ping Ong, Manuel Herrera, Olivia A. Graeve, "Barium vacancies as the origin of triboluminescence in hexacelsian ceramics: An ab initio and experimental investigation", *ACS Applied Optical Materials*, (Accepted).

K. Carrera, V. Huerta, V. Orozco, J. Matutes, A. Urbieta, P. Fernández, **F. Martínez**, O.A. Graeve and M. Herrera, "Formation of oxygen vacancies in Cr^{3+}-doped hydroxyapatite nanofibers and their role in generating paramagnetism", *Journal of Materials Chemistry C*, (Submitted in revision).

M.I. Piñón-Muñiz, V.H. Ramos-Sánchez, N. Gutiérrez-Méndez, S.B. Pérez-Vega, J.C. Sacramento-Rivero, C.I. Vargas-Consuelos, **F.M. Martinez**, O.A. Graeve, R.E. Orozco-Mena, A. Quintero-Ramos, M.A. Sánchez-Madrigal, I. Salmerón, "Potential use of Sotol bagasse (Dasylirion spp.) as a new biomass source for liquid biofuels production: Comprehensive characterization and ABE fermentation", *Renewable Energy*, Vol. 212, 2023, pp. 632-643.

https://doi.org/10.1016/j.renene.2023.05.055.

Martínez F. M., Albiter E., Alfaro S., Luna A. L., Colbeau-Justin C., Barrera-Andrade J. M., Remita H., Valenzuela M. A., Hydrogen Production from Glycerol Photoreforming on TiO_2/HKUST-1 Composites: Effect of Preparation Method, *Catalysts*. 2019; 9(4):338. https://doi.org/10.3390/catal9040338

Álvarez-Suarez A. S., López-Maldonado E. A., Graeve O. A., **Martinez-Pallares F.**, Gómez-Pineda L. E., Oropeza-Guzmán M. T., Iglesias A. L., Ng T., Serena-Gómez E., Villarreal-Gómez L. J., "Fabrication of porous polymeric structures using a simple sonication technique for tissue engineering" *Journal of Polymer Engineering*, vol. 37, no. 9, 2017, pp. 943-951. https://doi.org/10.1515/polyeng-2016-0423

E. Albiter, M.A. Valenzuela, S. Alfaro, G. Valverde-Aguilar, **F.M. Martínez-Pallares**, "Photocatalytic deposition of Ag nanoparticles on TiO2: Metal precursor effect on the structural and photoactivity properties", *Journal of Saudi Chemical Society*, 2015, 19(5), 563-573. https://doi.org/10.1016/j.jscs.2015.05.009

ABSTRACT OF THE DISSERTATION

Luminescent Hydroxyapatite: Degradation Study and Osteogenic Potential

by

Fabian M. Martinez Pallares

Doctor of Philosophy in Materials Science and Engineering

University of California San Diego, 2024

Professor Olivia A. Graeve, Chair

This dissertation explores the multifaceted roles of rare-earth doped hydroxyapatite in biomedical applications, bridging the gap between luminescence studies and osteogenic potential in the context of bone tissue engineering and regenerative medicine. In the second chapter, we look into the luminescence properties of terbium, cerium, and europium doped hydroxyapatite scaffolds when immersed in simulated body fluid (SBF) over a four-week period. Our comprehensive study reveals a consistent decrease in luminescence emission intensity across all samples, accompanied by a reduction in the concentration of rare-earth ions within the scaffolds, as confirmed by energy dispersive spectroscopy. Furthermore, fluorescence spectroscopy

demonstrates the translocation of these ions into the SBF, indicating the scaffolds' partial dissolution over time. The employment of rare-earth ions as luminescence markers offers profound insights into apatite formation mechanisms, presenting significant implications for the development of safer and more durable materials in biomedical applications.

Expanding upon the foundational knowledge established in the first and second chapters, the third chapter investigates the osteogenic potential of rare-earth doped hydroxyapatite scaffolds using a murine pre-osteoblastic cell line. This study assesses the effects of ytterbium, terbium, cerium, and europium doping on osteoblast differentiation, gauged by alkaline phosphatase activity and the expression of osteogenic marker genes such as Runx2, OCN, ALP, OPN, and BMP2. Our findings indicate a notable enhancement in differentiation activity with the incorporation of rare-earth elements, with europium and ytterbium doped HAp showing superior performance. Cathodoluminescence spectroscopy further corroborates these results by revealing distinct emission peaks specific to the Eu2+/Eu3+ and Yb2+ ions, underscoring the role of valence state incorporation in augmenting osteoblast differentiation.

Collectively, this dissertation contributes expanding the field of biomaterials by elucidating the dual utility of rare-earth doped hydroxyapatite scaffolds in promoting osteogenic differentiation and providing luminescence-based insights into scaffold behavior in physiological environments. By combining the luminescence stability studies with the exploration of osteogenic potential, our research underscores the importance of integrating multifunctional elements into scaffold design to enhance their performance in bone tissue engineering. The insights garnered from both studies not only pave the way for the development of novel biomaterials but also highlight the potential of rare-earth elements as pivotal components in the advancement of regenerative medicine and biomedical engineering.

INTRODUCTION

In the dynamic field of biomaterials science, which integrates aspects of medicine, biology, chemistry, tissue engineering, and materials science, we have witnessed substantial progress that has enhanced the properties of materials for biomedical use. Among these materials, hydroxyapatite (HAp), an inorganic ceramic, is notable for its biocompatibility, bioactivity, and resemblance to the mineral component of human bone. These characteristics have made HAp a focal point of interest over the past six decades, underlining its value in various medical applications such as bone grafting, dental and orbital implants, drug delivery systems, and as coatings for metal implants.

However, HAp's limitations in degradation rate and bone remodeling restrict its effectiveness in scenarios that demand improved osteoinduction and long-term stability within the body. In response, research efforts have been directed towards enhancing its performance by modifying its properties through dopant incorporation.

Doping HAp with rare-earth elements, a group of metallic elements characterized by an unsaturated 4f electronic structure and their physicochemical properties, has emerged as a promising strategy. Rare-earth elements are of particular interest due to their potential to impart desirable properties to HAp, including a wide range of luminescence (300nm-1400nm), improved biocompatibility, and enhanced bioactivity. Despite the growing interest in rare-earth doped hydroxyapatites, there is a need for comprehensive studies to understand the impact of rare-earth dopants on HAp's lattice structure, their luminescence stability in physiological solutions, and their osteogenic potential.

This dissertation seeks to fill these knowledge gaps by examining the luminescent properties, lattice parameters, hemocompatibility, cell viability, and osteoinductive properties of HAp doped with rare-earth ions, including europium, cerium, terbium, and ytterbium, synthesized through solution combustion synthesis. This research aims to offer a systematic study that contributes to the understanding of how rare-earth doping affects the properties of hydroxyapatite and its suitability for biomedical applications.

Chapter 1 Hydroxyapatite for biomedical applications

1.1 Introduction and background

The evolution of HAp from its first report of bioactivity in the late 60's[1] and its early commercial use in the 80's for implant coating[2] up to the wider field of biomaterials, where it is used today, is amazing. By the late 1980s and early 1990s, that role had evolved with the advent as a coating for metallic implants, e.g., titanium to enhance osteointegration[3], and greatly improved the success rates of implant surgeries by promoting bone growth while minimizing risks of rejection. The appearance of tissue engineering further expanded the applications of HAp to be the scaffold material to bear the growth and differentiation of osteoblasts[4], and thus led the innovations in bone tissue regeneration. Its porous nature, in addition to having an excellent surface area, was used in drug delivery systems, especially in the targeting of bone diseases[5]; this marks a bold stride for the therapeutic field.

The trajectory of its use extended into craniofacial reconstruction[6] and periodontal therapy[7], where its versatility rendered custom-shaped implants for facial reconstruction and filling in the bone defects due to periodontal diseases. Moreover, its entanglement into bioactive papers and textiles for wound dressing and antibacterial use showed its effectiveness outside conventional medicinal applications.[8,9] The invention of nanotechnology and the development of composite materials in which HAp particles are embedded have further improved the features like increased surface area and better mechanical strength, which have shown new potentials for application as load-bearing areas and as a constituent in high-end research for cancer treatment through luminescent and magnetic HAp[10]. During its course of evolution, HAp has ripened from being merely a material for bone grafts to one with very extensive application in advanced biomedical

applications. Its progress is therefore underlined by the ongoing research and technological development that fuels it, hence underlying the potentiality in the healthcare solutions in medical science that HAp possess, indicating a great future for HAp.

1.2 Crystal structure and properties

The crystal structure of HAp, a naturally occurring mineral form of calcium apatite with the chemical formula $Ca_{10}(PO_4)_6(OH)_2$, is both complex and highly ordered, contributing to its unique chemical and physical properties. The HAp crystal structure most frequently encountered is hexagonal, having the $P6_3/m$ space group symmetry. The hexagonal unit cell of HAp normally exhibits lattice parameters a = 9.432 Å and c = 6.881 Å.[11,12,13] These dimensions can slightly vary depending on the ionic substitutions or defects present within the crystal structure. The structure, Figure 1, is built up from columns of Ca^{2+} ions and PO_4^{3-} tetrahedra, with hydroxyl groups (OH^-) occupying specific channels along the c-axis.

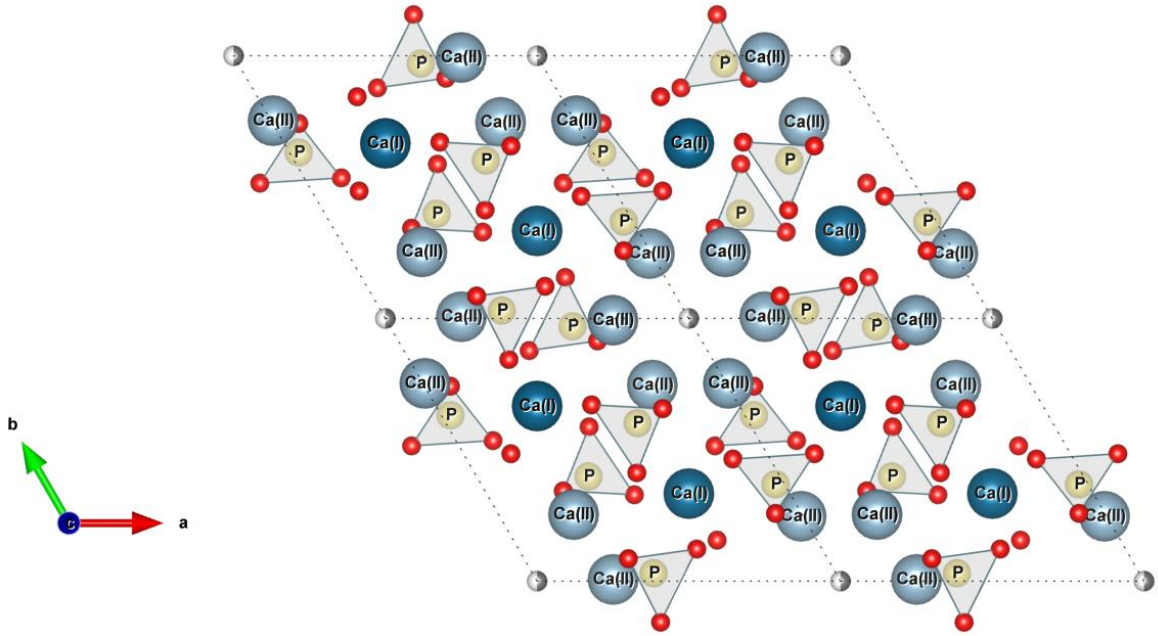

Figure 1. HAp structure along c-axis

There are two distinct sites for calcium ions within the HAp crystal structure, referred to as Ca(I) and Ca(II). The Ca(I) site is nine-coordinated by oxygen atoms, forming a somewhat distorted polyhedron, while the Ca(II) site is seven-coordinated. The phosphate groups are tetrahedrally coordinated and evenly distributed throughout the structure. Hydroxyl ions are aligned in columns parallel to the c-axis, which is a distinctive feature of HAp. These groups are considered active in the bioactivity of HAp as they take part in the process of bonding with bone tissues.[14] Its structure allows for the substitution of its constituent ions with no substantial disorientation of the overall crystal lattice. This capacity to accommodate various ions, for example, carbonate, fluoride, magnesium, strontium, and iron, modify its solubility, mechanical strength, and bioactivity properties.[15,16,17,18,19,20,21,22] As an example, carbonate substitution for phosphate can render HAp more similar to bone mineral.[23]

The vacancies, interstitials, and ionic substitutions present in HAp may cause variations in its crystal size, morphology, and solubility, which in turn makes it a multifaceted material for many applications.

HAp can integrally connect to bone tissue and supports osteointegration, which is one of the most important processes to take place during engraftment of a bone graft. Moreover, osteoconductivity of HAp functions as a scaffold improves the attachment, proliferation, and differentiation of bone cells that are required in regenerating tissues of bones.[24] Pure HAp may have limited osteoinductive properties, but its modifications or combinations with other materials like beta tri-calcium phosphate may induce bone formation at regions which normally are non-bone forming. Figure 2 show the formation of new bone, by immunostaining of BMP-2, in those regions that were closer to the HAp/TCP implant. The differences were related to their location and proximity to the osteogenic environment. [25]

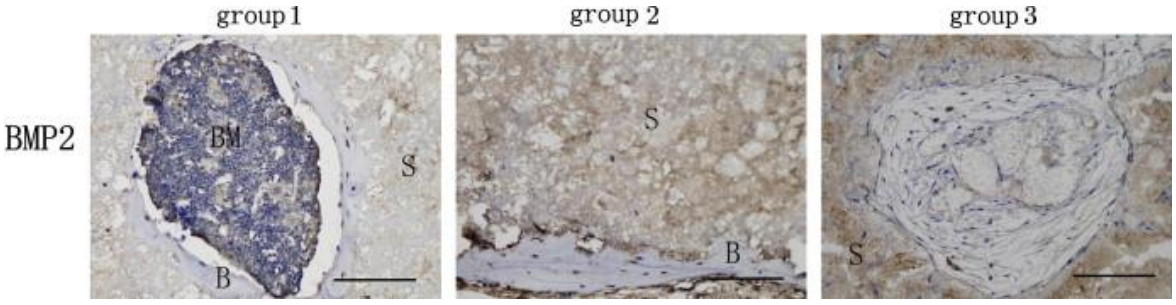

Figure 2. Immunohistochemistry of BMP-2 in decalcified sections of the three groups at 12 weeks.
The brown signals (BMP-2) were detected in osteocyte or mesenchymal cells in the three groups. B, new bone; BM, bone marrow; S, HA/β-TCP scaffold. Bar: 50 μm.[25]

1.3 Synthesis methods

HAp is synthesized through various methods, each tailored for specific properties and applications. Precipitation is a common approach, involving the reaction of calcium and phosphate precursors in a controlled solution to produce HAp with high purity. The precipitation technique is the most widely used and researched method for synthesis of doped HAp. Some common types of ions doped into HAp using precipitation method are shown in Table 1. It was found that the lattice parameters, the biological properties, the degradation rate and absorption were modified by the incorporation of the dopants.

Table 1. Doped HAp using precipitation method[26]

No	Author & Year	Ions Doped	Stirring/ Aging Time	Washing Solvent	Drying/ Calcination	Remarks
1	Kanasan N et al. 2018 [16]	Mg^{2+}	4h/24h at room temp	DI Water	80°C for 24h	The peak intensity and adsorption bands have decreased due to the doping of magnesium.
2	Nagyné-Kovács T et al. 2018 [17]	Sr^{2+}	24h at room temp	DI Water	80°C for 12h	Lattice parameters and the unit cell volume of Sr-doped HAs increased slightly.
3	Wang Y et al. 2016 [18]	Li^{+}	1h at 60°C/48h at room temp	Distilled Water	80°C	Li-HA show higher degradation rate than pure HA.
4	Kulanthaivel S et al. 2016 [19]	Co^{2+}	80°C/24h at 35°C	Distilled Water	55°C for 24h	Co-HA is biocompatible and osteogenic.
5	Ofudje E A et al. 2019 [20]	Zn^{2+}	24h	DI Water	100°C for 24h	The doping causes a decrease in the crystallite size of the HA with an increase in zinc ions concentrations.

The sol-gel method, which transitions a colloidal "sol" into a solid "gel," allows for low-temperature synthesis of homogeneous HAp. Hydrothermal synthesis reacts calcium and phosphate precursors under high pressure and temperature, ideal for creating crystalline, nanosized HAp particles. Although HAp nanoparticles synthesized by sol-gel and hydrothermal methods, as shown in Figure 3, exhibit the same morphology and a similar particle size, in Figure 4 the X-ray diffraction patterns reveal the formation of a second phase in the sample synthesized by sol-gel, which can be attributed to evaporative loss of precursor phosphite phases during specimen preparation and breakdown of the primary HAp phase during calcination.

Mechanical alloying, a solid-state technique using high-energy ball milling, yields HAp with high crystallinity. Microwave processing, a rapid heating method, reduces synthesis time and energy consumption, producing HAp with controlled nanostructures [Figure 5].

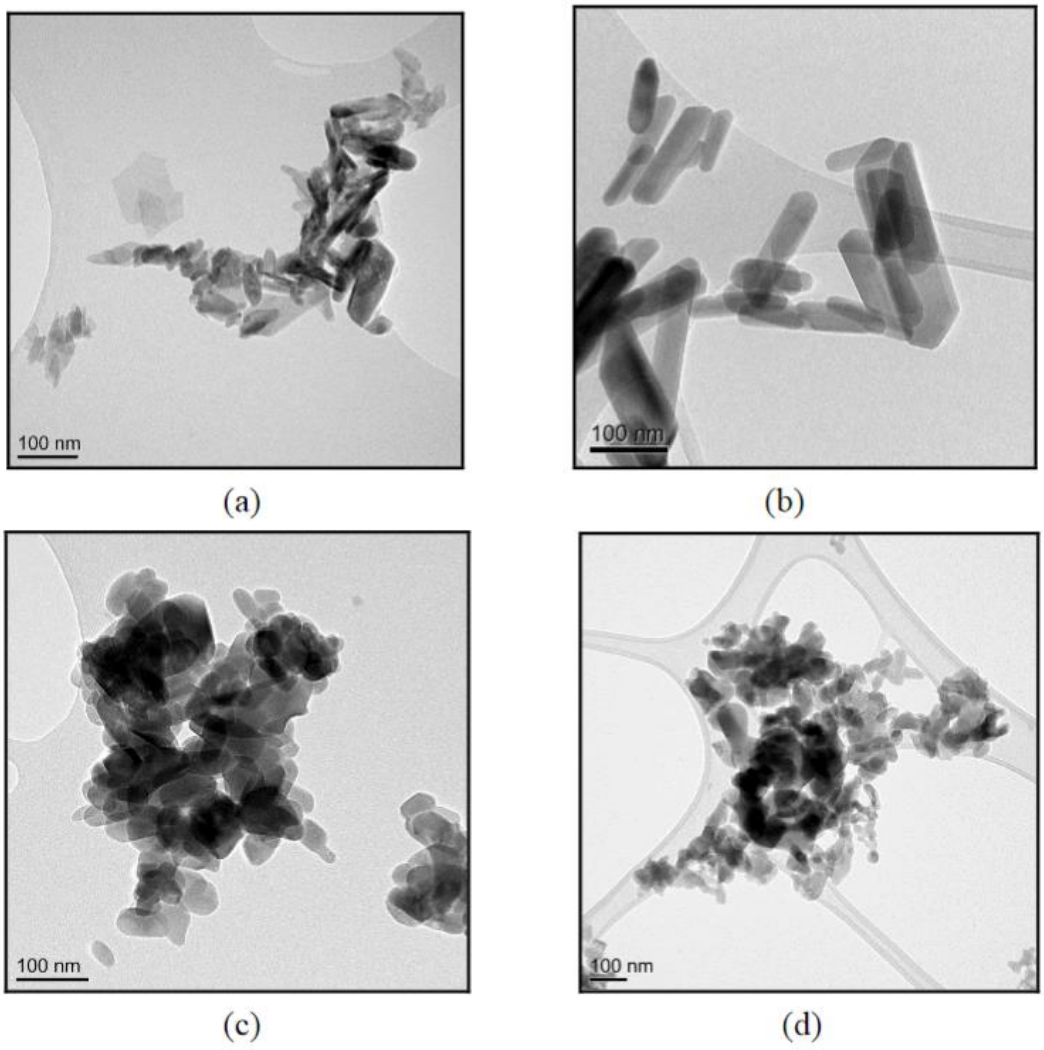

Figure 3. TEM images of (a) Sigma-Aldrich HAp; (b) pH 11 hydrothermal HAp; (c) 500˚C sol-gel HAp and (d) 700˚C sol-gel HAp.

All of the preparations are nano-particulate and neither the hydrothermal nor sol-gel powders exhibit any significant porosity. The sol-gel powders are smaller and more equi-axed than the hydrothermal powders.[27]

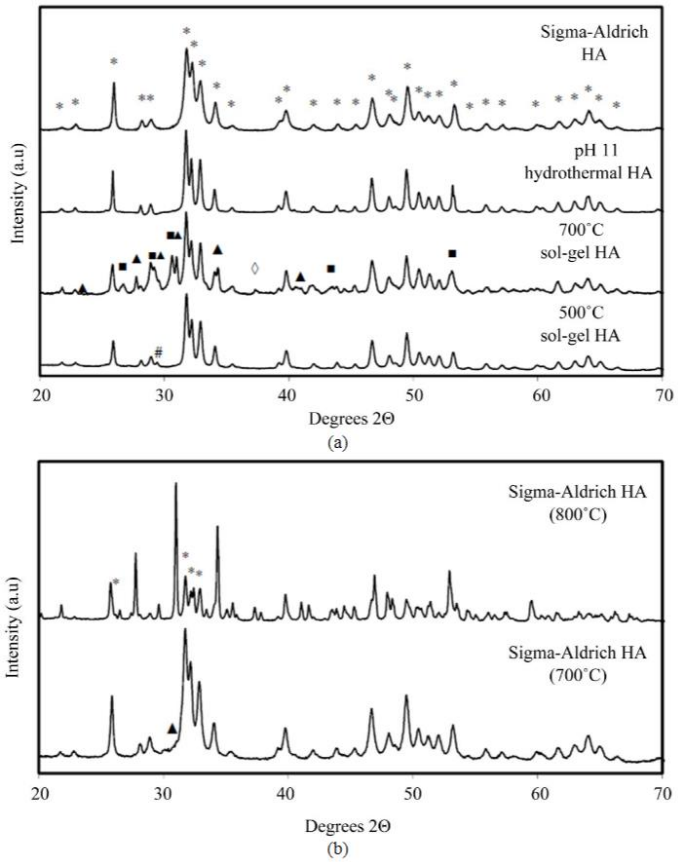

Figure 4. Figure 3. (a) Powder XRD patterns for all HAp samples.
All peaks labelled "*" in the Sigma-Aldrich pattern and all unlabelled peaks in subsequent patterns correspond to a stoichiometric HAp phase[28]. The Sigma-Aldrich and hydrothermal HAp powders show only HAp reflections. Peaks labelled "▲" indicate β-TCP (β-Tricalcium phosphate, Ca3(PO4)2)[29]; peaks labelled "■" indicate DCPA (dicalcium phosphate anhydrate, CaHPO4)[30], peaks labelled "◊" indicate calcium oxide (CaO)[31] and peaks labelled "#" indicate calcium carbonate (CaCO3)[32]. (b) Powder XRD patterns for Sigma-Aldrich HAp decomposed for 1 hour at 700˚C and 800˚C. Unlabelled peaks at 700˚C and peaks labelled "*" at 800˚C correspond to a stoichiometric HAp phase[28]. Unlabelled peaks at 800˚C and peak labelled "▲" at 700˚C indicate β-TCP (β-Tricalcium phosphate, Ca 3(PO4) 2)[29]. At 800˚C most of the HAp has decomposed to β-TCP.[27]

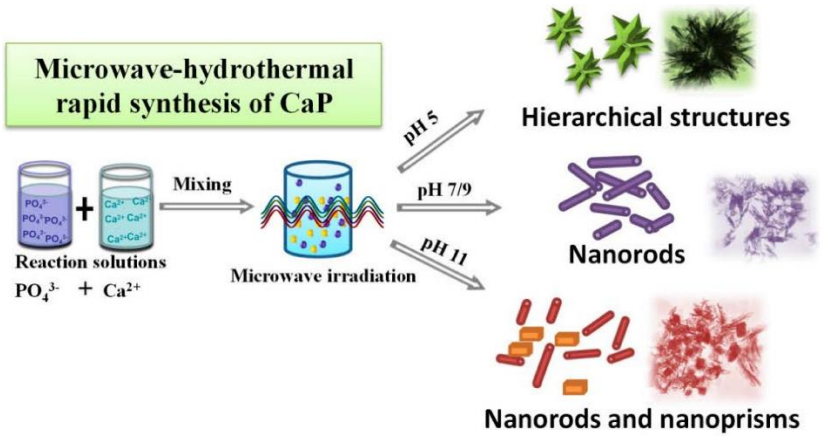

Figure 5. Schematic illustration for the synthesis of calcium phosphate nanostructures with the microwave-assisted hydrothermal method under different pH values. [33]

The biomimetic method mimics natural biomineralization, creating HAp similar to bone apatite using simulated body fluid, suitable for physiological applications. Figure 6 shows the process of HAp formation due to the negative charges of the hydroxyl ion on the surface of the HAp. This process is described more in detail in chapter 2.

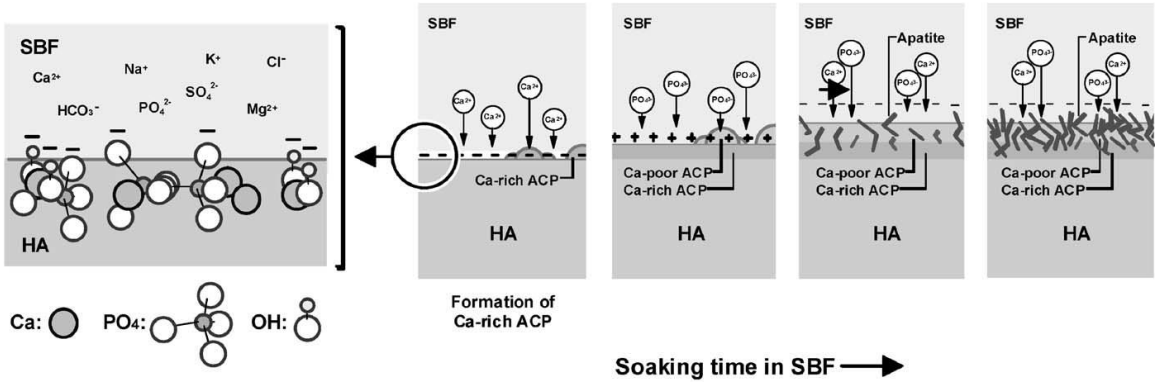

Figure 6. Schematic presentations of the origin of negative charge on the HAp surface and the process of bonelike apatite formation thereon in SBF.[34]

Solution combustion synthesis is a rapid and cost-effective method for producing HAp. It involves the exothermic reaction between metal nitrates, phosphate sources, and a fuel (e.g., carbohydrazide, urea or glycine) in a solution. The combustion process generates high temperatures, facilitating the formation of crystalline HAp nanoparticles with controlled stoichiometry and morphology. This method is advantageous for its simplicity, scalability, and

potential for producing HAp powders. Table 2 displays the results of varying the precursor, temperature, or fuel, primarily affecting the purity of the HAp.

Table 2. Combustion method for synthesis of hydroxyapatite.[35]

Method	Ca/P source	Fuels	Combustion temperature (°C)	Result	Reference
Combustion	$Ca(NO_3)_2$, $(NH_4)_2HPO_4$	Citric acid, succinic acids	185–425	• Ca/P ratio: 1.67 • TCP (major) in mixture of fuel • Single fuel results in carbonated HAp.	[41]
	$Ca(NO_3)_2.4H_20$, $(NH_4)_2HPO_4$	Urea	500	• HAp (major) and β-TCP (minor)	[42]
	$Ca(C_2H_30_2)_2$, $(NH_4)_2HPO_4$	Urea	500	• HAp (ignition temperature of 500 °C at a pH of 7.4 with 30 min) • Small nanorods with smooth edges of diameter 5 ± 2 nm and length ≥ 17 nm	[43]
	$Ca(NO_3)_2$, $NH_4H_2PO_4$, $Ca(OH)_2$	Urea	500	• HAp and CaO phases • Rectangular	[44]

Each method offers distinct advantages, influencing HAp's purity, crystallinity, morphology, and particle size, with ongoing research aimed at enhancing its biomedical applications.

1.4 Cationic substitution

Cationic substitution in HAp is a process that involves replacing calcium ions (Ca^{2+}) in its crystal lattice with other metal ions, significantly altering its physical, chemical, and biological properties. This substitution has become essential in customizing HAp for various applications, allowing the enhancement or introduction of specific functionalities like luminescence, biocompatibility, bioactivity, mechanical strength, and antibacterial properties. Key ions used for substitution include magnesium (Mg^{2+}), which boosts bone formation and HAp bioactivity, however at high concentrations (28.5 mol%) inhibits the osteogenic differentiation-related gene expression[36]; strontium (Sr^{2+}), known for promoting bone growth by promoting the osteoblast differentiation and inhibiting the osteoclast proliferation and differentiation[37]; and zinc (Zn^{2+}), crucial for bone health and imparting antibacterial properties[38]. Additionally, silicon (Si^{4+}) enhances osteoblast activity and the material's bioactivity, while copper (Cu^{2+}), cerium (Ce^{3+}) and silver (Ag^{+}) confer potent antibacterial activities[17,39], making them ideal for infection-prone

implant and graft applications. The strategic incorporation of these ions aims to improve HAp's interaction with natural bone tissue, its load-bearing capacity, and its ability to prevent infections, addressing key challenges in biomedical implantation and regeneration. However, successful cationic substitution requires careful consideration of the substituting ion's ionic radius and valency, concentration, and distribution within the HAp structure to maintain the material's stability and ensure uniform properties. By leveraging cationic substitution, researchers and engineers are equipped to develop HAp-based materials tailored for specific medical applications, from bone regeneration and tissue engineering to antimicrobial interventions, highlighting its significance as a versatile and adaptable biomaterial in advancing healthcare solutions.

1.5 Hydroxyapatite doped with rare-earth elements

HAp substituted with rare-earth elements has emerged as an innovative area of research, unlocking new functionalities and applications for this already versatile biomaterial. Rare-earth elements, such as europium, cerium, terbium, and yttrium have been incorporated into HAp to enhance its properties and utility in various fields, particularly in biomedicine and imaging.[40,41]

1.5.1 Europium doped hydroxyapatite

In the biomedical field, europium-doped materials are used as fluorescent markers for bioassays, microscopy, and in vivo imaging. The sharp emission peaks and long decay times of europium allow for high-resolution imaging and the ability to track biological processes with minimal background interference, a feature not as easily achievable with other rare earth elements. Europium doped hydroxyapatite (HAp:Eu) is utilized for bioimaging and biosensing purposes, where its bright luminescence under specific excitation wavelengths enables high-resolution imaging of cells and tissues, facilitating medical diagnostics and research. This capability is

particularly valuable in tracking and monitoring the behavior of implanted materials within the body, offering insights into biological processes in real time.

Liu et. al.[42] developed and tested a HAp:Eu scaffold for bone regeneration. The study employed a one-step hydrothermal method to synthesize HAp:Eu nanowires and then used a thiol-ene click reaction to create pure net-like scaffolds from these nanowires. These scaffolds were evaluated for their ability to induce osteogenesis. The evaluations involved assessing alkaline phosphatase (ALP) activity, the formation of mineralized nodules, and the expression of bone-related proteins and genes. The results indicated that the net-like HAp:Eu scaffolds were highly effective in inducing osteogenesis. Furthermore, the study highlights the advantage of incorporating Eu^{3+} ions into the scaffolds, which allows for luminescent imaging. This imaging capability enables the relative positioning of scaffolds and cells to be identified, enhancing the monitoring and confirmation of bone repair processes. In vivo experiments demonstrated that the scaffolds not only promoted greater bone defect reconstruction compared to both a control group and a group using $HAp_{@}PCL$ composite scaffolds but also allowed for the monitoring of bone repair through luminescent intensity and area measurements.

Yang et al.'s[43] research on luminescent, bioactive, and mesoporous HAp:Eu nanoparticles reveals their multifunctionality, particularly as drug delivery carriers. The utilization of cationic surfactants as templates results in ordered mesostructures with rod-like morphology, facilitating efficient drug storage and release properties. With diameters ranging from 20 to 40 nm and lengths spanning 100 to 200 nm, these nanoparticles offer precise control over drug delivery kinetics, suggesting promising prospects for targeted therapeutic interventions.

1.5.2 Cerium doped hydroxyapatite

The detailed analysis of cerium cation effects within HAp materials reveals multifaceted benefits and considerations in biomedical applications. Cerium's ionic radius and electronegativity are comparable to those of calcium (Ca^{2+}), enabling it to substitute for calcium in HAp structures. This substitution facilitates cerium's accumulation in bones in small quantities, where it can enhance bone metabolism and the biomimetic formation of HAp, a crucial component of bone and teeth[44].

The incorporation of cerium into HAp materials has been shown to confer several advantageous properties, including the promotion of dental health by preventing cavities and reducing enamel demineralization. Its antioxidant properties contribute to the high thermal-phase stability of the materials. In vitro experiments have demonstrated that cerium doped HAp facilitates biomimetic apatite formation when soaked in simulated body fluid for 2-3 weeks, indicating its potential for enhancing bone regeneration and repair.[45]

Cerium's impact extends to antimicrobial activity, where both Ce^{4+} and Ce^{3+} ions, present in varying proportions depending on the synthesis method, have been reported to inhibit pathogens and stimulate regenerative properties[46,47]. The antibacterial effectiveness of cerium doped HAp has been observed across a wide range of cerium concentrations (1.25–25 at.%), effectively targeting both Gram-positive and Gram-negative bacterial strains without leading to the formation of secondary residual phases. This antibacterial action is attributed to the release of cerium cations, which penetrate the negatively charged bacterial cell membranes, disrupting DNA replication.[47]

However, the antibacterial efficacy and optimal cerium content for inducing such effects vary across studies, with some demonstrating significant antibacterial properties at higher cerium doping levels (>8 at.%)[48] and others noting activity at lower levels (0.3–1.25 at.%).[49,50] These

discrepancies highlight the influence of cerium concentration, preparation method, and the presence of co-dopants like Fe_3O_4[49] nanoparticles or Sr ions[51] on the material's antimicrobial performance.

Cerium doped hydroxyapatite materials offer significant potential in bone and dental applications, owing to their ability to enhance bone metabolism, biomimetic HAp formation, and antimicrobial activity, alongside their applications as fluorescent probes and antioxidant agents. Nonetheless, the balance between antibacterial efficacy, biocompatibility, and potential cytotoxicity must be carefully managed, with the choice of cerium concentration and the incorporation of co-dopants playing critical roles in optimizing the material's performance and safety for biomedical applications.

1.5.3 Terbium doped hydroxyapatite

Terbium, a member of the rare earth element family, exhibits unique optical, magnetic, and electronic properties making it suitable for a wide array of applications across different industries, including glass manufacturing, information technology, polymers, biochemical sensors, and solar energy. Its pervasive use has led to its presence in the environment, ecosystems, and food chains, raising concerns over the need to monitor and understand the exposure to Tb^{3+} ions due to their potential toxicological impacts and other detrimental effects on human health and the environment.[52]

An innovative approach to harness the advantageous properties of terbium, while mitigating its adverse effects, has been demonstrated by Li et al.[53] through the synthesis of terbium doped hydroxyapatite (HAp:Tb). The doping of 20 nm HAp nanoparticles with Tb^{3+} ions not only enhances their luminescent properties under visible light excitation but also retains the fundamental physicochemical characteristics and bioactivity of HAp. Remarkably, even a minimal

doping level significantly boosts the luminescence of these nanoparticles without compromising their inherent qualities. Achieved at room temperature, the synthesis yields nanoparticles with a Tb to (Ca + Tb) atomic ratio of 2:100, capable of emitting constant luminescence when excited by a visible light source (488 nm), showcasing a bright green emission. The high biocompatibility of these HAp:Tb nanoparticles is evidenced by their successful internalization by living cells without inducing toxicity, considering the relatively high lethal dose (50 g. via an oral route LD50PO) of terbium compounds. This feature, combined with the nanoparticles' stable fluorescence, positions HAp:Tb as an excellent inorganic probe for biological studies, particularly in cellular imaging. To explore the broader biomedical applications of HAp:Tb, further studies were conducted on the biological responses of MC3T3-E1 cells to varying concentrations of HAp:Tb nanorods. Figure 7 shows the photoluminescence of the internalized hydroxyapatite in the intracellular cytoplasm under a fluorescent microscope, It is observed that the cells retained their natural morphology. These studies aimed to assess the material's suitability for more extensive biomedical applications, focusing on its interactions with cells and its potential impacts on cell viability, proliferation, and differentiation.

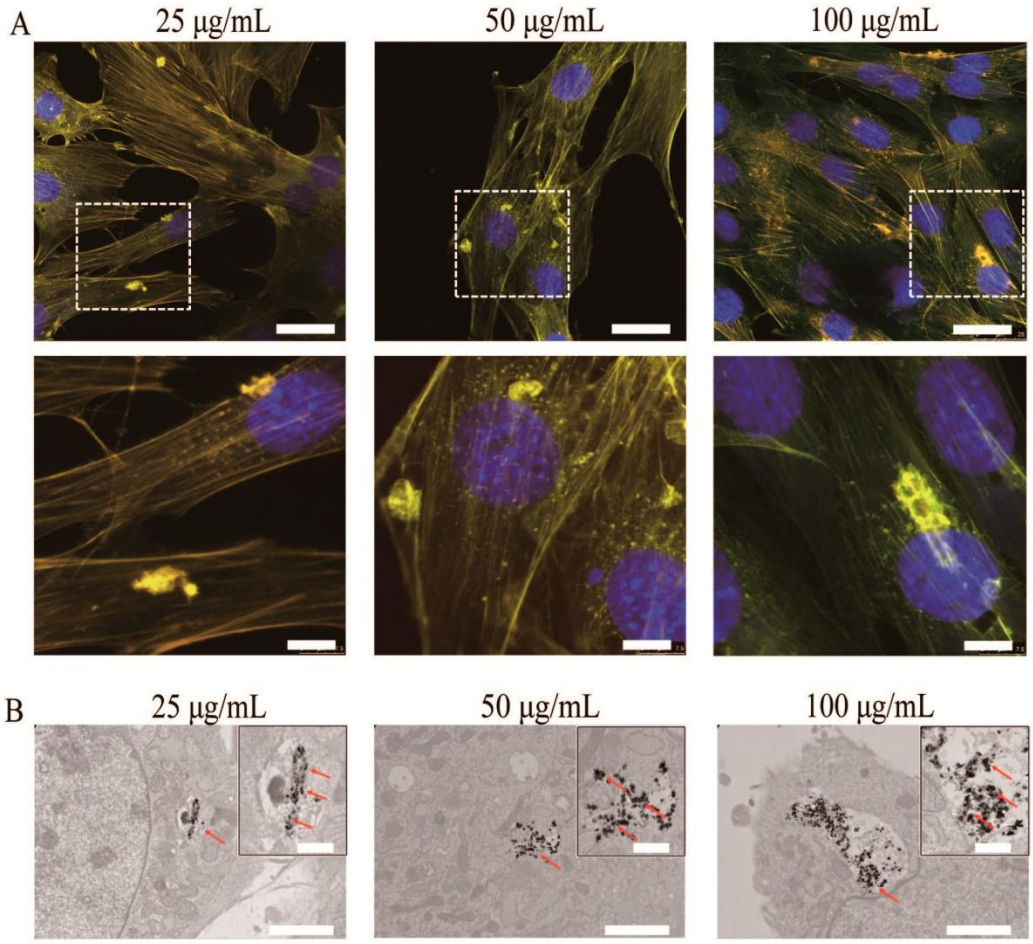

Figure 7. (A) Representative fluorescent images of MC3T3-E1 cells after incubation with HAp:Tb nanorods for 24 h at 37 C. (B) Transmission electron microscopy images of MC3T3-E1 cells after incubation with HA-Tb nanorods.[54]

1.5.4 Ytterbium doped hydroxyapatite

Other lanthanide elements such as cerium, gadolinium, and ytterbium have been identified for their gradual accumulation in human bones, presenting beneficial effects on bone tissue metabolism at low concentrations.[55] These elements, particularly Yb, when incorporated into the bone, can influence cellular activities beneficially. However, it's crucial to note that Yb^{3+} ions, at concentrations exceeding 1×10^{-3} mol/L, may induce apoptosis in rat bone marrow stromal cells (BMSCs), highlighting a concentration-dependent effect on cellular viability.[56] In the other hand, ytterbium doped HAp crystals exhibits enhanced biocompatibility and fluorescent properties,

making them suitable for applications in cell imaging, particularly for tracking and monitoring the chondrogenesis of Bone marrow stromal cells (BMSCs).[57] Yb^{3+} ions possess the unique ability to absorb near-infrared light at approximately 980 nm (~1.26eV), based on the $^2F_{7/2} \rightarrow {}^2F_{5/2}$ transition[58]. This property is beneficial for biomedical imaging applications. However, the absorption peak of Yb^{3+} at 980 nm coincides with the maximum absorption band of water molecules, which can lead to the attenuation of effective incident laser power. This overlap not only reduces the penetration depth in human tissue but also raises concerns about potential cell and tissue damage due to the significant increase in temperature during laser exposure.[59]

1.6 Biocompatibility

Biocompatibility refers to the ability of a material to perform with an appropriate host response when applied within a specific application. In simpler terms, it's the capability of a material to be in contact with a living system without causing any harmful effects. This concept is particularly important in the field of medical devices, implants, and biomaterials, where materials come into direct contact with body tissues and fluids. Biocompatibility ensures that these materials do not elicit any undesirable reactions in the body, such as inflammation, toxicity, or allergic responses, and that they support the intended biological function.

HAp is generally non-toxic to cells, supporting cell adhesion, proliferation, and differentiation, particularly osteoblasts, which are crucial for bone growth and healing. However, performing biocompatibility studies each time a biomaterial is modified is crucial.

Changes in its chemical composition, physical structure, surface properties, or manufacturing process, can significantly alter its interactions with the biological environment. To confirm that a material is biocompatible, a series of assays and tests are conducted, which can be broadly categorized into in vitro (performed outside a living organism), in vivo (conducted in a living

organism), and in some cases, ex vivo (using organs or tissues outside the organism they came from). These tests evaluate different aspects of biocompatibility, including hemocompatibility, cytotoxicity, genotoxicity, immunogenicity, and others described in the ISO 10993.[60]

Cytotoxicity Tests evaluate whether the material is toxic to cells. They are typically performed in vitro using cultured cell lines. The most common method is the MTT assay, which measures cell viability. Figure 8 exhibits the cytotoxicity ionic concentration of various cations. We can observe that the f-block, corresponding to the rare-earth elements, shows the lower cytotoxicity concentrations compere with elements in block d and s.

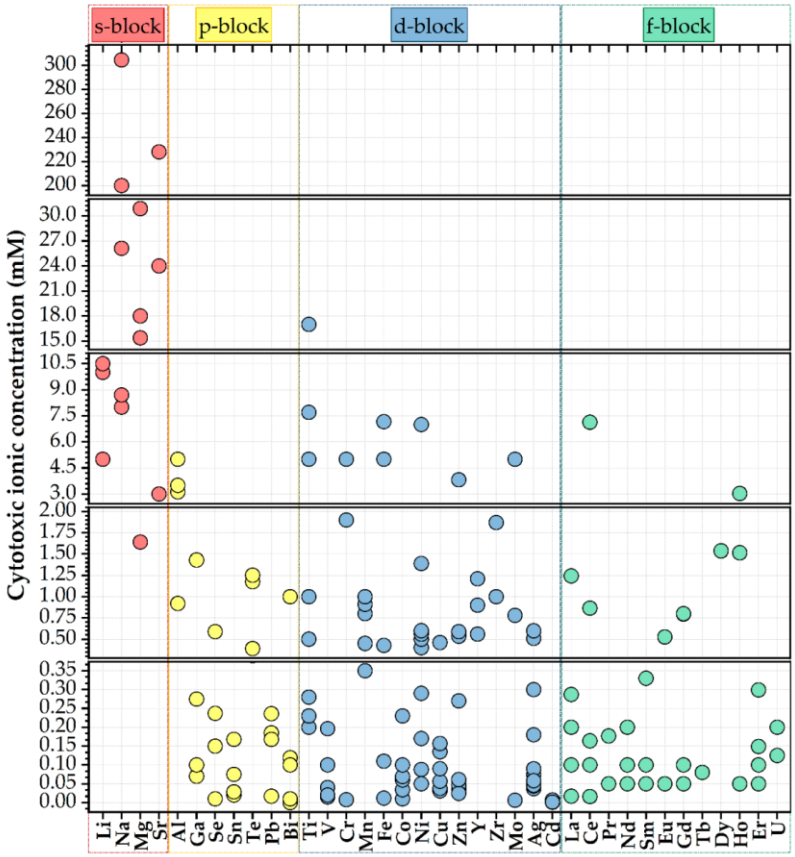

Figure 8. Half-maximal cytotoxic concentration (in mM) of various cationic species.[61]

Sensitization and Irritation Tests are in vivo tests that assess whether the material causes allergic reactions (sensitization) or irritation when in contact with body tissues. Genotoxicity Tests

determine if the material causes genetic damage or mutations. They can be performed in vitro (e.g., Ames test) and in vivo (e.g., micronucleus test). HAp is known for its excellent biocompatibility, rarely triggering a strong immune response, which ensures its good tolerance when implanted in the body. As illustrated in Figure 9, an HAp implant was placed on the iliac crest of rabbits, where it was observed to integrate well without any signs of inflammation or infection. Additionally, certain rare-earth elements like europium are recognized for their anti-inflammatory and antibacterial properties, offering further benefits in such biomedical applications.[62]

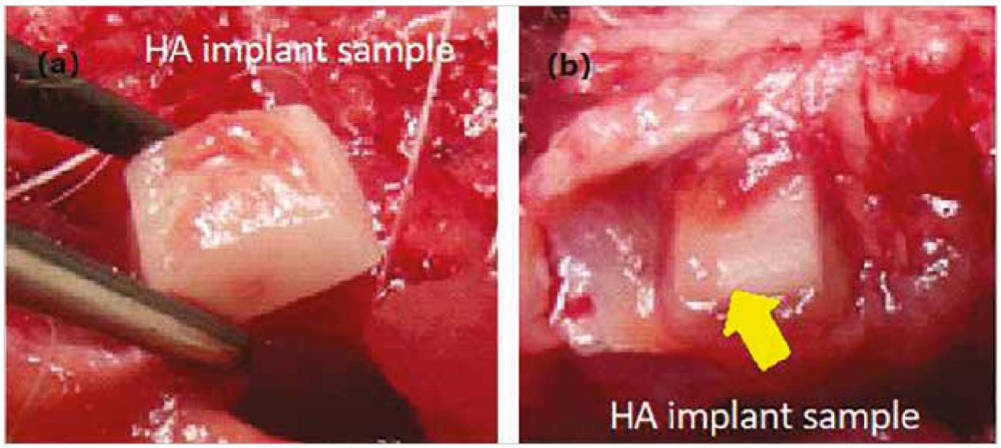

Figure 9. Macroscopic appearance of HAp implant in rabbits' iliac bone after 2weeks. Control group (a), and low-intensity pulsed ultrasound (LIPUS) group (b).[63]

Hemocompatibility tests evaluate materials that come into contact with blood, focusing on their impact on blood components and their potential to induce coagulation or to degrade red blood cells. HAp is notable for its minimal effect on blood coagulation and its lack of hemolytic activity, rendering it suitable for blood-contact applications.[64] Moreover, cerium oxide has demonstrated hemocompatibility, maintaining its compatibility with blood even at higher concentrations (1000 μg/mL).[65]

Degradation and Leachables Testing, assesses how the material degrades over time and whether any degradation products or substances leached from the material are toxic. HAp can

degrade in physiological conditions, but its degradation products are similar to natural bone mineral components, which are biocompatible and can be absorbed or integrated into the body's natural bone tissue.

1.7 Osteoblast differentiation

Osteoblast differentiation is a critical process in the formation and maintenance of bone tissue. It involves the maturation of osteoprogenitor cells into osteoblasts, which are the primary cells responsible for bone formation. This process is essential for skeletal development, growth, and the continuous remodeling of bone throughout an individual's life. Understanding osteoblast differentiation is crucial for developing treatments for bone-related diseases and conditions, such as osteoporosis and fractures.

The process begins with mesenchymal stem cells (MSCs), which are multipotent stromal cells that can differentiate into various cell types, including osteoblasts, chondrocytes (cartilage cells), myocytes (muscle cells), and adipocytes (fat cells). Under specific conditions, MSCs commit to the osteoblast lineage, becoming osteoprogenitor cells. This commitment is influenced by various growth factors and signaling pathways, including bone morphogenetic proteins (BMPs), Wnt signaling, and fibroblast growth factors (FGFs). Osteoprogenitor cells proliferate and form a pool of pre-osteoblasts. These cells are characterized by their high proliferative capacity and the expression of early markers of osteoblast differentiation, such as Runx2 (Runt-related transcription factor 2), which is a critical transcription factor for osteoblast differentiation. Pre-osteoblasts then differentiate into mature osteoblasts, marked by the expression of specific genes and proteins essential for bone formation, including alkaline phosphatase (ALP), osteocalcin, and bone sialoprotein. Runx2, along with other transcription factors such as Osterix (Sp7), plays a pivotal role in this stage by activating the transcription of osteoblast-specific genes.

Osteoblasts are responsible for the production of the bone matrix, which is initially unmineralized (osteoid). The osteoid is composed mainly of Type I collagen and other non-collagenous proteins. Subsequently, osteoblasts secrete alkaline phosphatase, which facilitates the mineralization of the osteoid by depositing calcium and phosphate ions, forming hydroxyapatite crystals that harden the bone. After the bone matrix is formed, osteoblasts can undergo apoptosis (programmed cell death), become bone-lining cells that cover the bone surface and play roles in nutrient exchange, or become embedded in the matrix they secreted, differentiating into osteocytes. Osteocytes are mature bone cells that maintain bone tissue and communicate with other cells in bone through dendritic processes. Despite the prevalence of osteocytes as the primary cellular constituent of bone tissue, our understanding of the transition from osteoblasts to osteocytes remains notably limited.[66]

Osteoblast differentiation is regulated by a complex interplay of systemic hormones (such as parathyroid hormone, vitamin D, and estrogen), local growth factors (including BMPs, Wnt, and FGFs), and mechanical stress. The balance between bone formation by osteoblasts and bone resorption by osteoclasts (bone-degrading cells) is critical for maintaining bone health and integrity.

HAp have been extensively studied for their role in promoting osteoblast differentiation and subsequent bone tissue regeneration due to their chemical composition and surface properties. HAp provides a bioactive surface that can bind proteins and other bioactive molecules from the body fluids, enhancing cell attachment and proliferation. In the other hand, the dissolution of HAp in physiological conditions releases calcium and phosphate ions into the surrounding environment. These ions can increase the local supersaturation, which not only aids in the mineralization process but also activate pathways such as BMP, Wnt, and MAPK leading to the upregulation of

osteoblast-specific transcription factors such as Runx2 and Osterix, which are essential for the differentiation process.

Reference

[1] Hench, L. L.; Splinter, R. J.; Allen, W. C.; Greenlee, T. K. Bonding Mechanisms at the Interface of Ceramic Prosthetic Materials. *J. Biomed. Mater. Res.* **1971**, *5* (6), 117–141. DOI: 10.1002/jbm.820050611.

[2] Abraham, C. M. A Brief Historical Perspective on Dental Implants, Their Surface Coatings and Treatments. *Open Dent. J.* **2014**, *8*, 50–55. DOI: 10.2174/1874210601408010050

[3] Family, R.; Solati-Hashjin, M.; Namjoy Nik, S.; Nemati, A. Surface Modification for Titanium Implants by Hydroxyapatite Nanocomposite. *Caspian J. Intern. Med.* **2012**, *3* (3), 460–465.

[4] Norman, M. E.; Elgendy, H. M.; Shors, E. C.; El-Amin, S. F.; Laurencin, C. T. An In-Vitro Evaluation of Coralline Porous Hydroxyapatite as a Scaffold for Osteoblast Growth. *Clin. Mater.* **1994**, *17* (2), 85–91. DOI: 10.1016/0267-6605(94)90016-7.

[5] Dash, A. K.; Cudworth, G. C. Therapeutic Applications of Implantable Drug Delivery Systems. *J. Pharmacol. Toxicol. Methods* **1998**, *40* (1), 1–12. DOI:10.1016/S1056-8719(98)00027-6

[6] Verret, D. J.; Ducic, Y.; Oxford, L.; Smith, J. Hydroxyapatite Cement in Craniofacial Reconstruction. *Otolaryngol.–Head Neck Surg.* **2005**, *133* (6), 897–899. DOI: 10.1016/j.otohns.2005.09.001.

[7] Kasaj, A.; Röhrig, B.; Zafiropoulos, G.-G.; Willershausen, B. Clinical Evaluation of Nanocrystalline Hydroxyapatite Paste in the Treatment of Human Periodontal Bony Defects – A Randomized Controlled Clinical Trial: 6-Month Results. *J. Periodontol.* **2008**, *79* (3), 394–400. DOI: 10.1902/jop.2008.070378.

[8] Türe, H. Characterization of Hydroxyapatite-Containing Alginate–Gelatin Composite Films as a Potential Wound Dressing. *Int. J. Biol. Macromol.* **2019**, *123*, 878–888. DOI: 10.1016/j.ijbiomac.2018.11.143.

[9] Otsuka, M.; Matsuda, Y.; Yu, D.; Wong, J.; Fox, J. L.; Higuchi, W. I. A Novel Skeletal Drug Delivery System for Anti-Bacterial Drugs Using Self-Setting Hydroxyapatite Cement. *Chem. Pharm. Bull.* **1990**, *38* (12), 3500–3502. DOI: 10.1248/cpb.38.3500

[10] Sánchez Lafarga, A. K.; Pacheco Moisés, F. P.; Gurinov, A.; Ortiz, G. G.; Carbajal Arízaga, G. G. Dual Responsive Dysprosium-Doped Hydroxyapatite Particles and Toxicity Reduction After Functionalization with Folic and Glucuronic Acids. *Mater. Sci. Eng. C* **2015**, *48*, 541–547. DOI: 10.1016/j.msec.2014.12.033.

[11] Corno, M.; Busco, C.; Civalleria, B.; Ugliengo, P. Periodic ab initio Study of Structural and Vibrational Features of Hexagonal Hydroxyapatite Ca10(PO4)6(OH)2. *Phys. Chem. Chem. Phys.* **2006**, *8*, 2464–2472.

[12] Ma, G.; Liu, X. Hydroxyapatite: Hexagonal or Monoclinic? *Cryst. Growth Des.* **2009**, *9*, 2991–2994.

[13] Elliott, J. C.; Mackie, P. E.; Young, R. A. Monoclinic Hydroxyapatite. *Science* **1973**, *180* (4090), 1055–1057

[14] Perez-Moreno, A.; Reyes-Peces, M. d. l. V.; de los Santos, D. M.; Pinaglia-Tobaruela, G.; de la Orden, E.; Vilches-Pérez, J. I.; Salido, M.; Piñero, M.; de la Rosa-Fox, N. Hydroxyl Groups Induce Bioactivity in Silica/Chitosan Aerogels Designed for Bone Tissue Engineering. An In Vitro Model for the Assessment of Osteoblasts Behavior. *Polymers* **2020**, *12*, 2802. DOI: 10.3390/polym12122802

[15] Landi, E.; Celotti, G.; Logroscino, G.; Tampieri, A. Carbonated Hydroxyapatite as Bone Substitute. *J. Eur. Ceram.* **2003**, *23*, 2931–2937. DOI: 10.1016/S0955-2219(03)00304-2

[16] Tredwin, C. J.; Young, A. M.; Abou Neel, E. A.; Georgiou, G.; Knowles, J. C. Hydroxyapatite, Fluor-Hydroxyapatite and Fluorapatite Produced via the Sol-Gel Method: Dissolution Behaviour and Biological Properties After Crystallization. *J. Mater. Sci. Mater. Med.* **2014**, *25*, 47–53. DOI: 10.1007/s10856-013-5050-y

[17] Ressler, A.; Žužić, A.; Ivanišević, I.; Kamboj, N.; Ivanković, H. Ionic Substituted Hydroxyapatite for Bone Regeneration Applications: A Review. *Open Ceram.* **2021**, *6*, 100122. DOI: 10.1016/j.oceram.2021.100122.

[18] Bauer, L.; Antunović, M.; Rogina, A.; Ivanković, M.; Ivanković, H. Bone-Mimetic Porous Hydroxyapatite/Whitlockite Scaffolds: Preparation, Characterization and Interactions with Human Mesenchymal Stem Cells. *J. Mater. Sci.* **2021**, *56*, 3947–3969. DOI: 10.1007/s10853-020-05489-3

[19] Pilmane, M.; Salma-Ancane, K.; Loca, D.; Locs, J.; Berzina-Cimdina, L. Strontium and Strontium Ranelate: Historical Review of Some of Their Functions. *Mater. Sci. Eng. C* **2017**, *78*, 1222–1230. DOI: 10.1016/j.msec.2017.05.042

[20] Panseri, S.; Cunha, C.; D'Alessandro, T.; Sandri, M.; Giavaresi, G.; Marcacci, M.; Hung, C. T.; Tampieri, A. Intrinsically superparamagnetic Fe-hydroxyapatite nanoparticles positively influence osteoblast-like cell behaviour. *J. Nanobiotechnol.* **2012**, *10*, 32. DOI: 10.1186/1477-3155-10-32

[21] Farzadi, A.; Bakhshi, F.; Solati-Hashjin, M.; Asadi-Eydivand, M.; abu Osman, N. A. Magnesium incorporated hydroxyapatite: synthesis and structural properties characterization. *Ceram. Int.* **2014**, *40*, 6021-6029. DOI: 10.1016/j.ceramint.2013.11.051

[22] Matsunaga, K. First-principles study of substitutional magnesium and zinc in hydroxyapatite and octacalcium phosphate. *J. Chem. Phys.* **2008**, *128*, 245101. DOI: 10.1063/1.2940337

[23] Siddiqi, S. A.; Azhar, U. Carbonate substituted hydroxyapatite. In *Handbook of Ionic Substituted Hydroxyapatites*; Khan, A. S.; Chaudhry, A. A., Eds.; Woodhead Publishing, 2020; pp 149-173. DOI: 10.1016/B978-0-08-102834-6.00006-9

[24] Lovati, A. B.; Lopa, S.; Recordati, C.; Talò, G.; Turrisi, C.; Bottagisio, M.; Losa, M.; Scanziani, E.; Moretti, M. In Vivo Bone Formation Within Engineered Hydroxyapatite Scaffolds in a Sheep Model. *Calcif Tissue Int.* **2016**, *99*(2), 209-223. DOI: 10.1007/s00223-016-0140-8.

[25] Cheng, L.; Ye, F.; Yang, R.; Lu, X.; Shi, Y.; Li, L.; Fan, H.; Bu, H. Osteoinduction of hydroxyapatite/beta-tricalcium phosphate bioceramics in mice with a fractured fibula. *Acta Biomater.* **2010**, *6*(4), 1569-1574. DOI: 10.1016/j.actbio.2009.10.050..

[26] Baskaran, T.; Mohammad, N. F.; Md Saleh, S. S.; Mohd Nasir, N. F.; Mohd Daud, F. D. Synthesis Methods of Doped Hydroxyapatite: A Brief Review. *J. Phys.: Conf. Ser.* **2021**, *2071*(1), 012008. DOI: 10.1088/1742-6596/2071/1/012008.

[27] Bilton, M.; Milne, S. J.; Brown, A. P. Comparison of Hydrothermal and Sol-Gel Synthesis of Nano-Particulate Hydroxyapatite by Characterisation at the Bulk and Particle Level. *Open J. Inorg. Non-Met. Mater.* **2012**, *2*(1), 17043. DOI: 10.4236/ojinm.2012.21001

[28] Sudarsanan, K.; Young, R. A. Significant Precision in Crystal Structural Details: Holly Springs Hydroxyapatite. *Acta Cryst.* **1969**, *25*(8), 1534-1543. DOI: 10.1107/S0567740869004298

[29] Dickens, B.; Brown, W. E. Crystallographic Studies of Role of Mg as a Stabilizing Impurity in Beta-Ca3(PO4)2.1. Crystal-Structure of Pure Beta-Ca3(PO4)2. *J. Solid State Chem.* **1974**, *10*(3), 232-248. DOI: 10.1016/0022-4596(74)90030-9

[30] Catti, M.; Ferraris, G.; Filhol, A. Hydrogen-Bonding in Crystalline State—CaHPO4 (Monetite), P1bar or P1 -Novel Neutron-Diffraction Study. *Acta Crystallogr., Sect. B: Struct. Sci.* **1977**, *33*(4), 1223-1229. DOI: 10.1107/S0567740877005706

[31] Oftedal, I. The Lattice Constants of CaO, CaSe, CaS, CaTe. *Z. Phys. Chem. (Leipzig)* **1927**, *128*, 154-158.

[32] Swanson, H. E.; Fuyat, R. K. Calcite. *Stand. X-Ray Diffr. Patterns* **1953**, *539*, 52-53

[33] Cai, Z.-Y.; Peng, F.; Zi, Y.-P.; Chen, F.; Qian, Q.-R. Microwave-Assisted Hydrothermal Rapid Synthesis of Calcium Phosphates: Structural Control and Application in Protein Adsorption. *Nanomaterials* **2015**, *5*, 1284-1296. DOI: 10.3390/nano5031284

[34] Kim, H.-M.; Himeno, T.; Kokubo, T.; Nakamura, T. Process and kinetics of bonelike apatite formation on sintered hydroxyapatite in a simulated body fluid. *Biomaterials* **2005**, *26*(21), 4366–4373. DOI: 10.1016/j.biomaterials.2004.11.022

[35] Mohd Pu'ad, N. A. S.; Abdul Haq, R. H.; Mohd Noh, H.; Abdullah, H. Z.; Idris, M. I.; Lee, T. C. Synthesis method of hydroxyapatite: A review. *Mater. Today: Proc.* **2020**, *29*(1), 233-239. DOI: 10.1016/j.matpr.2020.05.536..

[36] Kozuma, W.; Kon, K.; Kawakami, S.; Bobothike, A.; Iijima, H.; Shiota, M.; Kasugai, S. Osteoconductive potential of a hydroxyapatite fiber material with magnesium: In vitro and in vivo studies. *Dent. Mater. J.* **2019**, *38*(5), 771-778. DOI: 10.4012/dmj.2018-333

[37] Bonnelye, E.; Chabadel, A.; Saltel, F.; Jurdic, P. Dual effect of strontium ranelate: Stimulation of osteoblast differentiation and inhibition of osteoclast formation and resorption in vitro. *Bone* **2008**, *42*(1), 129-138. DOI: 10.1016/j.bone.2007.08.043

[38] Nenen, A.; Maureira, M.; Neira, M.; Orellana, S. L.; Covarrubias, C.; Moreno-Villoslada, I. Synthesis of antibacterial silver and zinc doped nano-hydroxyapatite with potential in bone tissue engineering applications. *Ceramics International* **2022**, *48*(23, Part A), 34750-34759. DOI: 10.1016/j.ceramint.2022.08.064

[39] Lin, Y.; Yang, Z.; Cheng, J. Preparation, Characterization and Antibacterial Property of Cerium Substituted Hydroxyapatite Nanoparticles. *J. Rare Earths* **2007**, *25*(4), 452-456. DOI: 10.1016/S1002-0721(07)60455-4

[40] Coelho, J.; Hussain, N. S.; Gomes, P. S.; Garcia, M. P.; Lopes, M. A.; Fernandes, M. H.; Santos, J. D. Development and characterization of lanthanides doped hydroxyapatite composites for bone tissue application. In *Current Trends on Glass and Ceramic Materials*; Nandyala, S. H.; Santos, J. D., Eds.; Bentham Science Publishers, 2013; pp 87–115

[41] Doat, A.; Fanjul, M.; Pelle, F.; Hollande, E.; Lebugle, A. Europium-doped bioapatite: a new photostable biological probe, internalizable by human cells. *Biomaterials* **2003**, *24*, 3365–3371

[42] Liu, M.; Shu, M.; Yan, J.; Liu, X.; Wang, R.; Hou, Z.; Lin, J. Luminescent net-like inorganic scaffolds with europium-doped hydroxyapatite for enhanced bone reconstruction. *Nanoscale*, **2021**, 13, 1181-1194 DOI: 10.1039/D0NR05608A.

[43] Yang, P.; Quan, Z.; Li, C.; Kang, X.; Lian, H.; Lin, J. Bioactive, luminescent and mesoporous europium-doped hydroxyapatite as a drug carrier. *Biomaterials*, **2008**, 29, 4341–4347 DOI: 10.1016/j.biomaterials.2008.07.042

[44] Zhou, L.; Tang, S.; Yang, L.; Huang, X.; Zou, L.; Huang, Y.; Dong, S.; Zhou, X.; Yang, X. Cerium ion promotes the osteoclastogenesis through the induction of reactive oxygen species. *J. Trace Elem. Med. Biol.* **2019**, *52*, 126-135. DOI: 10.1016/j.jtemb.2018.12.006.

[45] Heshmatpour F., Lashteneshaee S.H., Samadipour M. Study of in vitro bioactivity of nano hydroxyapatite composites doped by various cations. *J. Inorg. Organomet. Polym. Mater.* **2018**, 28, 2063–2068. DOI: 10.1007/s10904-018-0864-1

[46] Yuan, Q.; Qin, C.; Wu, J.; Xu, A.; Zhang, Z.; Liao, J.; Lin, S.; Ren, X.; Zhang, P. Synthesis and characterization of cerium-doped hydroxyapatite/polylactic acid composite coatings on metal substrates. *Mater. Chem. Phys.* **2016**, *182*, 365–371. DOI: 10.1016/j.matchemphys.2016.07.044

[47] Priyadarshini, B.; Anjaneyulu, U.; Vijayalakshmi, U. Preparation and characterization of sol-gel derived Ce4+ doped hydroxyapatite and its in vitro biological evaluations for orthopedic applications. *Mater. Des.* **2017**, *119*, 446–455. DOI: 10.1016/j.matdes.2017.01.095

[48] Lin, Y.; Yang, Z.; Cheng, J. Preparation, Characterization and Antibacterial Property of Cerium Substituted Hydroxyapatite Nanoparticles. *J. Rare Earths.* **2007**, *25*, 452–456. DOI: 10.1016/S1002-0721(07)60455-4

[49] Baskaran, P.; Udduttula, A.; Uthirapathy, V. Development and characterisation of novel Ce-doped hydroxyapatite–Fe3O4 nanocomposites and their in vitro biological evaluations for biomedical applications. *IET Nanobiotechnol.* **2018**, *12*, 138–146. DOI: 10.1049/iet-nbt.2017.0029

[50] Ciobanu, C.; Popa, C.; Predoi, D. Cerium doped hydroxyapatite nanoparticles synthesized by coprecipitation method. *J. Serb. Chem. Soc.* **2016**, *81*, 433–446. DOI: 10.2298/JSC150824007C

[51] Sundarabharathi, L.; Chinnaswamy, M.; Ponnamma, D.; Parangusan, H.; Al-Maadeed, M. A. A. Investigation of antimicrobial properties and in-vitro bioactivity of Ce3+-Sr2+ dual-substituted nano hydroxyapatites. *J. Am. Ceram. Soc.* **2018**. DOI: 10.1111/jace.15866

[52] Chen, Q.; Zuo, J.; He, X.; Mo, X.; Tong, P.; Zhang, L. Enhanced fluorescence of terbium with thiabendazole and application in determining trace amounts of terbium and thiabendazole. Talanta **2017**, 162, 540–546. DOI: 10.1016/j.talanta.2016.10.036

[53] Li, L.; Liu, Y.; Tao, J.; Zhang, M.; Pan, H.; Xu, X.; Tang, R. Surface modification of hydroxyapatite nanocrystallite by a small amount of terbium provides a biocompatible fluorescent probe. J. Phys. Chem. C **2008**, 112, 12219–12224. DOI: 10.1021/jp8026463

[54] Wei, Y.; He, Y.; Li, X.; Chen, H.; Deng, X. Cellular Uptake and Delivery-Dependent Effects of Tb3+-Doped Hydroxyapatite Nanorods. *Molecules*, **2017**, 22, 1043.

[55] Zaichick, S.; Zaichick, V.; Karandashev, V.; Nosenko, S. Accumulation of rare earth elements in human bone within the lifespan. *Metallomics* **2011**, *3*, 186-194. DOI: 10.1016/j.cej.2020.124166

[56] C. Dai, S. Chen, C. Wang, L. Zhang, K. Ge, J. Zhang Ytterbium ion promotes apoptosis of primary mouse bone marrow stromal cells? *J. Rare Earth*, **2015**, 33, 445-452.

[57] X. Hu, J. Zhu, X. Li, X. Zhang, Q. Meng, L. Yuan, J. Zhang, X. Fu, X. Duan, H. Chen, Y. Ao Dextran-coated fluorapatite crystals doped with Yb3+/Ho3+ for labeling and

tracking chondrogenic differentiation of bone marrow mesenchymal stem cells in vitro and in vivo. *Biomaterials*, **2015**, 52, 441-451.

[58] Zavala, L. A.; Fernández, P.; Novitskaya, E.; Díaz, J. N.; Herrera, M.; Graeve, O. A. Interconfigurational and intraconfigurational transitions of Yb2+ and Yb3+ ions in hydroxyapatite: A cathodoluminescence study. *Acta Mater.* **2017**, *135*, 35-43. DOI: 10.1016/j.actamat.2017.06.003

[59] H. Dong, S.R. Du, X.Y. Zheng, G.M. Lyu, L.D. Sun, L.D. Li, P.Z. Zhang, C. Zhang, C.H. Yan Lanthanide nanoparticles: from design toward bioimaging and therapy. *Chem. Rev.* **2015**, 115, 10725-10815.

[60] ISO 10993. Biological evaluation of medical devices. International Organization for Standardization, Geneva, Switzerland.

[61] Tite, T.; Popa, A.-C.; Balescu, L. M.; Bogdan, I. M.; Pasuk, I.; Ferreira, J. M. F.; Stan, G. E. Cationic Substitutions in Hydroxyapatite: Current Status of the Derived Biofunctional Effects and Their In Vitro Interrogation Methods. *Materials* **2018**, *11*, 2081. DOI: 10.3390/ma11112081

[62] Luo, M.; Wang, M.; Niu, W.; Chen, M.; Cheng, W.; Zhang, L.; Xie, C.; Wang, Y.; Guo, Y.; Leng, T.; Zhang, X.; Lin, C.; Lei, B. Injectable self-healing anti-inflammatory europium oxide-based dressing with high angiogenesis for improving wound healing and skin regeneration. *Chem. Eng. J.* **2021**;412. DOI: 10.1016/j.cej.2021.128471.

[63] Kobayashi, M. Enhancement of osseointegration of hydroxyapatite implants by Low-Intensity Ultrasound Irradiation. *J. Osseointegr.* **2020**, *12*(4), 722-729

[64] Ooi, C. H.; Ling, Y. P.; Abdullah, W. Z.; Mustafa, A. Z.; Pung, S. Y.; Yeoh, F. Y. Physicochemical evaluation and in vitro hemocompatibility study on nanoporous hydroxyapatite. *J. Mater. Sci. Mater. Med.* **2019**, *30*(4), 44. DOI: 10.1007/s10856-019-6247-5. PMID: 30929088

[65] Ioannou, M.E.; Pouroutzidou, G.K.; Chatzimentor, I.; Tsamesidis, I.; Florini, N.; Tsiaoussis, I.; Lymperaki, E.; Komninou, P.; Kontonasaki, E. Synthesis and Characterization of Cerium Oxide Nanoparticles: Effect of Cerium Precursor to Gelatin Ratio. *Appl. Sci.* **2023**, *13*, 2676. https://doi.org/10.3390/app13042676

[66] Franz-Odendaal, T. A.; Hall, B. K.; Witten, P. E. Buried alive: how osteoblasts become osteocytes. *Dev. Dyn.* **2006**, *235*(1), 176-190. DOI: 10.1002/dvdy.20603.

Chapter 2 Decomposition of luminescent hydroxyapatite scaffolds in simulated body fluid

Abstract

We present a luminescence study investigating the dissolution of rare-earth doped hydroxyapatite scaffolds in simulated body fluid (SBF), aiming to assess the luminescence stability of Tb-, Ce-, and Eu-doped scaffolds over time. Our findings reveal a consistent decrease in luminescence emission intensity across all samples over a four-week period in which the scaffolds were immersed in the SBF. In addition, energy dispersive spectroscopy confirms a decrease in rare-earth ion concentration in the scaffolds with respect to time, whereas fluorescence spectroscopy shows the presence of rare-earth ions in the SBF, indicating the partial dissolution of the scaffolds over time. The use of rare-earth ions as luminescence markers provides insights into the mechanisms of apatite formation in hydroxyapatites. Thus, our study offers valuable insights for the development of safer and more durable materials for biomedical applications.

2.1 Introduction

Hydroxyapatite HAp, $Ca_5(PO_4)_3(OH)$ or $Ca(I)_4Ca(II)_6(PO_4)_6(OH)_2$ based on the composition of the unit cell[1] is one of the most frequently used biomaterials in orthopedic surgery due to its capability to promote bone formation.[2] It is considered a versatile biomaterial because of its ability to accept dopant element substitutions into its cation (Ca^{2+}) and anion (PO_4^{3-} or OH^-) sites.[3,4] Cationic substitutions can be achieved on Ca(I) and Ca(II) sites by divalent and trivalent ions such as Al^{3+},[5] La^{3+},[6] Fe^{3+},[7] Ce^{3+},[8] or Eu^{2+}/Eu^{3+},[9,10] which requires a charge balance that can be accommodated by the loss of a proton from the OH^- or by the generation of calcium vacancies.[9,11] Rare-earth ions have a particular affinity as substitutional elements in HAp because of their similarity in ionic radii to the calcium ions (*e.g.*, Ca^{2+} = 106 pm, Eu^{3+} = 101 pm, Ce^{3+} = 107 pm and Tb^{3+} = 0.98 pm).[12] Such substitutions result in changes in the lattice parameter and crystallinity of these materials, which may significantly affect their biological, chemical, and physical properties. Consequently, rare-earth doped HAp has potential applications for drug delivery,[13,14] electrical stimulation in tissue engineering technologies,[15] antimicrobials,[16] and cell labeling.[17]

When doped with rare-earth ions such as Eu^{3+}, Ce^{3+}, Tb^{3+}, and Yb^{3+}, HAp exhibits characteristic emission peaks that correspond to the 4*f* to 5*d* transitions of the dopants,[9,18] with an emission intensity dependent on the ion concentration of the dopant.[19] Thus, rare-earth doped HAp can be used as a sensor in tissues and cells.[20] Most of the rare-earth ions employed in the doping of HAp possess a valence state of +3.[21] However, in previous work we have reported the presence of Eu^{2+} and Yb^{2+} in calcium-deficient HAp.[9,10,18] The presence of both valence states (+2 and +3) may have an impact on the well-known bone resorption process during bone remodeling.[22] Bone remodeling is executed by osteoclasts that resorb bone and osteoblasts that fill the resorption

cavities with a bone matrix that subsequently becomes mineralized through a process of bone mineralization. The stimulation of osteoblasts in the process of bone mineralization is related to the ability of hydroxyapatite to release phosphorus and calcium ions from their structure.[23] This can be modulated by changing crystallinity, crystalline phase, and the calcium to phosphorus ratio.[24] Bertazzo *et al*.[25] proposed a mechanism for *in vivo* bone mineralization in hydroxyapatite implants [Figure 10], which initiates with the solubilization of the hydroxyapatite surface and the precipitation of the ions present in the biological fluids, forming an apatite layer, which may have a general composition of $Ca_5(PO_4)_3(OH)$ (hydroxyapatite), $Ca_5(PO_4)_3F$ (fluorapatite), or $Ca_5(PO_4)_3Cl$ (chlorapatite).[1] This process is followed by the absorption of proteins and organic material, along with the adhesion of cells, their proliferation, and ultimately the formation of new bone. The performance of an implant (bioactivity) depends on its ability to form an apatite layer on the surface.[25] Furthermore, the formation of the apatite layer is linked to the solubility of the hydroxyapatite implant, although the formation of an apatite layer is not exclusively limited to the presence of dissolved calcium or phosphorus ions from the implant, since both ions would be available if the implant was immersed in a biological fluid. In fact, previous reports have demonstrated apatite formation on surfaces of SiO_2 gel, gel-derived TiO_2, ZrO_2 gel, Nb_2O_5 gel, and Ta_2O_5 gel, among others, immersed in simulated body fluid (SBF).[26–31] SBF usually contains Na^+, K^+, Ca^{2+}, Mg^{2+}, Cl^-, $(HCO_3)^-$, $(HPO_4)^{2-}$, and $(SO_4)^{2-}$, which may result in the deposition of oxides, such as CaO and P_2O_5, that nucleate and grow the apatite layer,[32] even if the implant is not hydroxyapatite.

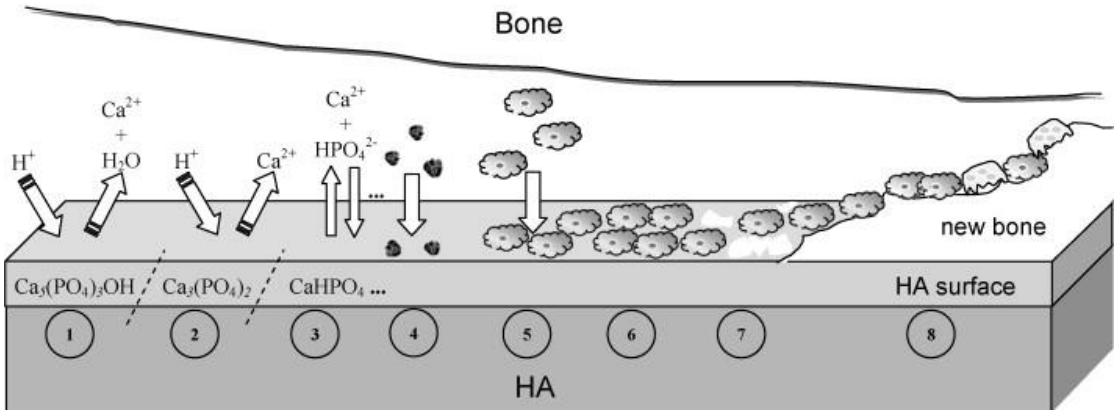

Figure 10. Schematic diagram representing the phenomena that occur on the surface of hydroxyapatite after implantation.
(1) Beginning of the implant procedure, where the solubilization of the hydroxyapatite surface starts. (2) Continuation of the solubilization of the hydroxyapatite surface. (3) Achievement of equilibrium between physiological solutions and the modified surface of hydroxyapatite.[25]

Given that the solubility of HAp plays a crucial role in the bone mineralization process, the ability to monitor it is essential. Xie *et al.*[20] demonstrated the feasibility of monitoring the dissolution of europium-doped hydroxyapatite in acetic acid by measuring the amount of europium dissolved in the acid, providing a valuable approach to studying and understanding HAp solubilization in a solution. Nonetheless, a study of rare-earth doped hydroxyapatite solubility in the presence of SBF has not been reported before. In this work, we present a luminescence study on the solubilization of Eu^{2+}/Eu^{3+}-, Ce^{3+}-, and Tb^{3+}-doped HAp scaffolds in the presence of SBF. We determine that the photoluminescence emission from the scaffolds decreases in a linear manner with respect to soaking time in the simulated body fluid. From scanning electron microscopy and energy dispersive spectroscopy we also show the formation of an apatite layer on the surfaces of the scaffolds. Thus, demonstrating the possibility of monitoring the gradual dissolution and re-precipitation of hydroxyapatite in SBF, and contributing to an understanding of the dissolution stability of hydroxyapatite in physiological fluids and the use of rare-earth ions as luminescence markers for biomaterials.

2.2 Experimental Methods

Eu^{2+}/Eu^{3+}-, Ce^{3+}-, and Tb^{3+}-doped hydroxyapatite powders (HAp:Eu, HAp:Ce, and HAp:Tb) were synthesized by solution combustion synthesis.[33–41] The reagents used were calcium nitrate tetrahydrate [$Ca(NO_3)_2 \cdot 4H_2O$, 99%, Alfa Aesar, Ward Hill, MA], ammonium hydrogen phosphate [$(NH_4)_2HPO_4$, 98%, Alfa Aesar, Ward Hill, MA], and carbohydrazide [$CO(NHNH_2)_2$, 97%, Alfa Aesar, Ward Hill, MA]. Europium nitrate hexahydrate [$Eu(NO_3)_3 \cdot 6H_2O$, 99.9%, Alfa Aesar, Ward Hill, MA], cerium nitrate hexahydrate [$Ce(NO_3)_3 \cdot 6H_2O$, 99.9%, Sigma Aldrich], and terbium nitrate hexahydrate [$Tb(NO_3)_3 \cdot 6H_2O$, 99.9%, Sigma Aldrich], were used as sources of the rare-earth dopants. The HAp:RE powders were prepared by dissolving 26.872 mmol of $Ca(NO_3)_2 \cdot 4H_2O$ and 1.414 mmol of rare-earth dopant into 28.28 mL of deionized water. Separately, 17.538 mmol of $(NH_4)_2HPO_4$ were dissolved in 25.45 mL of deionized water. The $(NH_4)_2HPO_4$ solution was then added dropwise to the calcium and rare-earth ion solution under continuous stirring, maintaining a molar ratio of Ca+RE to P of 1.67. Subsequently, 4.035 g of carbohydrazide were dissolved into the mixed solution and placed in a Pyrex crystallization dish, to be introduced into a furnace preheated at 773 K until ignition occurred, within approximately 15 minutes. The resulting HAp:RE powders were calcined at 873 K for 4 hours.

The calcined powders were characterized by X-ray diffraction on a Bruker D2 Phaser using CuKα radiation and a step size of 0.01° over the 2θ range of 20 to 70 degrees. Particle size distributions were determined on a Microtrac Nanotrac ULTRA dynamic light scattering system, dispersing approximately 5 mg of powder in 20 mL of deionized water, stirring for 15 minutes and ultrasonicating for 15 minutes.

The slurry used to form the scaffolds were prepared by mixing 4 g of the HAp:RE powder with 1 mL of deionized water. The scaffolds were extruded using a syringe with an 18G needle

and dried in an oven at 343 K for 1 hour. The SBF was prepared by dissolving sodium chloride [NaCl, 99.5%, Sigma Aldrich], sodium bicarbonate [$NaHCO_3$, 99.7%, Sigma Aldrich], potassium chloride [KCl, 99.0%, Sigma Aldrich], dipotassium hydrogen phosphate [$K_2HPO_4 \cdot 3H_2O$, 98%, Sigma Aldrich], magnesium chloride [$MgCl_2 \cdot 6H_2O$, 98%, Sigma Aldrich], calcium chloride [$CaCl_2$, 99.0%, Sigma Aldrich], sodium sulfate [Na_2SO_4, 99.0%, Sigma Aldrich], hydrochloric acid [HCl, 1N, Fisher Scientific], and tris-(hydroxymethyl) aminomethane [$(CH_2OH)_3CNH_2$, 99.8%, Sigma Aldrich], in deionized water and buffered to pH 7.40 at 309 K with HCl. The solution was prepared based on the method outlined by Kokubo *et al.*[42] The evaluation of the solubility was carried out by soaking the scaffolds in SBF for 4 weeks in a concentration of 1 mg of scaffold to 1 mL of SBF. After each week a volume of scaffold of approximate dimensions $5 \times 5 \times 5$ mm^3 was taken from each sample and analyzed using photoluminescence.

Energy dispersive spectroscopy (EDS) was utilized to determine elemental composition using an X-Max Oxford-Instruments system with a detector size of 20 mm^2. The morphologies of the powders and scaffolds were evaluated by scanning electron microscopy (SEM) using a JEOL JIB-4500 instrument at 10 kV. Photoluminescence measurements were performed in a Hitachi F-4500 fluorescence spectrophotometer over a wavelength range of 200 to 800 nm. To enhance the luminescence emission from the europium ions present in the SBF solution, 50 mL of SBF were mixed with 5 mL of PerkinElmer Delfia® enhancement solution and analyzed in a Cary Eclipse fluorescence spectrophotometer using an excitation wavelength of 395 nm.

2.3 Results and Discussion

Figure 11 shows the emission of HAp:RE powder under UV light, exhibiting the characteristic colors for europium (red), cerium (blue) and terbium (green).

Figure 11. Emission of the HAp:RE powder under UV light.

The doped HAp powders display a flake-like morphology [Figure 12a] with an average particle size of ~120 nm from dynamic light scattering [Figure 12b]. Powder X-ray diffraction [Figure 13] verified the phase purity and crystal structure of the doped samples corresponding to PDF #09-0432. These patterns agree with the hexagonal HAp phase (space group $P6_3/m$). In addition, the patterns exhibit a small peak at ~31°, which corresponds to beta tri-calcium phosphate (β-TCP, PDF #06-0426), present as a minor secondary phase. The β-TCP phase is formed during the combustion synthesis process, since it reaches higher temperatures (973 K) that are amenable to the formation of this phase. The patterns do not show the formation of rare-earth oxides due to the small concentration of the dopants (~1 at.%, Table 1).

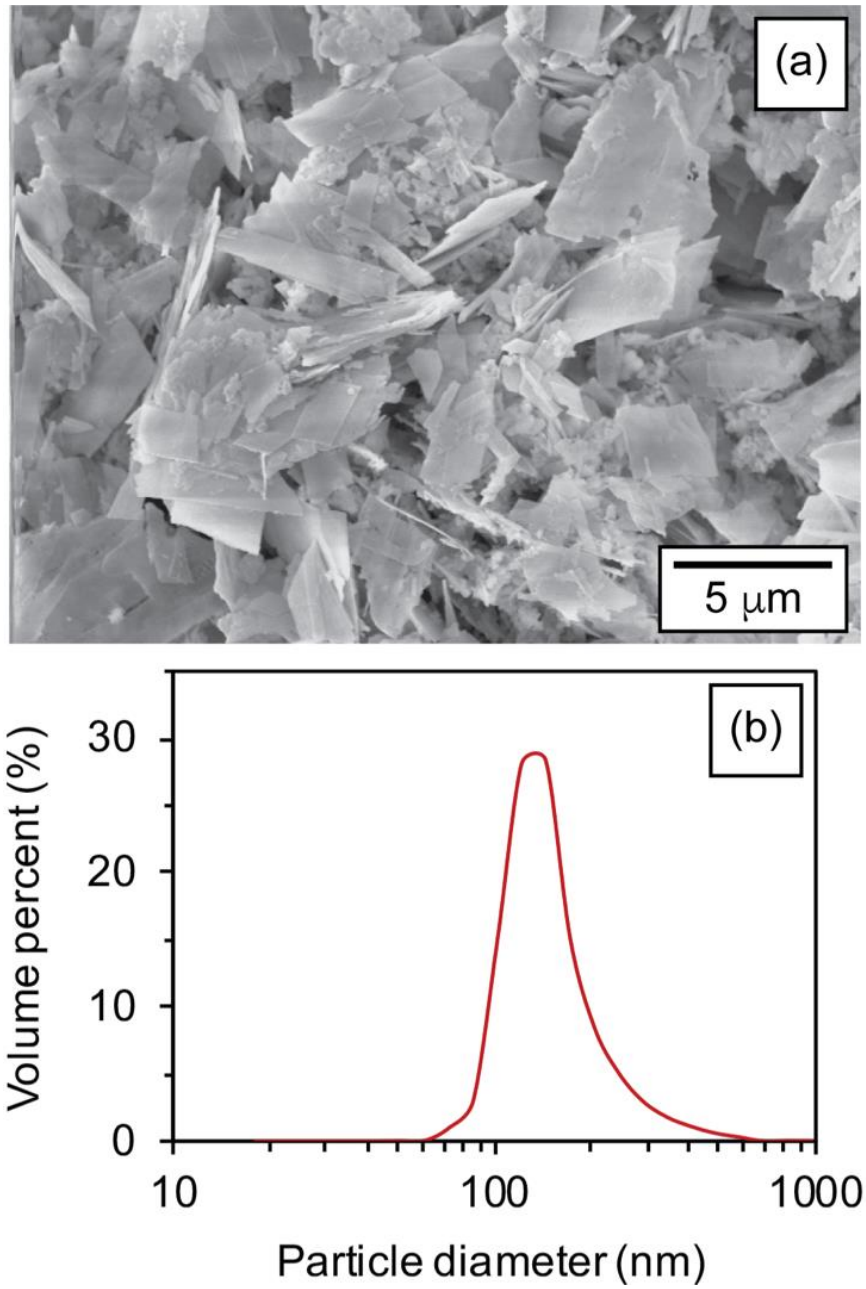

Figure 12. (a) Scanning electron micrograph and (b) particle size distribution of the combustion synthesized HAp powders.

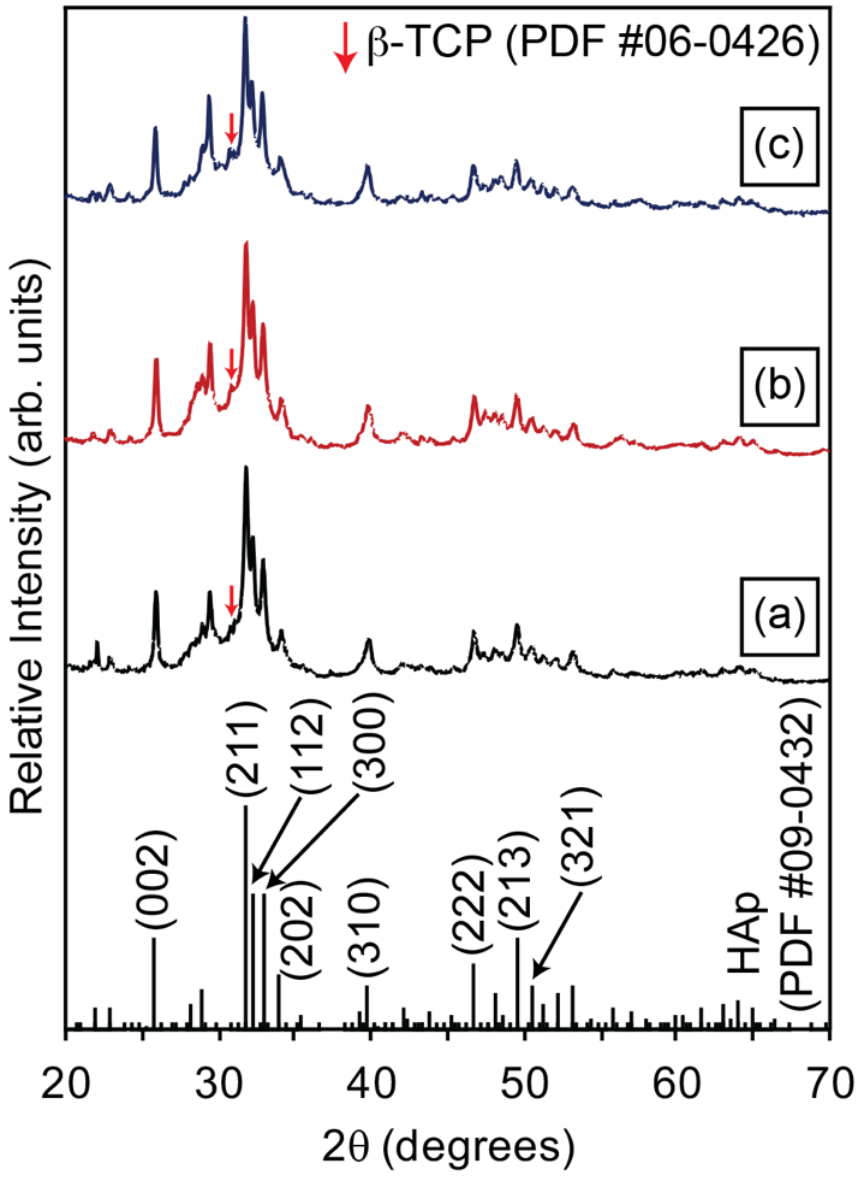

Figure 13. X-ray diffraction patterns of the (a) HAp:Eu, (b) HAp:Ce, and (c) HAp:Tb powders. The red arrow marks the location of the primary peak for TCP.

The emission spectra of the HAp:Eu, HAp:Ce, and HAp:Tb powders [Figure 14], show the characteristic emission bands for Eu^{3+}, Ce^{3+} and Tb^{3+} ions, respectively. HAp:Ce, under excitation at 265 nm, shows a broad band at 360 nm, attributed to the transitions $^2D_{3/2} \rightarrow {}^2F_{5/2}$ and $^2D_{3/2} \rightarrow {}^2F_{7/2}$ (labeled A and B).[43–45] The emission spectrum for HAp:Tb, under excitation at 228 nm, exhibits four peaks centered at 493, 547, 591 and 626 nm (labeled C, D, E and F), and

corresponding to the transitions $^5D_4 \rightarrow {}^7F_6$, $^5D_4 \rightarrow {}^7F_5$, $^5D_4 \rightarrow {}^7F_4$ and $^5D_4 \rightarrow {}^7F_3$, respectively.[46] The emission bands marked G, H, I, and J, for HAp:Eu correspond to the transitions $^5D_0 \rightarrow {}^7F_1$, $^5D_0 \rightarrow {}^7F_2$, $^5D_0 \rightarrow {}^7F_3$ and $^5D_0 \rightarrow {}^7F_4$ with centers at 594, 617, 655 and 698 nm.[47]

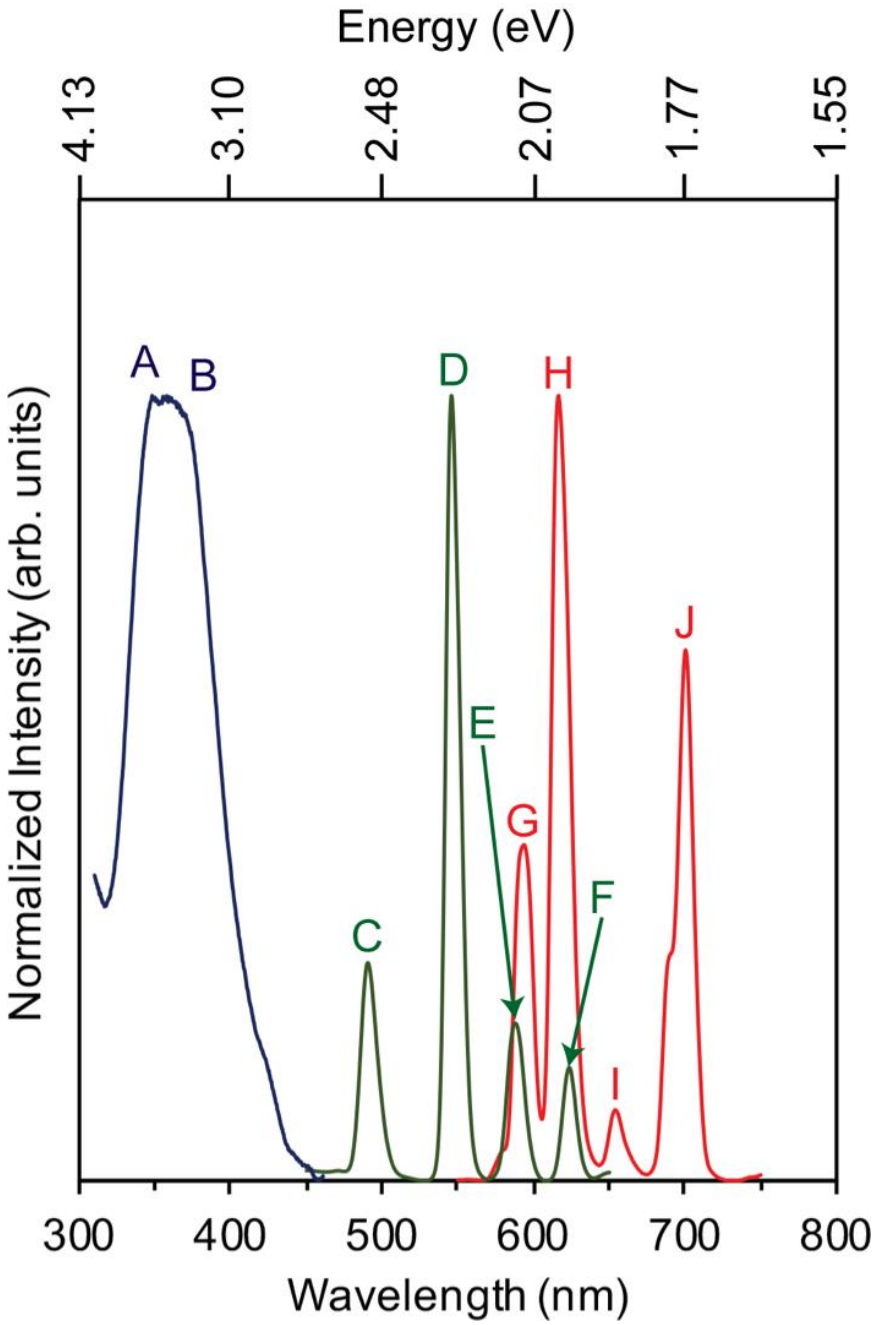

Figure 14. Photoluminescence emission spectra of HAp:Eu (red), HAp:Ce (blue) and HAp:Tb (green). A-B are the characteristic emission peaks for Ce^{3+}, C-F are the characteristic emission peaks for Tb^{3+}, and G-J are the characteristic emission peaks for Eu^{3+}.

Table 3 summarizes the EDS results of the scaffolds before and after immersion in SBF for four weeks. The Ca/P ratios for all samples are below the stoichiometric value of 1.67 for HAp, indicating that the materials correspond to Ca-deficient HAp. In addition, from Table 3, we observe a notable decrease in the concentration of rare-earth ions after immersion in SBF, attributed to the partial dissolution of the HAp:RE scaffolds. Specifically, europium experiences a substantial decline in concentration from 1.26 to 0.49 (~60% decrease), whereas cerium and terbium exhibit a decrease of ~30% and ~40%, respectively. The provenance of the oxygen, phosphorus, and calcium signals originate from both the HAp scaffolds and the ions in SBF, and it is not possible to separate the contributions, but EDS can provide us information on sodium and chlorine, which are present in the scaffolds only after soaking and must be from the SBF, since HAp does not contain either element in its structure.

Table 3. Elemental composition of the HAp:RE scaffolds before and after soaking in simulated body fluid for 4 weeks (determined from energy dispersive spectroscopy).

	O (at.%)	P (at.%)	Ca (at.%)	RE (at.%)	Na and Cl (at.%)	Ca/P
Before soaking in simulated body fluid						
HAp:Eu	55.98	17.73	25.03	1.26	-	1.41
HAp:Ce	57.32	17.38	23.95	1.35	-	1.38
HAp:Tb	57.57	17.85	23.25	1.33	-	1.30
After soaking in simulated body fluid						
HAp:Eu	50.51	14.66	22.91	0.49	11.43	1.56
HAp:Ce	46.55	15.51	22.59	0.95	14.39	1.46
HAp:Tb	47.86	15.37	22.94	0.81	13.04	1.49

The concentrations correspond to 11.43%, 14.39%, and 13.04%, for the HAp:Eu, HAp:Ce, and HAp:Tb scaffolds, respectively. Also, the Ca/P ratio increases in all scaffolds, from 1.41 to

1.56 in HAp:Eu, 1.38 to 1.46 in HAp:Ce, and 1.30 to 1.46 in HAp:Tb. The change in the Ca/P ratio is a result of the formation of apatite on the surface of the scaffold, a process previously reported in apatite materials in the presence of SBF.[48–50] Figure 15 illustrates the surface of the HAp:Eu scaffold before [Figure 15a] and after [Figure 15b] soaking in SBF, providing visual support for the formation of an apatite layer on the surface of the scaffolds. These images reveal the deposition of faceted particles after soaking, as these particles are present only in Figure 15b. According to the EDS analysis performed on one of these particles [Figure 15c], calcium, phosphorus and oxygen from the hydroxyapatite and/or the SBF are present. However, sodium and chlorine are also found and must be originating from the SBF.

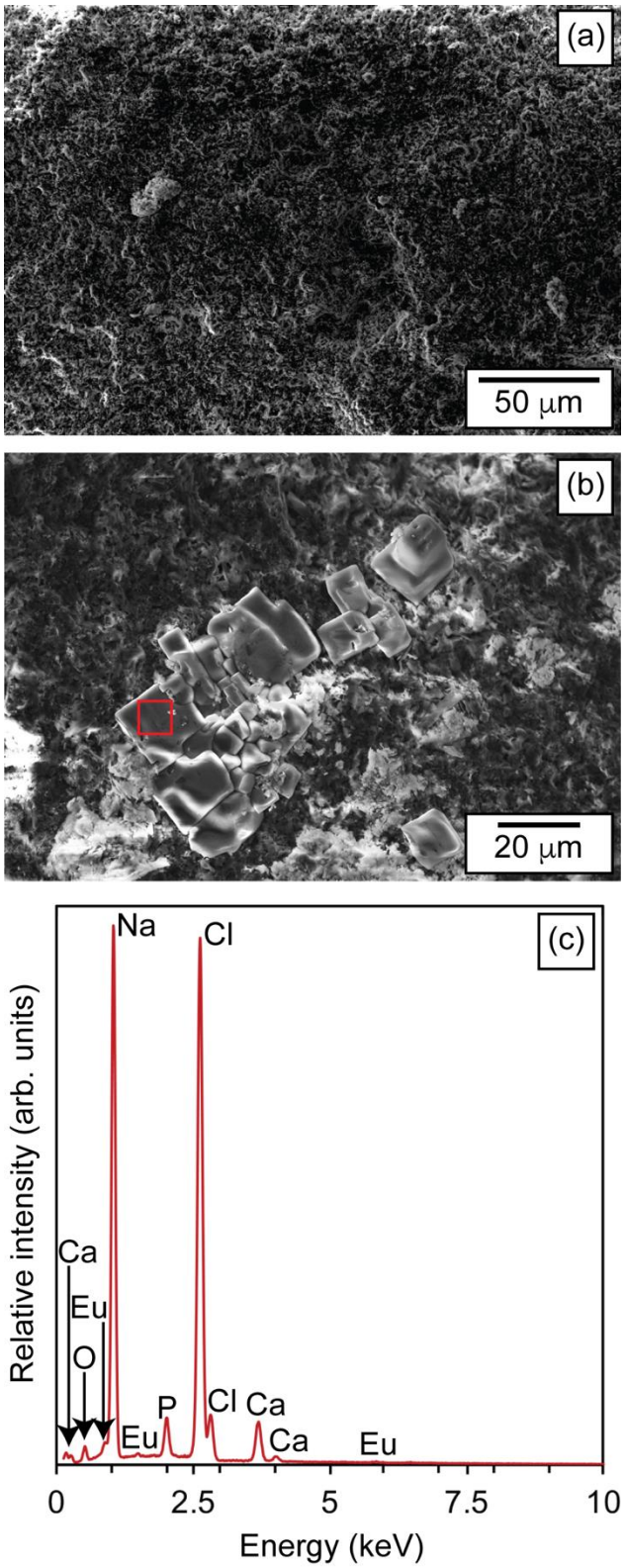

Figure 15. Scanning electron micrograph of the HAp:Eu scaffold (a) before and (b) after soaking in SBF for 4 weeks. (c) Energy dispersive spectrum of the HAp:Eu scaffold (obtained from the red square in (b)).

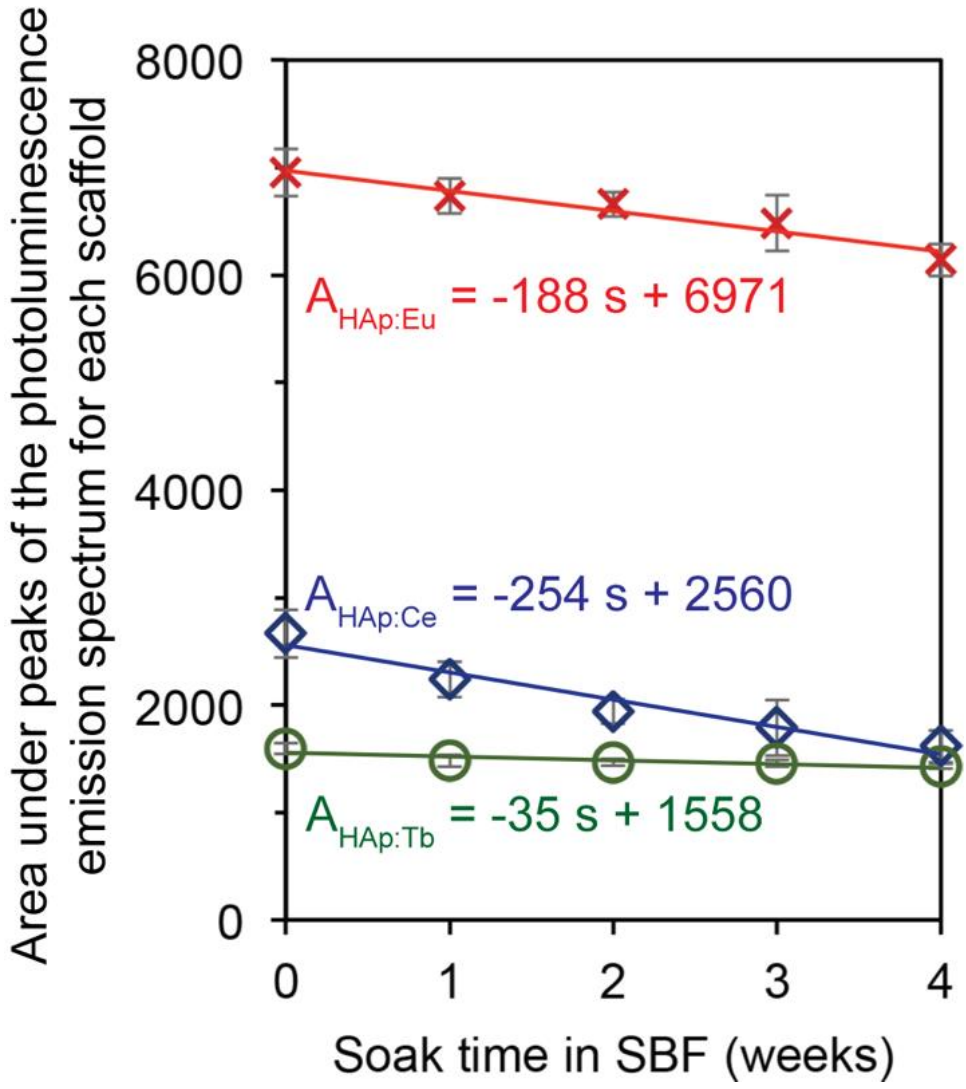

Figure 16. Area under peaks of the photoluminescence emission spectrum for the HAp:Eu, HAp:Ce, and HAp:Tb scaffolds.

Figure 16 depicts the values of the areas under the curves of the photoluminescence emission spectra corresponding to the three scaffolds. All the scaffolds exhibit a linear attenuation of the emission. We tested the release of europium from the HAp:Eu scaffold into the SBF [Figure 17], and show that all peaks in the fluorescence spectrum of the SBF correspond to the characteristic emission of Eu^{3+}. The peaks centered at 488 nm, 539 nm, and 618 nm, correspond to the transitions $^5D_2 \rightarrow {}^7F_0$, $^5D_1 \rightarrow {}^7F_0$, and $^5D_0 \rightarrow {}^7F_2$, respectively. Thus, the weakening of the

photoluminescence emission is due to the partial dissolution of the scaffolds into the SBF. Note that Figure 6 shows no signal for the SBF (dashed line) before immersion of the scaffold.

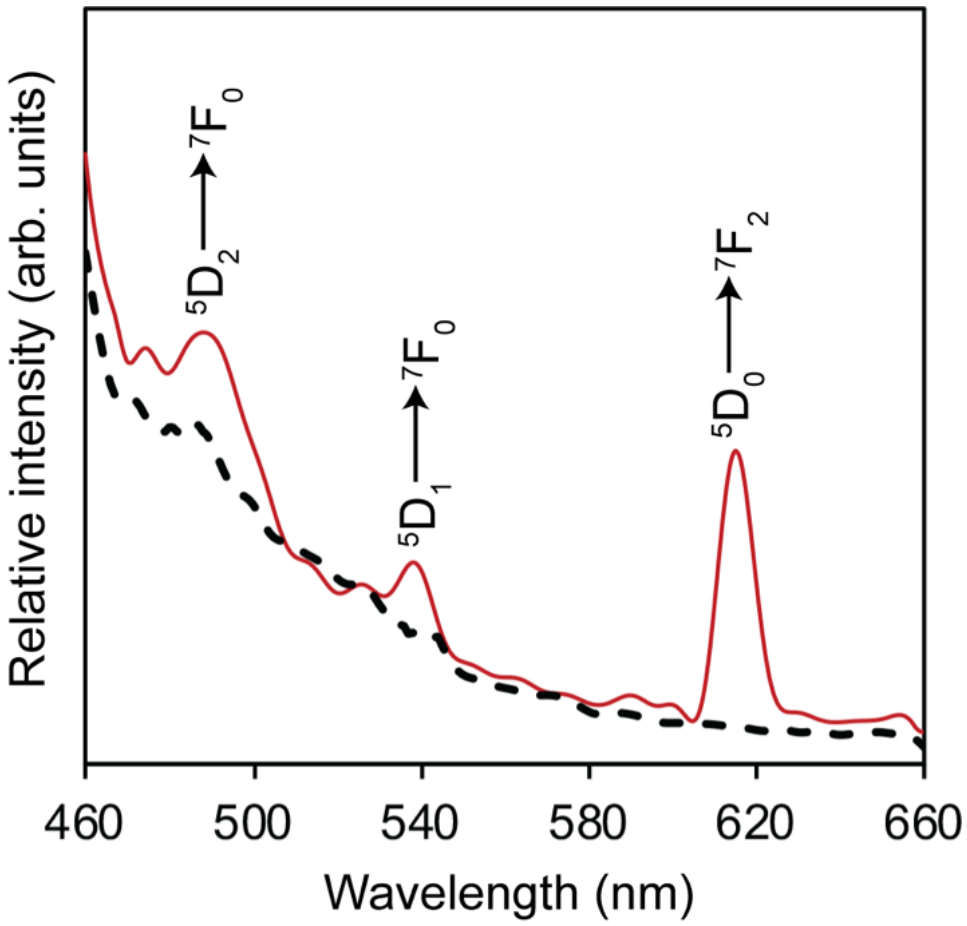

Figure 17. Fluorescence spectra of SBF before (dashed line) and after contact with the HAp:Eu scaffold for four weeks (solid line).

The mineralization mechanism of HAp has been discussed previously by Kim *et al.*[51] and Bertazzo *et al.*[25] According to Kim *et al.*[51] the negative charge on the surface of HAp enables the attraction of positively charged calcium ions from the SBF. This attraction results in the formation of a calcium-rich amorphous apatite. Subsequently, these positive charges selectively bind with negatively charged phosphate ions present in the SBF, leading to the formation of a calcium-poor apatite structure. In contrast, Bertazzo *et al.*[25] suggested that the first step involves the solubilization of HAp, followed by the precipitation of phosphate ions, leading to the formation of

a “biological apatite” (apatite deficient in calcium). However, this model was originally proposed based on reactions reported by Dorozhkin[52,53] for the HAp dissolution in different solutions that did not specifically examine the behavior in SBF.

By incorporating rare-earth ions as probes within HAp and based on the emissions observed in our photoluminescence spectra, we shed light on the interactions occurring on the surface of hydroxyapatite. In Figure 18, we describe the apatite formation mechanism. The europium fluorescence found in SBF [Figure 16] and the photoluminescence attenuation described in Figure 5 are evidence of the partial dissolution of the HAp scaffold, and we describe the process as follows. As a first step [Figure 18a], Ca^{2+}, PO_4^{3-}, and the rare-earth ions are dissolved in the SBF. The process of re-precipitation follows [Figure 18b], confirmed from images represented by Figure 5b, where platelets that are not present on the surface of the scaffold before immersion are now evident, and from the EDS analysis of Figure 5c, in which calcium and phosphorus from the SBF are evident, indicating the formation of apatite.[31,50,54] While our results do not show a homogeneous layer formed on the surface of the scaffolds, previous studies[25,51] suggest that the process of precipitation continues until equilibrium is achieved, resulting in a continuous apatite layer [Figure 18c].

Understanding the initial steps in the formation of apatite on doped HAp and determining its luminescence stability are crucial pieces of information for developing highly effective bioactive materials for medical applications. By knowing how apatite forms initially, we can tailor biomaterials to encourage this process, ultimately enhancing their ability to integrate with biological tissues. Additionally, the stable luminescence of HAp ensures that these materials maintain their performance over time, a vital characteristic for their sustained effectiveness in medical applications.

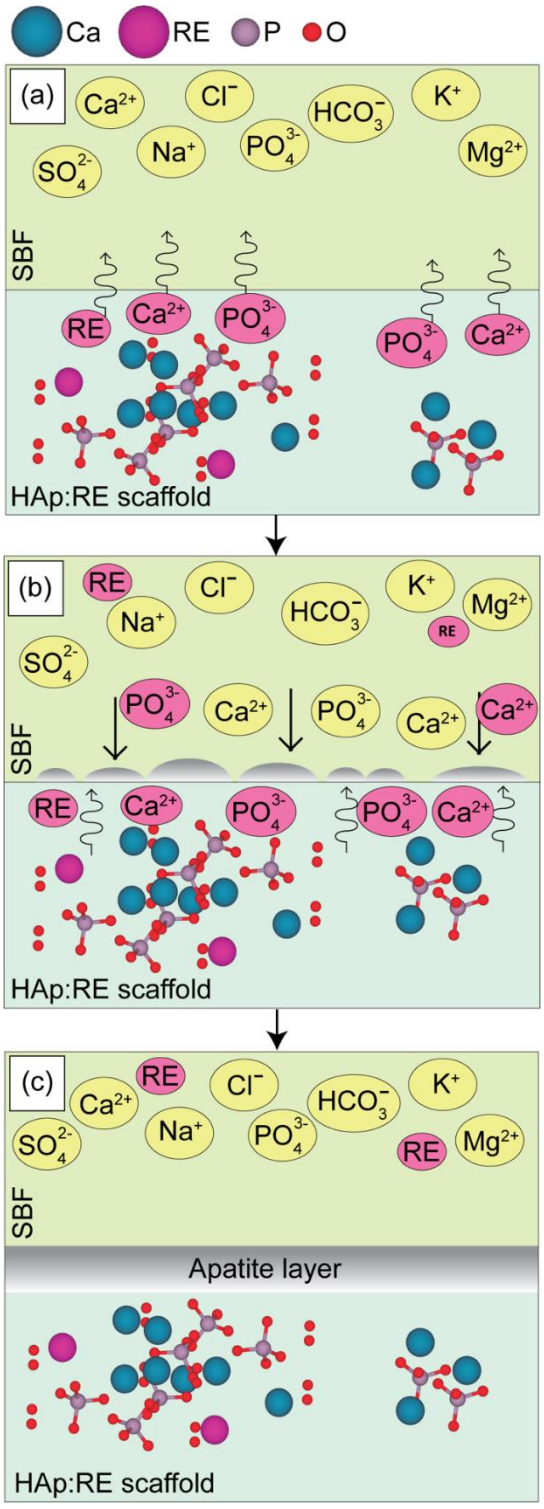

Figure 18. Schematic depicting surface changes in the HAp:RE scaffold during SBF immersion: (a) Initial HAp:RE surface solubilization, (b) ongoing HAp:RE surface solubilization concurrent with ion precipitation from SBF, primarily calcium and phosphorus, and (c) formation of an apatite layer upon reaching equilibrium between SBF and the HAp:RE surface.

2.4 Conclusions

Rare-earth doped hydroxyapatite (HAp) was synthesized by solution combustion synthesis, with europium, cerium, and terbium as dopants. The powders reveal a flake-like morphology and a particle size distribution of around 120 nm. According to X-ray diffraction analysis, the dopant concentration does not modify the crystal structure of the hydroxyapatite. Due to the high temperatures reached during combustion, a phase of β-TCP was formed as a minor secondary phase. The presence of the rare-earth ions in the powders was confirmed by EDS measurements, revealing a concentration of 1.26%, 1.35%, and 1.33% for HAp:Eu, HAp:Ce, and HAp:Tb, respectively. Photoluminescence spectra show the corresponding emissions of Eu^{3+} (594, 617, 655 and 698 nm), Ce^{3+} (360 nm), and Tb^{3+} (493, 547, 591 and 626 nm). After synthesis, the powders were used to prepare scaffolds using a solid free-form fabrication technique, then were soaked in simulated body fluid for four weeks, where it was found that the scaffolds were partially dissolved by SBF suggesting that this dissolution could serve as the initial stage for the formation of apatite on the scaffold surface. All the scaffolds showed a linear attenuation of the emission after exposure to SBF. Fluorescence analysis of the SBF revealed the presence of dissolved europium in the fluid. The mineralization on the surface of the scaffolds can be explained by a simple solubilization, precipitation, and subsequent formation of an apatite layer.

Chapter 2, in part, has been submitted for publication of the material as it may appear in ACS Applied Bio Materials, 2024. Martinez-Pallares, Fabian; Herrera-Zaldivar, Manuel; Graeve, Olivia A. The dissertation author was the primary author of this paper.

References

[1]. White, T.; Ferraris, C.; Kim, J.; Madhavi, S. Apatite - an adaptive framework structure. *Rev. Mineral. Geochem*. **2005**, *57* (1), 307–401. DOI: 10.2138/rmg.2005.57.10

[2]. Šupová, M. Substituted hydroxyapatites for biomedical applications: A review. *Ceram. Int.* **2015**, *41* (8), 9203–923. DOI: 10.1016/j.ceramint.2015.03.316

[3]. Ressler, A.; Žužić, A.; Ivanišević, I.; Kamboj, N.; Ivanković, H. Ionic substituted hydroxyapatite for bone regeneration applications: A review. *Open Ceram.* **2021**, *6*, 100122. DOI: 10.1016/j.oceram.2021.100122

[4]. Tite, T.; Popa, A.- C.; Balescu, L. M.; Bogdan, I. M.; Pasuk, I.; Ferreira, J. M. F.; Stan, G. E. Cationic substitutions in hydroxyapatite: Current status of the derived biofunctional effects and their in vitro interrogation methods. *Materials (Basel)* **2018**, *11* (11), 2081. DOI: 10.3390/ma11112081

[5]. Kolekar, T. V.; Thorat, N. D.; Yadav, H. M.; Magalad, V. T.; Shinde, M. A.; Bandgar, S. S.; Kim, J. H.; Agawane, G. L. Nanocrystalline hydroxyapatite doped with aluminium: A potential carrier for biomedical applications. *Ceram. Int.* **2016**, *2* (4), 5304–5311. DOI: 10.1016/j.ceramint.2015.12.060

[6]. Webster, T. J.; Massa-Schlueter, E. A.; Smith, J. L.; Slamovich, E. B. Osteoblast response to hydroxyapatite doped with divalent and trivalent cations. *Biomaterials.* **2004**, *25* (11), 2111–2121. DOI: 10.1016/j.biomaterials.2003.09.001

[7]. Jose, S.; Senthilkumar, M.; Elayaraja, K.; Haris, M.; George, A.; Dhayal Raj, A.; Sundaram, S. J.; Bashir, A. K. H.; Maaza, M.; Kaviyarasu, K. Preparation and characterization of Fe doped *n*-hydroxyapatite for biomedical application. *Surf. Interfaces.* **2021**, *25*, 101185. DOI: 10.1016/j.surfin.2021.101185

[8]. Feng, Z.; Liao, Y.; Ye, M. Synthesis and structure of cerium-substituted hydroxyapatite. *J. Mater. Sci. - Mater. Med.* **2005**, *16*, 417–421. DOI: 10.1007/s10856-005-6981-8

[9]. Zavala-Sanchez, L. A.; Hirata, G. A.; Novitskaya, E.; Karandikar, K.; Herrera, M.; Graeve, O. A. Distribution of Eu2+ and Eu3+ ions in hydroxyapatite: A cathodoluminescence and Raman study, *ACS Biomater. Sci. Eng.* **2015**, *1* (12), 1306–1313. DOI: 10.1021/acsbiomaterials.5b00378

[10]. Graeve, O. A.; Kanakala, R.; Madadi, A.; Williams, B. C.; Glass, K. C. Luminescence variations in hydroxyapatites doped with Eu2+ and Eu3+ ions. *Biomaterials*. **2010**, *31* (15), 4259–4267. DOI: 10.1016/j.biomaterials.2010.02.009

[11]. Serret, A.; Cabañas, M. V.; Vallet-Regi, M. Stabilization of calcium oxyapatites with lanthanum(III)-created anionic vacancies. *Chem. Mater*. **2000**, *12* (12), 3836–3841. DOI: 10.1021/cm001117p

[12]. Shannon, R. D. Revised effective ionic radii and systematic studies of interatomic distances in halides and chalcogenides. *Acta Crystallogr., Sect. A: Found. Crystallogr.* **1976**, *32* (5), 751–762. DOI: 10.1107/S0567739476001551

[13]. Yang, P.; Quan, Z.; Li, C.; Kang, X.; Lian, H.; Lin, J. Bioactive, luminescent and mesoporous europium-doped hydroxyapatite as a drug carrier. *Biomaterials*. **2008**, *29* (32), 4341–4347. DOI: 10.1016/j.biomaterials.2008.07.042

[14]. Ahymah Joshy, M. I.; Elayaraja, K.; Suganthi, R. V.; Chandra Veerla, S.; Kalkura, S. N. *In vitro* sustained release of amoxicillin from lanthanum hydroxyapatite nano rods. *Curr. Appl. Phys.* **2011**, *11* (4), 1100–1106. DOI: 10.1016/j.cap.2011.02.003

[15]. Li, Y.; Ooi, C. P.; Cheang, P. H. N.; Khor, K. A. Synthesis and characterization of neodymium(III) and gadolinium(III)-substituted hydroxyapatite as biomaterials. *Int. J. Appl. Ceram. Technol*. **2009**, *6* (4), 501–512. DOI: 10.1111/j.1744-7402.2008.02293.x

[16]. Lin, Y.; Yang, Z.; Cheng, J. Preparation, characterization and antibacterial property of cerium substituted hydroxyapatite nanoparticles. *J. Rare Earths* **2007**, *25* (4), 452–456. DOI: 10.1016/S1002-0721(07)60455-4

[17]. Zantye, P.; Fernandes, F.; Ramanan, S. R.; Kowshik, M. Rare earth doped hydroxyapatite nanoparticles for in vitro bioimaging applications. *Curr. Phys. Chem.* **2019**, *9* (2), 94–109. DOI: 10.2174/1877946809666190828104812

[18]. Zavala, L. A.; Fernández, P.; Novitskaya, E.; Díaz, J. N.; Herrera, M.; Graeve, O. A. Interconfigurational and intraconfigurational transitions of Yb2+ and Yb3+ ions in hydroxyapatite: A cathodoluminescence study. *Acta Mater*. **2017**, *135*, 35–43. DOI: 10.1016/j.actamat.2017.06.003

[19]. Popa, C. L.; Ciobanu, C. S. Synthesis and characterization of fluorescent hydroxyapatite. *Rom. Rep. Phys.* **2016**, *68* (3), 1170–1177.

[20]. Xie, Y.; Perera, T. S. H.; Li, F.; Han, Y.; Yin, M. Quantitative detection method of hydroxyapatite nanoparticles based on Eu3+ fluorescent labeling in vitro and in vivo. *ACS Appl. Mater. Interfaces* **2015**, *7* (43), 23819–23823. DOI: 10.1021/acsami.5b08767

[21]. Gu, M.; Li, W.; Jiang, L.; Li, X. Recent progress of rare earth doped hydroxyapatite nanoparticles: Luminescence properties, synthesis and biomedical applications. *Acta Biomater*. **2022**, *148*, 22–43. DOI: 10.1016/j.actbio.2022.06.006

[22]. Wu, L.; Yang, F.; Xue, Y.; Gu, R.; Liu, H.; Xia, D.; Liu, Y. The biological functions of europium-containing biomaterials: A systematic review. *Mater. Today Bio* **2023**, *19*, 100595. DOI: 10.1016/j.mtbio.2023.100595

[23]. Jeong, J.; Kim, J. H.; Shim, J. H.; Hwang, N. S.; Heo, C. Y. Bioactive calcium phosphate materials and applications in bone regeneration. *Biomater. Res.* **2019**, *23*, 4. DOI: 10.1186/s40824-018-0149-3

[24]. Dorozhkin S. V. Calcium orthophosphate-based bioceramics. *Materials (Basel)* **2013**, *6* (9), 3840–3942. DOI: 10.3390/ma6093840

[25]. Bertazzo, S.; Zambuzzi, W. F.; Campos, D. D. P.; Ogeda, T. L.; Ferreira, C. V.; Bertran, C. A. Hydroxyapatite surface solubility and effect on cell adhesion. *Colloids Surf., B* **2010**, *78* (2), 177–184. DOI: 10.1016/j.colsurfb.2010.02.027

[26]. Li, P.; Ohtsuki, C.; Kokubo, T.; Nakanishi, K.; Soga, N.; Nakamura, T.; Yamamuro, T. Apatite formation induced by silica gel in a simulated body fluid. *J. Am. Ceram. Soc.* **1992**, *75* (8), 2094–2097. DOI: 10.1111/j.1151-2916.1992.tb04470.x

[27]. Li, P.; Ohtsuki, C.; Kokubo, T.; Nakanishi, K.; Soga, N.; De Groot, K. The role of hydrated silica, titania, and alumina in inducing apatite on implants. *J. Biomed. Mater. Res.* **1994**, *28* (1), 7–15. DOI: 10.1002/jbm.820280103

[28]. Uchida, M.; Kim, H. -M.; Kokubo, T.; Miyaji, F.; Nakamura, T. Bonelike apatite formation induced on zirconia gel in a simulated body fluid and its modified solutions. *J. Am. Ceram. Soc.* **2001**, *84* (9), 2041–2044. DOI: 10.1111/j.1151-2916.2001.tb00955.x

[29]. Miyazaki, T.; Kim, H. -M.; Kokubo, T.; Ohtsuki, C.; Nakamura, T. Apatite-forming ability of niobium oxide gels in a simulated body fluid. *J. Ceram. Soc. Jpn.* **2001**, *109* (1275), 929–933. DOI: 10.1002/jbm.820280103

[30]. Miyazaki, T.; Kim, H. -M.; Kokubo, T.; Kato, H.; Nakamura, T. Induction and acceleration of bonelike apatite formation on tantalum oxide gel in simulated body fluid. *J. Sol-Gel Sci. Technol.* **2001**, *21*, 83–88. DOI: 10.1023/A:1011265701447

[31]. Yamaguchi, S.; Nath, S.; Sugawara, Y.; Divakarla, K.; Das, T.; Manos, J.; Chrzanowski, W.; Matsushita, T.; Kokubo, T. Two-in-one biointerfaces–Antimicrobial and bioactive nanoporous gallium titanate layers for titanium implants. *Nanomaterials (Basel)*, **2017**, *7* (8), 229. DOI: 10.3390/nano7080229

[32]. Pan, H.; Zhao, X.; Darvell, B. W.; Lu, W. W. Apatite-formation ability – predictor of "bioactivity"?. Acta Biomater. **2010**, *6* (11), 4181–4188 (2010). DOI: 10.1016/j.actbio.2010.05.013

[33]. Novitskaya, E.; Manheim, A.; Herrera, M.; Graeve, O. A. Effect of oxygen vacancies on the mechanoluminescence response of magnesium oxide. *J. Phys. Chem. C* **2021**, *125* (1) 854–864. DOI: 10.1021/acs.jpcc.0c07674

[34]. Novitskaya, E., Kelly, J. P., Bhaduri, S., Graeve, O. A. A review of solution combustion synthesis: An analysis of parameters controlling powder characteristics. *Int. Mater. Rev.* **2021**, *66* (3), 188–214. DOI: 10.1080/09506608.2020.1765603

[35]. Kanakala, R.; Escudero, R.; Rojas-George, G.; Ramisetty, M.; Graeve, O. A. Mechanisms of combustion synthesis and magnetic response of high-surface-area hexaboride compounds. *ACS Appl. Mater. Interfaces* **2011**, *3* (4), 1093–1100. DOI: 10.1021/am1012276

[36]. Kanakala, R.; Rojas-George, G.; Graeve, O. A. Unique preparation of hexaboride nanocubes: A first example of boride formation by combustion synthesis. *J. Am. Ceram. Soc.* ***2010****, 93 (10),* 3136–3141. DOI: 10.1111/j.1551-2916.2010.03853.x

[37]. Sinha, K.; Pearson, B.; Casolco, S. R.; Garay, J. E.; Graeve, O. A. Synthesis and consolidation of BaAl2Si2O8:Eu. Development of an integrated process for luminescent smart ceramic materials. *J. Am. Ceram. Soc.* **2009**, *92* (11), 2504–2511. DOI: 10.1111/j.1551-2916.2009.03242.x

[38]. Graeve, O. A.; Varma, S.; Rojas-George, G.; Brown, D. R.; Lopez, E. A. Synthesis and characterization of luminescent yttrium oxide doped with Tm and Yb. *J. Am. Ceram. Soc.* ***2006****, 89 (3),* 926–931. DOI: 10.1111/j.1551-2916.2006.00845.x

[39]. Lopez, O. A.; McKittrick, J.; Shea, L. E. Fluorescence properties of polycrystalline Tm3+-activated Y3Al5O12 and Tm3+-Li+ co-activated Y3Al5O12 in the visible and near IR ranges. *J. Lumin.* **1997**, *71* (1), 1–11. DOI: 10.1016/S0022-2313(96)00123-8

[40]. Shea, L. E.; McKittrick, J.; Lopez, O. A.; Sluzky, E.; Phillips, M. L. F. Advantages of self-propagating combustion reactions for synthesis of oxide phosphors. *J. Soc. Inf. Disp.* **1997**, *5* (2**),** 117–125. DOI: 10.1889/1.1985140

[41]. Shea, L. E.; McKittrick, J.; Lopez, O. A.; Sluzky, E. Synthesis of red-emitting, small particle size luminescent oxides using an optimized combustion process. *J. Am. Ceram. Soc.* **1996**, ***79*** (12), 3257–3265. DOI: 10.1111/j.1151-2916.1996.tb08103.x

[42]. Kokubo, T. Bioactive glass ceramics: Properties and applications. *Biomaterials*. **1991**, *12* (2), 155–163. DOI: 10.1016/0142-9612(91)90194-F

[43]. Maleka, P. M.; Reddy, L.; Nkosi, T. J.; Balakrishna, A.; Kroon, R. E.; Swart, H. C.; Ntwaeaborwa, O. M. Structural and morphological characterization of photoluminescent cerium-doped near UV-blue sodium ortho-phosphate phosphors. *J. Lumin.* **2020**, *226*, 117409. DOI: 10.1016/j.jlumin.2020.117409

[44]. Ghamami, S.; Anari, S. K.; Bakhshi, M.; Lashgari, A.; Salgado-Morán, G.; Glossman-Mitnik, D. Preparation and characterization of cerium (III) doped captopril nanoparticles and study of their photoluminescence properties. *Open Chem.* **2016**, *14* (1), 60–64. DOI: 10.1515/chem-2016-0008

[45]. Kobylinska, N. G.; Dudarko, O. A.; Melnyk, I. V.; Seisenbaeva, G. A.; Kessler, V. G. Luminescence performance of cerium(III) ions incorporated into organofunctional mesoporous silica. *Microporous Mesoporous Mater.* **2020**, *305*, 110331. DOI: 10.1016/j.micromeso.2020.110331

[46]. Nie, K.; Zhou, R.; Cheng, C. -A.; Duan, X.; Hu, Z.; Mei, L.; Liu, H.; Zhang, Y.; Wang, L.; Wang, H.; Ma, X. Structure, luminescence properties and energy transfer of terbium and samarium co-doped barium based apatite phosphor with tunable emission colour. *Heliyon* **2022**, *8* (12), e12566. DOI: 10.1016/j.heliyon.2022.e12566

[47]. Verma, N.; Michalska-Domańska, M.; Ram, T.; Kaur, J.; Misra, A. K.; Dubey, V.; Dubey, N.; Tiwari, K.; Rao, M. C. Optimizing the luminescence efficiency of an europium (Eu3+) doped SrY2O4 phosphor for flexible display and lighting applications. *RSC Adv*. **2023**, *13* (29), 20217–20228. DOI: 10.1039/d3ra03199c

[48]. Demirtaş, T. T.; Kaynak, G.; Gümüşderelioğlu, M. Bone-like hydroxyapatite precipitated from 10×SBF-like solution by microwave irradiation. *Mater. Sci. Eng., C* **2015**, *49*, 713–719. DOI: 10.1016/j.msec.2015.01.057

[49]. Spanos, N.; Misirlis, D. Y.; Kanellopoulou, D. G.; Koutsoukos, P. G. Seeded growth of hydroxyapatite in simulated body fluid. *J. Mater. Sci.* **2006**, *41*, 1805–1812. DOI: 10.1007/s10853-006-2952-9

[50]. Cho, S. -B.; Nakanishi, K.; Kokubo, T.; Soga, N.; Ohtsuki, C.; Nakamura, T.; Kitsugo, T.; Yamamuro, T. Dependence of apatite formation on silica gel on its structure: Effect of heat treatment. *J. Am. Ceram. Soc.* **1995**, *78* (7), 1769–1774. DOI: 10.1111/j.1151-2916.1995.tb08887.x

[51]. Kim, H. -M.; Himeno, T.; Kokubo, T.; Nakamura, T. Process and kinetics of bonelike apatite formation on sintered hydroxyapatite in a simulated body fluid. *Biomaterials* **2005**, *26* (21), 4366–4373. DOI: 10.1016/j.biomaterials.2004.11.022

[52]. Dorozhkin, S. V. Surface reactions of apatite dissolution. *J. Colloid Interface Sci.* **1997**, *191* (2), 489–497. DOI: 10.1006/jcis.1997.4942

[53]. Dorozhkin, S. V. Inorganic chemistry of the dissolution phenomenon: The dissolution mechanism of calcium apatites at the atomic (ionic) level. *Comments Inorg. Chem.* **1999**, *20* (4-6), 285–299. DOI: 10.1080/02603599908021447

[54]. Zvicer, J.; Medic, A.; Veljovic, D.; Jevtic, S.; Novak, S.; Obradovic, B. Biomimetic characterization reveals enhancement of hydroxyapatite formation by fluid flow in gellan gum and bioactive glass composite scaffolds. *Polym. Test.* **2019**, *76*, 464–472. DOI: 10.1016/j.polymertesting.2019.04.004

Chapter 3 In vitro differentiation of pre-osteoblast like cells (MC3T3-E1) in luminescent hydroxyapatite

Abstract

We present a study investigating the osteogenic potential of rare-earth doped hydroxyapatite in a murine pre-osteoblastic cell line, aiming to assess the osteoblast differentiation effect of Yb-, Tb-, Ce-, and Eu- doped hydroxyapatite through alkaline phosphatase activity and the expression levels of osteogenic marker genes. Our findings reveal an enhancement of differentiation activity with the incorporation of rare-earth elements into the hydroxyapatite lattice. Among the rare-earth dopants assessed, europium and ytterbium exhibited higher alkaline phosphatase activity. Additionally, the gene expression of Runx2, OCN, ALP, OPN, and BMP2 was higher in the presence of these two dopants. Cathodoluminescence spectroscopy measurements revealed distinct emission peaks corresponding to Eu^{2+}/Eu^{3+} and Yb^{2+} in the hydroxyapatite doped with europium and terbium, respectively, suggesting that the incorporation of the 2+ valence ions in the hydroxyapatite lattice contributes to the enhancement of osteoblast differentiation. This research contributes valuable insights into the development of novel biomaterials with enhanced osteoinductive properties, promising advancements in bone tissue engineering and regenerative medicine.

3.1. Introduction

Hydroxyapatite (HAp) and β-tricalcium phosphate (TCP) are essential inorganic materials, constituting the primary components of robust biological tissues like bone. While HAp provides the structural integrity[1], TCP plays a crucial role in bone remodeling and regeneration.[2] Given their significance, there is immense interest in leveraging these materials for biomedical applications to fabricate artificial bone structures that not only gain host acceptance but also stimulate osteo-regeneration. HAp [$Ca_{10}(PO_4)_6(OH)_2$] is obtained either from biological sources like bovine bones[3,4] or through different synthesis methods involving calcium and phosphorus precursors[5]. It is crucial to understand how specific methods and conditions influence the biological performance, thereby impacting its stability and solubility[6]. In contrast, TCP synthesis can be achieved through high-temperature solid-state reactions, low thermal wet precipitation and thermal conversion methods.[7] It is known that the thermal conversion is not a direct synthesis method; rather, it involves the conversion of amorphous calcium phosphate[8,9,10] or calcium deficient hydroxyapatite[11,12,13] to TCP by reaching temperatures above 1023 K.[14] For this reason, synthesis of HAp involving high-temperature reactions, such as solution combustion method, often results in the formation of a mixture of HAp and TCP.[15,16,17]

Although, HAp is known to inhibit the proliferation of both human cancer cells (MGC-803, Os-732, and Bel-7402) and normal cells (L-02, MRC-5, and HaCaT)[18,19], further investigations revealed HAp does not inhibit bone cells proliferation and can even promote them[20], a property that can be affected by mixing it with other materials[21], like TCP[22], or by the incorporation of dopants[23] such as rare-earth elements.[24] Both TCP and rare-earth elements have been well-documented for inducing osteoblast differentiation.[25,26,27,28,29] In TCP, osteoblast differentiation has been related to the Ca^{2+} release[30], following the activation of the Calmodulin

and Calmodulin-dependent kinase II pathway, as described by Carey et. al..[31] On the other hand, in rare-earth ions, such as lanthanum and gadolinium, the differentiation has been linked to Wnt/β-Catenin pathways.[32,33] All these pathways activate the expression of genes associated with the osteoblast differentiation. While these studies confirm the positive influence of rare-earth elements on osteoblast differentiation, a comparative study among rare-earth dopants with varying charges has not been reported previously. In this work we present an osteogenic promotion study of hydroxyapatite doped with rare-earth elements, including europium, cerium, terbium, and ytterbium. Gene expression and ALP activity were assessed to reveal the osteogenic properties of rare-earth doped hydroxyapatite. Cathodoluminescence spectroscopy confirmed the presence and charge of the rare-earth dopants. The crystal structure and phase purity of both the undoped and doped hydroxyapatite powders were determined through Rietveld analysis. This paper discusses the formation of TCP and the alterations in the HAp lattice structure, as well as reports on the influence of the rare earth dopant on osteogenic activity.

3.2. Experimental procedure

3.2.1. HAp and HAp:RE powders synthesis

Undoped hydroxyapatite (HAp) and rare-earth doped hydroxyapatite (HAp:RE = HAp:Eu, HAp:Ce, HAp:Tb and HAp:Yb) powders were synthesized by combustion synthesis [as shown in Figure 19].[34,35,36,37,38,39,40,41,42] For the HAp, the reagents used were calcium nitrate tetrahydrate [$Ca(NO_3)_2{\cdot}4H2O$, 99%, Alfa Aesar, Ward Hill, MA], ammonium hydrogen phosphate [$(NH_4)_2HPO_4$, 98%, Alfa Aesar, Ward Hill, MA], and carbohydrazide [$CO(NHNH_2)_2$ 97%, Alfa Aesar, Ward Hill, MA]. The rare earth dopants used were europium nitrate hexahydrate [$Eu(NO_3)_3{\cdot}6H_2O$, 99.9%, Alfa Aesar, Ward Hill, MA], cerium nitrate hexahydrate [$Ce(NO_3)_3{\cdot}6H_2O$, 99.9%, Sigma Aldrich], terbium nitrate hexahydrate [$Tb(NO_3)_3{\cdot}6H_2O$, 99.9%,

Sigma Aldrich] and ytterbium nitrate hexahydrate [$Yb(NO_3)_3 \cdot 5H_2O$, 99.9%, Alfa Aesar, Ward Hill, MA].

The HAp solution was prepared by adding 26.87ml of $(NH_4)_2HPO_4$ 0.67M to 29.86ml of $Ca(NO_3)_2 \cdot 4H_2O$ 1M solution by dropwise under continues stirring. The HAp:RE solutions were prepared by dissolving 26.87 mmol of $Ca(NO_3)_2 \cdot 4H_2O$ and 1.414 mmol of RE dopant into 28.28 mL of deionized water, 25.45ml of $(NH_4)_2HPO_4$ 0.67M was added dropwise to the calcium/RE solution under continuous stirring. Then, 4.035 g of carbohydrazide was dissolved into the HAp and HAp:RE solutions and placed in a Pyrex crystallization dish and placed into a preheated furnace at 773 K until ignition occurred (within approximately 15 min). The HAp and HAp:RE powders resultant from the combustion were calcined at 873 K for 4 hours.

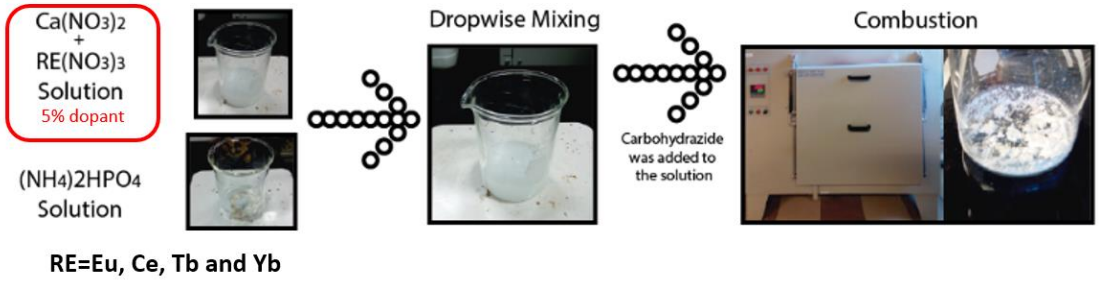

Figure 19. Synthesis Scheme of the solution combustion synthesis of HAp:RE.

3.2.2. Powder characterization

All samples were characterized with a Bruker D2 Phaser X-ray diffractometer, using CuKα radiation and a step size of 0.01° over the 2θ range of 20 to 70 degrees. Rietveld analysis of XRD data in JADE software was used to identify and quantify the percentages of the phases. Particle size distributions were determined using a Microtrac Nanotrac ULTRA dynamic light scattering (DLS) system dispersing 10 mg of powder in 100 mL of deionized water, and ultrasonicated for 10 minutes. Subsequently, the sample was allowed to stand undisturbed for approximately 5 minutes before measurement. Energy dispersive spectroscopy (EDS) was used to determine

elemental composition using an X-Max Oxford-Instruments system with a detector size of 20 mm^2. The morphology of the powders was analyzed by scanning electron microscopy (SEM) using a JEOL JIB-4500 instrument. Photoluminescence measurements were performed in a Hitachi F-4100 fluorescence spectrophotometer over a wavelength range of 200–800 nm.

3.2.3. Cell Culture

Mouse pre-osteoblast MC3T3-E1 subclone 4 cell line (CRL-2593, ATCC, Manassas, VA) were cultured in alpha-Minimum Essential Medium Eagle medium (α-MEM) (Sigma-Aldrich, St. Louis, MO), supplemented with 10% Fetal Bovine Serum (FBS, BenchMark, Gemini Bio Products), 1% v/v (Streptomycin/Penicilin, BIowest), 1% v/v L-glutamine (Sigma Aldrich, MO) and 1.5 g/l sodium bicarbonate. MC3T3-E1 cells were cultivated at 310 K humidified atmosphere containing 5% CO_2.

3.2.4. Hemolysis

The hemolysis test was performed according to the ISO 10993-4. For the Erythrocytes preparation, 25 mL of blood from an anonymous normocyte healthy human donor were extracted directly into K2-EDTA-coated Vacutainer tubes to prevent coagulation.

The blood sample was 1) centrifuged at 1750 RPM for 5 minutes at 298 K to separate the hematocrit, then 2) the supernatant was removed and 3) replaced with 150 mM NaCl solution. Steps 1), 2) and 3) were repeated once to wash the blood sample. The NaCl solution was removed following steps 1) and 2). Then, the 4) supernatant was replaced with PBS. Steps 1), 2) and 4) were repeated to wash the blood sample. The red blood cell solution (RBC) was prepared mixing 1 mL of the washed blood sample solution and 49 mL of PBS. In a 1.5 mL Eppendorf tube, 2 mg of HAp and HAp:RE powders were dispersed in 0.2 mL of RBC and placed in an incubator at 310 K for 1 hour. After incubation, the samples were centrifuged at 10,000 rpm for 5 minutes and 100

μL of supernatant from all samples were transferred to a 96-well plate. The absorbance of the samples was measured at 541 nm in a microplate reader (Multiskan GO, Thermo Scientific). To determine the percentage of hemolysis, the following formula was used: Hemolysis (%) = (absorbance at 541 nm of the sample - absorbance at 541 nm of the negative control) / (absorbance at 541 nm of the positive control - absorbance at 541 nm of the negative control) × 100. The negative control consisted of RBC, showing no hemolysis. In contrast, the positive control was RBC treated with 0.1% Triton X-100 in PBS, which induced 100% hemolysis.

According to the ASTM F756-00 standard, the materials can be classified in three different categories: hemolytic with a percentage of hemolysis over 5%, slightly hemolytic with a percentage of hemolysis between 5% and 2% , and non-hemolytic with a percentage of hemolysis below 2%.

3.2.5. Osteoblast viability assays

Pre-osteoblast cell (MC3T3-E1) viability test was performed using a colorimetric assay based on the reduction of resazurin (7-Hydroxy-3H-phenoxazin-3-one 10-oxide, sodium). 3 mg of HAp and HAp:RE were dispersed in 300 μL of α-MEM and placed in a 24-well plate. Then, 200 μL of α-MEM containing 12,500 cells were added to the 24-well plate and incubated for 24 h, 48 h and 72 h at 310 K and 5% CO_2. Consecutively, treated cells were rinsed with PBS and the cell viability test was assessed with the in vitro Cell Vitality Assay Kit (Sigma Aldrich, Eugene, OR). The negative control consisted of α-MEM with 10% C12-resazurin, while untreated cells incubated for 24 h, 48 h and 72 h at 310 K and 5% CO_2 were used as a positive control for C12-resazurin staining. The absorbance of the samples and controls were measured at 570 nm and 600 nm in the micro plate reader.

3.2.7. *In vitro* Alkaline phosphatase activity assay

The differentiation of pre-osteoblast cells was evaluated as a function of alkaline phosphatase (ALP) activity. Osteoblast MC3T3-E1 cells were differentiated for 7 days and assessed for ALP activity. 5 mg of HAp and HAp:RE were dispersed by sonication in 1 ml of PBS for 5 minutes. Then, 100 µL of this solution was added to osteoblast cells that had been seeded in a 24-well plate at a density of 3,000 cells. Then were incubated for 7 days at 310 K in a 5% CO_2 atmosphere (the osteoblast culture medium was replaced every 2 days). Subsequently, the cells were rinsed with PBS, followed by the addition of 200 µL of 5 mM p-Nitrophenyl Phosphate (p-NPP, Sigma Aldrich, St. Louis, MO) and incubated for 1 hour at 310 K in a 5% CO_2 atmosphere. 100 µL of supernatant were place in a 96-well plate and measured in microplate reader at 405nm. A solution was prepared by mixing 5 mg of ascorbic acid and 216 mg of β-glycerophosphate in 100 mL of HPLC grade water. Subsequently, 10 µL of this solution was added to a well containing only cells on day 5 of the ALP activity assay, serving as the negative control. For the positive control, cells were incubated under identical conditions. Both the positive and negative control groups were incubated without the presence of either HAp or HAp:RE.

All results were normalized by the total number of cells present on day 7 of the analysis. The number of cells was estimated indirectly by the calculation of the total protein content.

3.2.8. Gene expression of Runx2, ALP, OPN, OCN, and BMP2

To determine whether HAp or HAp:RE causes changes in the expression of genes involved in the differentiation of osteoblast (Runx2, ALP, OPN, OCN, and BMP2), quantitative polymerase chain reaction was performed (q-PCR).

3.2.9. Statistical analysis

Each experiment was conducted independently in triplicate. The results were presented as the mean ± standard deviation of three separate experiments.

3.3. Results and Discussion

3.3.1. General powder characteristics

SEM measurement of HAp:Eu sample revealed a distinctive flake-like morphology that appeared irregularly agglomerated [Figure 1(a)]. Both the pure and HAp:RE samples exhibited a unimodal particle size distribution with an average hard agglomerate diameter ranging from 90 nm to 140 nm, as depicted in Figure 1(b). Cathodoluminescence spectra of the HAp:Eu powders [Figure 3(a)] display the typical broad emission of the Eu^{2+} ions centered at 420 nm, attributed to transitions between levels $4f^{6}5d^{1}$ and $4f^{7}(^{8}S_{7/2})$[43], and the characteristic emissions of Eu^{3+} ions between 570 nm and 720 nm that correspond to transitions between levels $^{5}D_{0}$ and $^{7}F_{J}$.[44] Figures 3(b) and (c) illustrate the Ce^{3+} and Tb^{3+} emissions for the transitions $^{5}D_{0} \rightarrow {}^{7}F_{0}$ and $^{5}D_{3/2} \rightarrow {}^{7}F_{J}$ for Ce^{3+} [45,46], and $^{5}D_{3} \rightarrow {}^{7}F_{J}$ and $^{5}D_{4} \rightarrow {}^{7}F_{J}$ for Tb^{3+} .[47,48] The catholuminescence spectra shown in Figure 3(d) corresponds to the transitions of Yb^{2+} generated by a trigonal distortion of the regular octahedral crystal field of the $4f^{13}5d^{1}$ configuration.[49]

The atomic compositions of the HAp and HAp:RE samples, analyzed by energy dispersive spectroscopy, are detailed in Table 1. The results reveal that the atomic percentages of the rare-earth ions in the HAp:RE samples are approximately 1.3. The HAp sample exhibits a Ca/P ratio of 1.6, which is below the stoichiometric Ca/P ratio of HAp (1.67) but above the stoichiometric Ca/P ratio for TCP (1.50). This discrepancy is attributed to the HAp sample being a mixture of HAp and TCP, as illustrated in Figure 3(f). While the HAp:RE samples are similarly composed of a mixture of HAp and TCP, their Ca/P ratios (HAp:Eu 1.39, HAp:Ce 1.41, HAp:Tb 1.39, and

HAp:Yb 1.36) fall below both the stoichiometric Ca/P ratio of HAp and the Ca/P ratio of TCP, indicating that the HAp:RE samples are Ca-deficient.

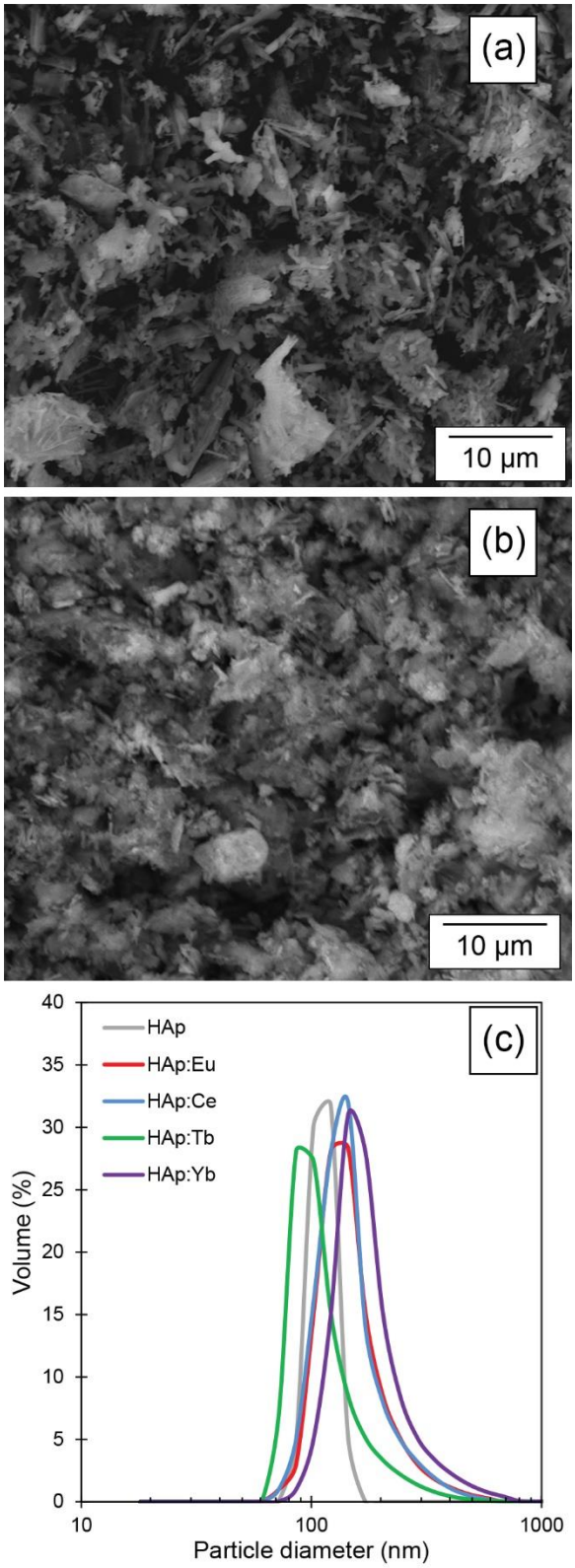

Figure 20. Scanning electron micrograph of (a) HAp and (b) HAp:Eu. Particle size distribution of the combustion-synthesized (c) HAp and HAp:RE samples

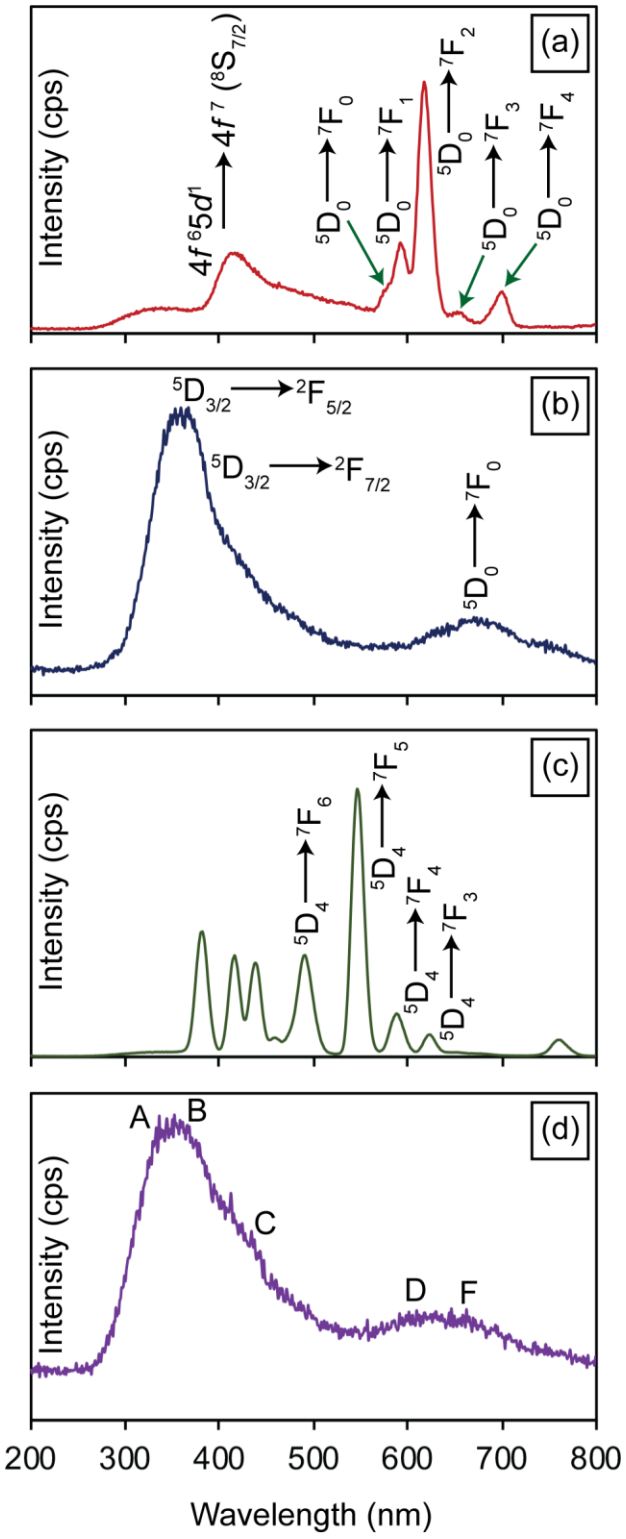

Figure 21. Cathodoluminescence spectra of the (a) HAp:Eu, (b) HAp:Ce, (c) HAp:Tb samples, and (d) HAp:Yb scaffolds with the relevant A-E peaks produced by electronic interconfigurational transitions of the Yb2+ ions.

Table 4. Atomic Composition of the HAp and HAp:RE from Energy-Dispersive Spectroscopy Measurements.

	O (at.%)	P (at.%)	Ca (at.%)	RE (at.%)	Ca/P
HAp	55.24	17.21	27.55	NA	1.60
HAp:Eu	56.78	17.52	24.38	1.32	1.39
HAp:Ce	57.55	17.07	24.11	1.27	1.41
HAp:Tb	55.45	18.05	25.17	1.33	1.39
HAp:Yb	58.13	17.18	23.43	1.26	1.36

Based on the XRD analysis [Figure 3(a-e)], undoped and doped HAp samples exhibit high crystallinity, characterized by distinct peaks corresponding to hexagonal HAp ($P6_3/m$, no. 176) and beta tri-calcium phosphate (TCP), PDF card #00-055-0898, according to the HAp and TCP Bragg's position, respectively. Rietveld refinement was employed to characterize the crystal structure and the crystallographic phases present in the HAp and HAp:RE. Crystal structure models were taken from Palache et al.[50] for HAp, and Calvo and Gopal[51] for TCP. The resulting Rietveld refinement plots, shown in Figure 3 (a-e), exhibit a notable concordance between observed and calculated diffraction patterns for the HAp and HAp:RE samples. The structure models for HAp and TCP proved to be well-suited for refining the diffraction patterns, yielding goodness-of-fit values (GOF) close to or below 1.5. Figure 3 (f) shows the phase fractions obtained by the quantitative analysis of the Rietveld refinement, revealing that the HAp sample contains approximately 23 wt.% TCP. In addition, the weight percentage of TCP increases to around 40% in the HAp:RE samples. In previous research[52,49], we reported that TCP forms when HAp is synthesized by combustion synthesis. This happens because the combustion temperature goes beyond the formation temperature for TCP (973 K), a thermal phase transformation that has been

observed mainly in calcium-deficient HAp.[14,53] The increment in the formation of TCP observed for HAp:RE samples is related to the decrease of calcium content[54], as shown in Table 1, caused by the incorporation of the rare-earth ions in the HAp lattice.

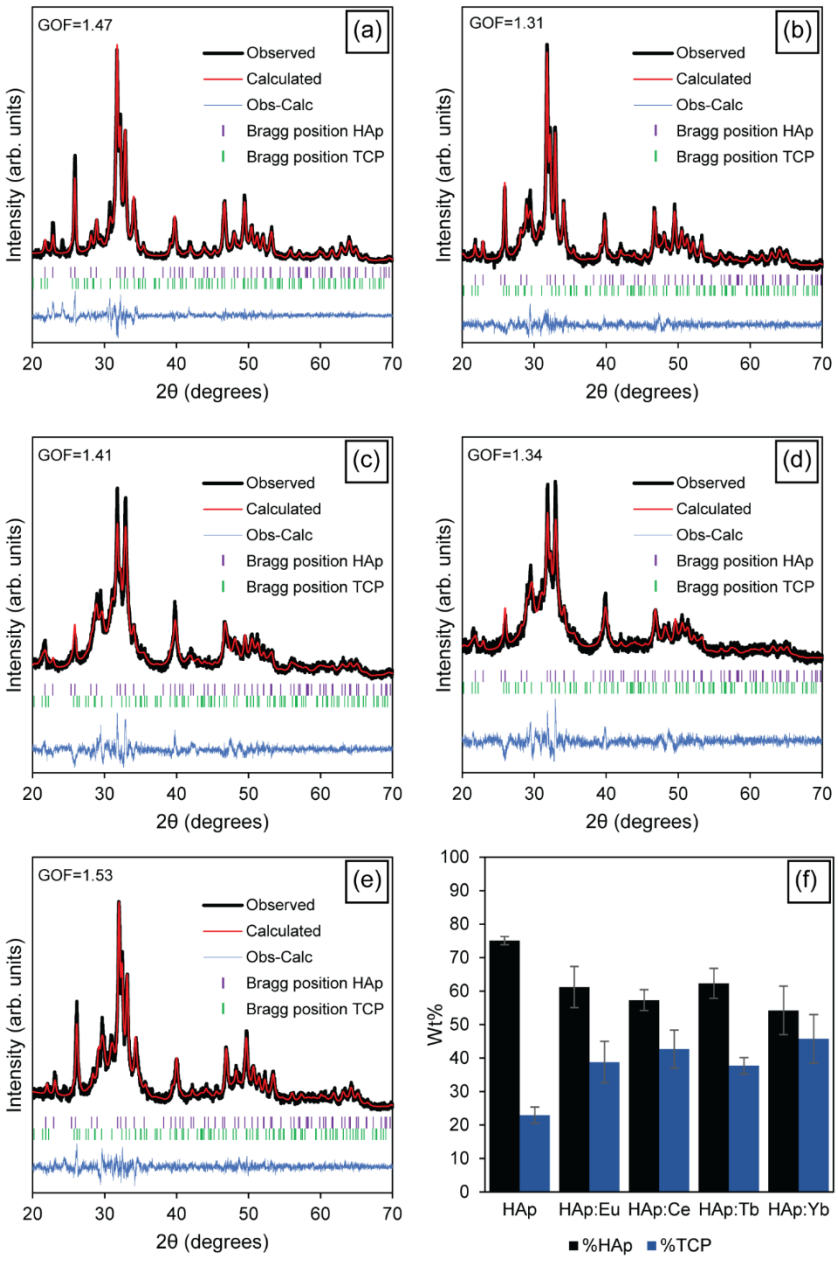

Figure 22. Rietveld refinement of the X-ray diffraction pattern of (a) HAp, (b) HAp:Eu, (c) HAp:Ce, (d) HAp:Tb and (e) HAp:Yb samples. (f) Phase fractions (as weight percent) obtained from full pattern Rietveld refinement of HAp and HAp:RE X-ray diffraction patterns.

HAp possesses two crystallographic Ca^{2+} sites. Ca(I) sites are coordinated to nine oxygen atoms belonging to six PO_4^{3-} groups, while Ca(II) sites are coordinated to seven oxygens, six from PO_4^{3-} groups and one from an OH^- ion. Rare-earth ions have shown preference for substituting the Ca(II) sites[55,56,57,58,59], and typically have a higher charge than calcium ions (e.g., Eu^{3+}, Ce^{3+}, Tb^{3+}, and Yb^{3+} compared to Ca^{2+}). The difference in the charges results in either: i) the removal of two or more calcium ions from the crystal lattice, or ii) the loss of a proton from the OH^- ion to give an O^{2-} ion[60], both aimed at maintaining charge balance in the HAp lattice. Ignjatović et al.[61] suggest that the incorporation of rare-earth ions (such as Gd^{3+}, Yb^{3+}, Tm^{3+}, and Eu^{3+}) decreases the lattice parameters of the HAp, resulting from the reduction in the Ca-O interatomic distance caused by the loss of a proton in the OH^- ion. However, the lattice parameters of both HAp and HAp:RE, as shown in Table 2, indicate an increase in lattice parameter *a*, and a slight contraction in lattice parameter *c* for the HAp phase.

Table 5. Refined lattice parameters of HAp and HAp:RE samples, and reference lattice constants for HAp (PDF# 00-009-0432) and TCP (PDF# 00-055-0898).

	HAp		TCP	
	a (nm)	c (nm)	a (nm)	c (nm)
Reference	**0.9.41800**	**0.688400**	**1.04264**	**3.737600**
HAp	0.943143	0.688443	1.04296	3.736510
HAp:Eu	0.944613	0.687352	1.04479	3.748965
HAp:Ce	0.943654	0.688383	1.04433	3.749114
HAp:Tb	0.943524	0.687250	1.04463	3.749685
HAp:Yb	0.943979	0.688124	1.04448	3.748121

We suggest this variation is attributed to calcium vacancies, as fewer positively charged ions are present to balance the negative charges of phosphate and hydroxide ions. The negative

charge can generate the Coulomb repulsion force with the negative charge of PO_4^{3-}, which can push PO_4^{3-} away from its original position, resulting in local lattice expansion. An expansion in the unit cell that has been observed in other ceramics by the formation of cation vacancies.[62,63,64] In contrast, the lattice parameters *a* and *c* for the TCP phase in the HAp:RE increased as a result of the incorporation of rare-earth ions. Previous studies suggest that the substitution of Ca^{2+} in TCP by rare-earth ions (i.e. Er^{3+}, Yb^{3+}, Sm^{3+}, Eu^{3+} or Gd^{3+}) can occur at the Ca(4) sites[65,66], and the substitution by trivalent ions results in the expansion of the unit cell through increases in the a- and c-axis.[65,67,68,69]

3.3.2 Hemolysis assay

As seen in Figure 4, neither the HAp nor HAp:RE were able to induce a percentage of hemolysis greater than 5%, which is the upper limit allowed by the ASTM F756-00 standard to be considered as non-hemolytic or slightly hemolytic material.[70] Negative control has a 2.9% of hemolysis, suggesting that this percentage of hemolysis corresponds to the natural rupture of the erythrocyte membrane by the conditions of the hemolysis assay (such as temperature, centrifuge parameters or wash procedure). Indeed, rare-earth elements such as europium, praseodymium, or gadolinium, have been shown to be safe for red blood cells, with hemolysis percentages below 4%.[71,72,73] However, even if the percentage of hemolysis of a material is below an accepted limit, such as 5%, it can still be influenced by other factors such as the duration of contact with blood[74], and the intended use of the material.[75]

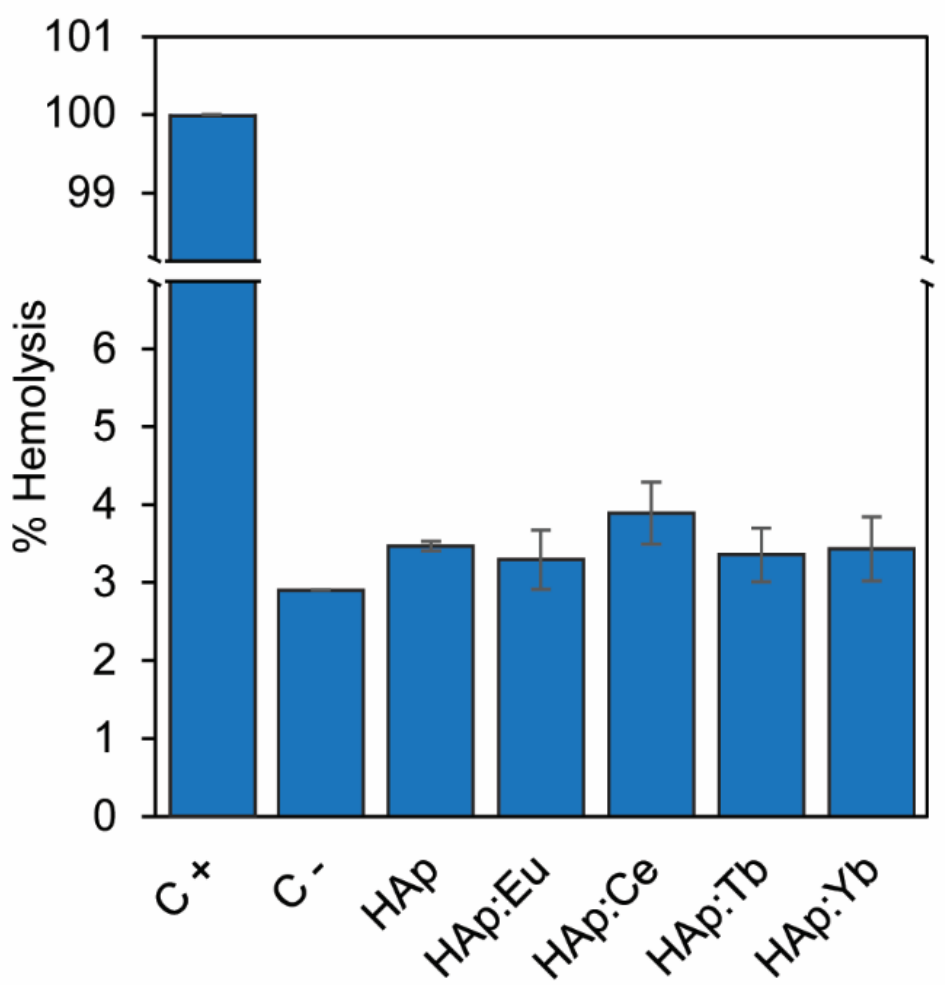

Figure 23. Hemocompatibility assay of HAp and HAp:RE samples.

3.3.3 Pre-osteoblast cell viability assay

The growth of MC3T3-E1 mouse pre-osteoblast cells cultured indirectly with the HAp and HAp:RE was quantitatively measured. Figure 5 shows the cell viability percentage of the HAp and HAp:RE samples. The cell viability analysis revealed that by the end of day 1, the viability percentage of the HAp and HAp:RE samples surpassed the viability of the control (>100%). Although the proliferation levels were high on day 1, by the end of day 2, the differences in cell viability were indistinguishable among all samples compared to the control, hovering around ~99%.%. These values remained constant by the end of day 3. Our results show that cell

proliferation is not influenced by the presence of rare-earth dopants, such as europium, cerium, terbium, or ytterbium. These findings are consistent with previously reported results for HAp doped with europium, samarium, gadolinium, or ytterbium.[76,77,78]

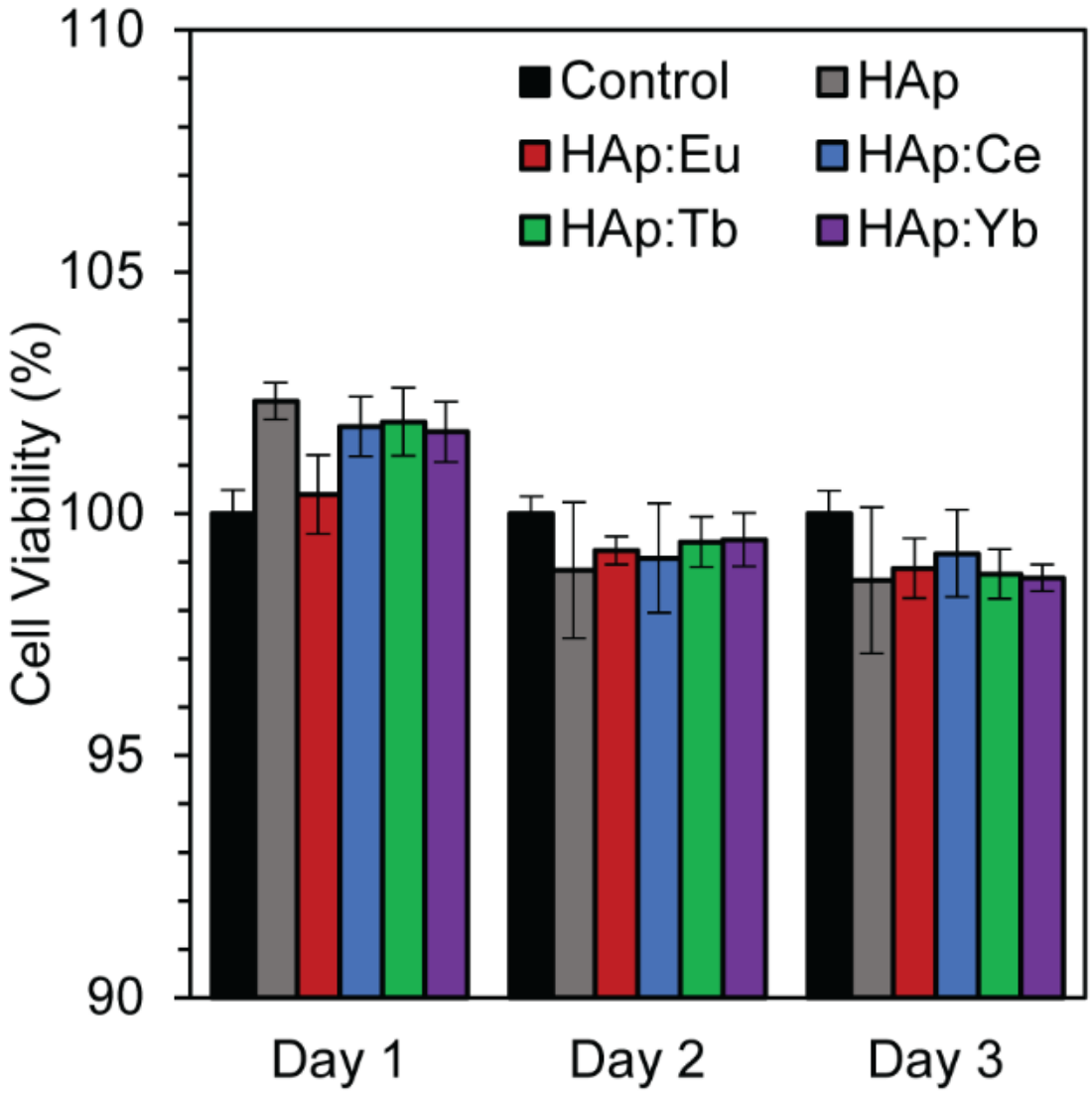

Figure 24. Cell viability assessment (resazurin-based) of HAp and HAp:RE in murine pre-osteoblasts MC3T3-E1 cell lines.

3.3.4 Pre-osteoblast differentiation

The observed increase in ALP activity, shown in Figure 6, indicates a stimulatory effect of HAp and HAp:RE on the initiation of bone formation. However, HAp:RE samples demonstrated higher ALP activity compared to HAp alone. This enhancement in ALP activity can be attributed to the presence of rare-earth dopants and their higher content of TCP, as demonstrated by Jin et al.[30], who showed that despite having a similar pore structure, TCP exhibited superior ALP activity compared to HAp. Additionally, Li et al.[79] showed that doping bioactive glass with europium enhanced their osteogenic differentiation properties. In both cases, the presence of TCP and the use of rare-earth dopants follow pathways that activate the expression of osteoblast genes.[27,33,80] In Figure 7, we illustrate the expression of osteoblast genes, particularly Runx2, OCN, ALP, OPN, and BMP2. Our findings reveal a coordinated upregulation of multiple osteogenic markers during osteoblast differentiation induced by these materials. Consistent with osteoblast differentiation, the expression levels of Runt-related transcription factor 2 (Runx2), osteocalcin (OCN), alkaline phosphatase (ALP), and osteopontin (OPN) were prominently elevated, reflecting their essential functions in bone matrix mineralization and extracellular matrix remodeling in the presence of these materials. Moreover, the robust activation of the bone morphogenetic protein 2 (BMP2) signaling pathway further supported the osteogenic program, highlighting BMP2's potent inducer role in driving osteoblast differentiation upon exposure to HAp doped with europium and ytterbium. Within the HAp:RE samples, HAp:Eu and HAp:Yb exhibited higher ALP activity in all assays, suggesting that the incorporation of rare-earth ions with charge 2+ have a positive effect in the differentiation of murine pre-osteoblastic cell.

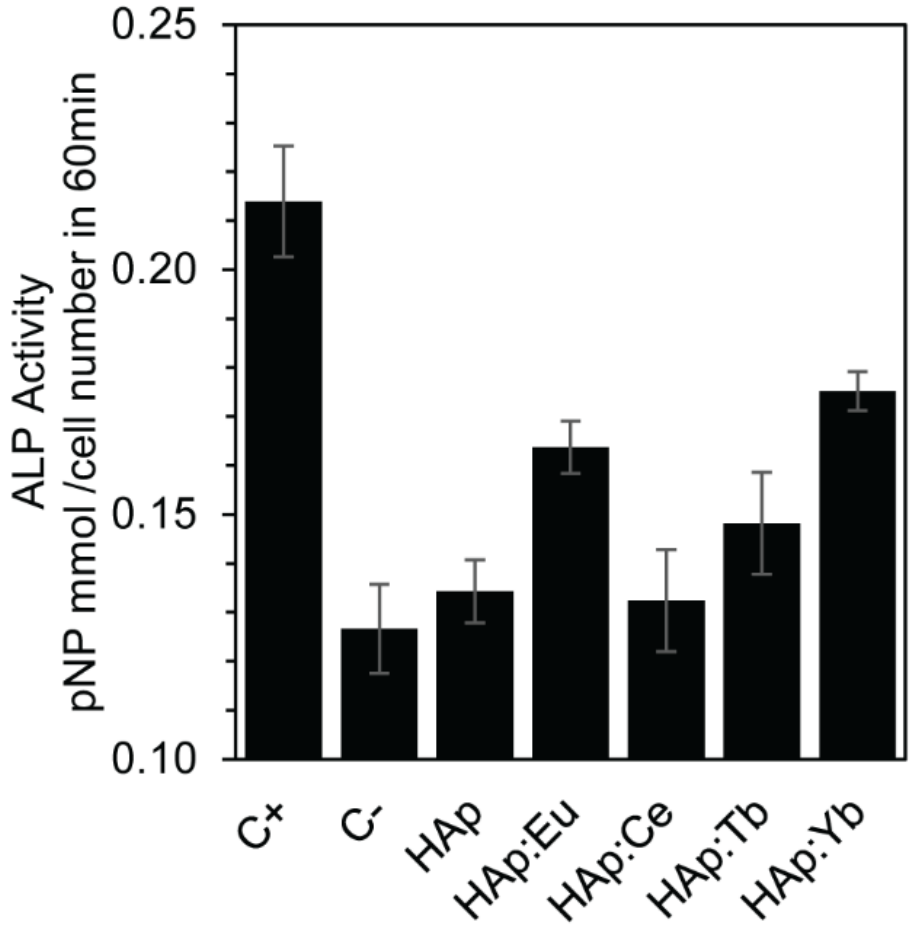

Figure 25. ALP activity of osteoblast cultured with HAp and HAp:RE samples for 7 days.

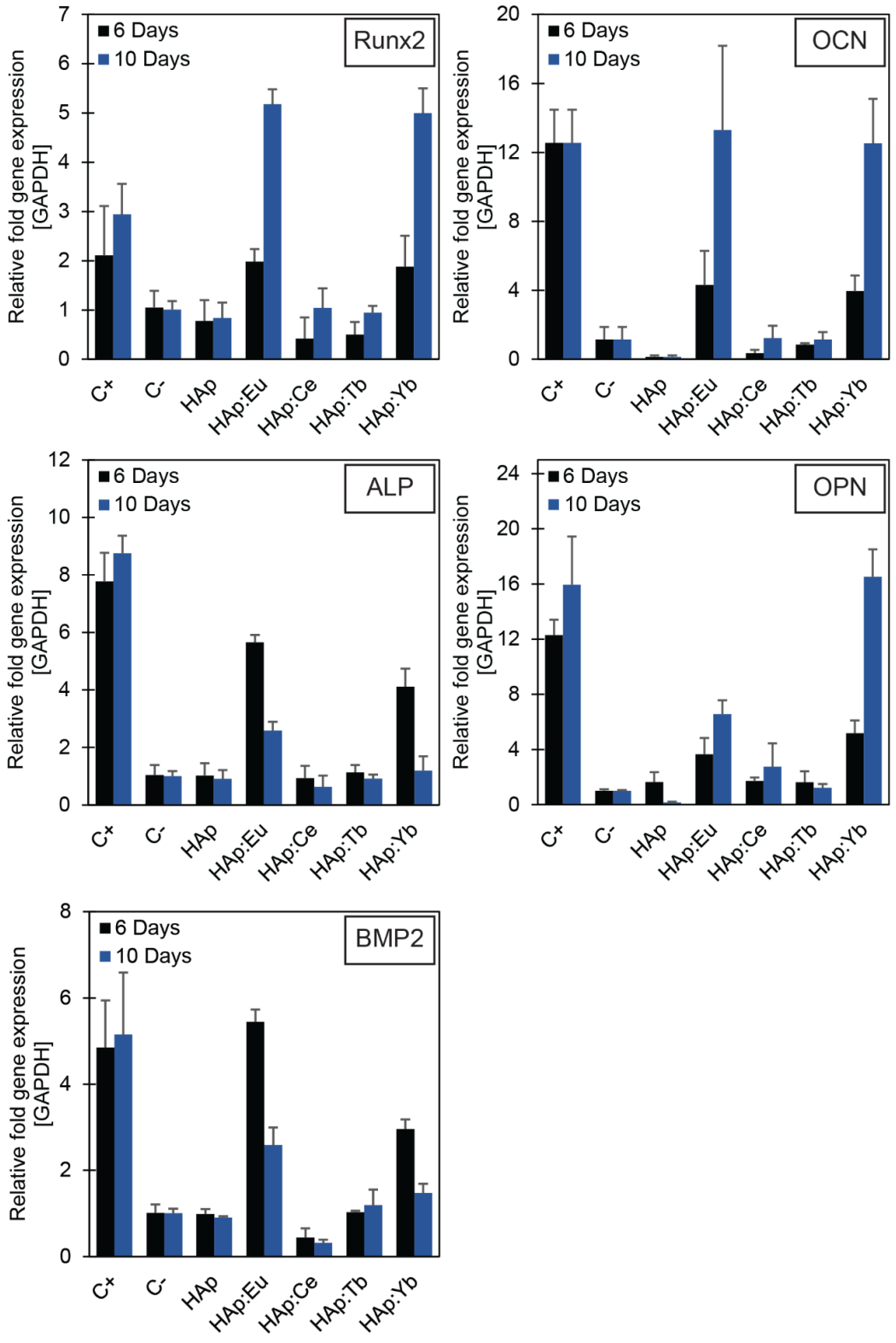

Figure 26. Real-time PCR gene expression on the HAp and HAp:RE samples at days 6 and 10. The bone-associated genes, including Runx2, OCN, ALP, OPN, BMP2, were assessed.

3.4. Conclusions

Undoped (HAp) and rare-earth doped hydroxyapatite (HAp:RE) was synthesized by solution combustion synthesis, with europium, cerium, terbium, and ytterbium as dopants. The powders reveal a flake-like morphology and a particle size distribution ranging from 90 nm to 140 nm. The presence of the rare-earth ions in the HAp:RE powders was confirmed by cathodoluminescence spectroscopy, exhibiting the corresponding emissions of Eu^{2+} (412 nm), Eu^{3+} (578, 592, 617, 655 and 698 nm), Ce^{3+} (360 nm), Tb^{3+} (493, 547, 588 and 623 nm), and Yb^{2+}(350 and 620 nm). EDS measurements reveal Ca/P ratios of 1.60%, 1.39%, 1.41%, 1.39%, and 1.36% for HAp, HAp:Eu, HAp:Ce, HAp:Tb, and HAp:Yb, respectively, indicating calcium deficiency in the HAp:RE samples. X-ray diffraction analysis confirms high crystallinity in both HAp and HAp:RE samples, with distinct peaks corresponding to hexagonal hydroxyapatite and beta tri-calcium phosphate. The quantitative analysis of Rietveld refinement indicates that the HAp:RE samples exhibit a higher weight percentage of TCP (around 40%) compared to the HAp sample (approximately 23%). The formation of TCP during the combustion synthesis of HAp occurs due to the elevated combustion temperature surpassing the TCP formation temperature (973 K). Furthermore, the increased formation of TCP in HAp:RE samples is attributed to the reduced calcium content, as indicated by EDS analysis, resulting from the incorporation of rare-earth ions into the HAp lattice. HAp and HAp:RE exhibit an increase in lattice parameter *a* and a slight contraction in lattice parameter *c* for the HAp phase. This variation is likely attributed to calcium vacancies, resulting in fewer positively charged ions available to balance the negative charges of phosphate and hydroxide ions. Consequently, the negative charge generated may lead to Coulomb repulsion force with neighboring ions, causing them to be pushed away from their original positions, thereby resulting in local lattice expansion.

Our studies demonstrate that neither HAp nor HAp:RE exhibited a percentage of hemolysis exceeding 5%, which is the upper limit defined by the ASTM F756-00 standard. Despite initial differences in cell viability of MC3T3-E1 mouse pre-osteoblast cells cultured with HAp and HAp:RE on day 1, all samples exhibited comparable viability levels by the end of day 2 and throughout day 3. These findings suggest that the addition of rare-earth dopants does not adversely affect cell proliferation. Both HAp and HAp:RE demonstrate a stimulating effect on bone formation initiation, with HAp:RE showing higher ALP activity attributed to rare-earth dopants and increased TCP content. These findings suggest that rare-earth dopants and TCP activate pathways associated with osteoblast differentiation, enhancing the osteogenic potential of HAp:RE materials.

Acknowledgements

Chapter 3, in part, is currently being prepared for submission for publication of the material. Martinez-Pallares, Fabian; Juarez-Moreno, Karla; Vazquez, Lidia; Herrera-Zaldivar, Manuel; Graeve, Olivia. The dissertation author was the primary researcher and author of this chapter.

Reference

[1]. Sopyan, I.; Mel, M.; Ramesh, S.; Khalid, K. A. Porous hydroxyapatite for artificial bone applications, *Sci. Technol. Adv. Mater.* **2007**, 8 (1–2), 116-123.DOI: 10.1016/j.stam.2006.11.017.

[2]. Kikuchi, N.; Yoshioka, T.; Arai, N.; Hyodo, K.; Kanamori, A.; Yamazaki, M. A radiological study of bone remodeling with two different types of porous β-tricalcium phosphate in humans. *Sci. Rep.* **2020**, 10, 19886. DOI: 10.1038/s41598-020-77011-3

[3]. Odusote, J. K.; Danyuo, Y.; Baruwa, A. D.; Azeez, A. A. Synthesis and characterization of hydroxyapatite from bovine bone for production of dental implants. *J. Appl. Biomater. Funct. Mater.* **2019**, 17 (2), 2280800019836829. DOI: 10.1177/2280800019836829

[4]. Arokiasamy, P.; Al Bakri Abdullah, M. M.; Abd Rahim, S. Z.; Luhar, S.; Sandu, A. V.; Jamil, N. H.; Nabiałek, M. Synthesis methods of hydroxyapatite from natural sources: A review, *Ceram. Int.* **2022**, 48 (11), 14959-14979, DOI: 10.1016/j.ceramint.2022.03.064.

[5]. Mohd Pu'ad, N.A.S.; Abdul Haq, R. H.; Mohd Noh, H.; Abdullah, H. Z.; Idris, M.I.; Lee, T. C. Synthesis method of hydroxyapatite: A review, *Mater. Today: Proc.* **2020**, 29 (1), 233-239, DOI: 10.1016/j.matpr.2020.05.536.

[6]. DileepKumar, V. G.; Sridhar, M. S.; Aramwit, P.; Krut'ko, V. K.; Musskaya, O. N.; Glazov, I. E.; Reddy, N. A review on the synthesis and properties of hydroxyapatite for biomedical applications. *J Biomater Sci Polym Ed*, 2022, 33 (2), 229-261. DOI: 10.1080/09205063.2021.1980985.

[7]. Bohner, M.; Le Gars Santoni, B.; Döbelin, N. β-tricalcium phosphate for bone substitution: Synthesis and properties, *Acta Biomater.* **2020**, 113, 23-41.DOI: 10.1016/j.actbio.2020.06.022.

[8]. Maciejewski, M.; Brunner, T. J.; Loher, S. F.; Stark, W. J.; Baiker, A. Phase transitions in amorphous calcium phosphates with different Ca/P ratios, *Thermochim. Acta*, **2008**, 468, 75–80. DOI: 10.1016/j.tca.2007.11.022

[9]. Bohner, M.; Brunner, T. J.; Doebelin, N.; Tang, R.; Stark, W.J.; Effect of thermal treatments on the reactivity of nanosized tricalcium phosphate powders, *J. Mater. Chem.* **2008**, 18, 4460–4467. DOI: 10.1039/B804314K

[10]. Vecbiskena, L.; Gross, K. A.; Riekstina, U.; Yang, T.C.K. Crystallized nano-sized alpha-tricalcium phosphate from amorphous calcium phosphate: microstructure, cementation and cell response, *Biomed. Mater.* **2015**, 10 (2), 025009. DOI: 10.1088/1748-6041/10/2/025009

[11]. Alshemary, A. Z.; Goh, Y. F.; Shakir, I.; Hussain, R.; Synthesis, characterization and optical properties of chromium doped β-Tricalcium phosphate, *Ceram. Int.* **2015**, 41 (1), 1663–1669. DOI: 10.1016/j.ceramint.2014.09.107

[12]. Deng , C.; Yao, Q.; Feng, C.; Li, J.; Wang, L.; Cheng, G.; Shi, M.; Chen, L.; Chang, J.; Wu, C.; 3D printing of bilineage constructive biomaterials for bone and cartilage regeneration, *Adv. Funct. Mater.* **2017**, 27 (36), 1703117. DOI: 10.1002/adfm.201703117

[13]. Gomes, S.; Vichery, C.; Descamps, S.; Martinez, H.; Kaur, A.; Jacobs, A.; Nedelec, J.-M.; Renaudin, G. Cu-doping of calcium phosphate bioceramics: from mechanism to the control of cytotoxicity, *Acta Biomater.* **2018**, 65, 462–474. DOI: 10.1016/j.actbio.2017.10.028

[14]. Destainville, A.; Champion, E.; Bernache-Assollant, D.; Laborde, E. Synthesis, characterization and thermal behavior of apatitic tricalcium phosphate, *Mater. Chem. Phys.* **2003**, 80 (1), 269-277. DOI: 10.1016/S0254-0584(02)00466-2.

[15]. Canillas, M.; Rivero, R.; García-Carrodeguas, R.; Barba, F.; Rodríguez, M. A. Processing of hydroxyapatite obtained by combustion synthesis, *Bol. Soc. Esp. Ceram. Vidrio*, **2017**, 56 (5), 237-242, DOI: 10.1016/j.bsecv.2017.05.002.

[16]. Batista, H. A.; Silva, F. N.; Lisboa, H. M.; Costa, A. C. F. M. Modeling and optimization of combustion synthesis for hydroxyapatite production, *Ceram. Int.* **2020**, 46 (8), Part B, 11638-11646. DOI: 10.1016/j.ceramint.2020.01.194.

[17]. Graeve, O. A.; Kanakala, R.; Madadi, A.; Williams, B. C.; Glass, K. C. Luminescence variations in hydroxyapatites doped with Eu2+ and Eu3+ ions. Biomaterials, **2010**, 31 (15), 4259–4267. DOI: 10.1016/j.biomaterials.2010.02.009

[18]. Han, Y.; Li, S.; Cao, X.; Yuan, L.; Wang, Y.; Yin, Y.; Qiu, T.; Dai, H.; Wang, X. Different Inhibitory Effect and Mechanism of Hydroxyapatite Nanoparticles on Normal Cells and Cancer Cells in Vitro and in Vivo. *Sci. Rep.* **2014**, 4, 7134. DOI: 10.1038/srep07134

[19]. Liu, Z.-S.; Tang, S.-L.; Ai, Z.-L. Effects of Hydroxyapatite Nanoparticles on Proliferation and Apoptosis of Human Hepatoma BEL-7402 Cells. *World J. Gastroenterol*. **2003**, 9 (9), 1968–1971. DOI: 10.3748/wjg.v9.i9.1968

[20]. Cai, Y.; Liu, Y.; Yan, W.; Hu, Q.; Tao, J.; Zhang, M.; Shi, Z.; Tang, R. Role of Hydroxyapatite Nanoparticle Size in Bone Cell Proliferation. *J. Mater. Chem.* **2007**, 17 (36), 3780. DOI: 10.1039/b705129h

[21]. Zhao, B.; Xu, H.; Gao, Y.; Xu, J.-Z.; Yin, H.-M.; Xu, L.; Li, Z.-M.; Song, X. Promoting Osteoblast Proliferation on Polymer Bone Substitutes with Bone-like Structure by Combining Hydroxyapatite and Bioactive Glass. *Mater. Sci. Eng. C*, **2019**, 96, 1–9. DOI: 10.1016/j.msec.2018.11.006

[22]. Sulaiman, S. B.; Keong, T. K.; Cheng, C. H.; Saim, A. B.; Idrus, R. B. Tricalcium phosphate/hydroxyapatite (TCP-HA) bone scaffold as potential candidate for the formation of tissue engineered bone. *Indian J. Med. Res.* **2013**, 137 (6), 1093–1101.

[23]. Ressler, A.; Žužić A.; Ivanišević, I.; Kamboj, N.; Ivanković, H. Ionic substituted hydroxyapatite for bone regeneration applications: A review, Open Ceram., **2021**, 6, 100122, DOI: 10.1016/j.oceram.2021.100122.

[24]. Kolmas, J.; Groszyk, E.; Kwiatkowska-Różycka, D. Substituted Hydroxyapatites with Antibacterial Properties. *BioMed Res. Int.* **2014**, 1–15. https://doi.org/10.1155/2014/178123.

[25]. Shalash, M. A.; Rahman, H .A.; Azim, A. A.; Neemat, A. H.; Hawary, H. E.; Nasry, S. A. Evaluation of Horizontal Ridge Augmentation Using Beta Tricalcium Phosphate and Demineralized Bone Matrix: A Comparative Study. *J. Clin. Exp. Dent.* **2013**, e253-e259. DOI: 10.4317/jced.51244.

[26]. Kim, W.; Kim, G. Collagen/bioceramic-based composite bioink to fabricate a porous 3D hASCs-laden structure for bone tissue regeneration. *Biofabrication*, **2019**, 12 (1), 015007. DOI: 10.1088/1758-5090/ab436d.

[27]. Lu, H.; Zhou, Y.; Ma, Y.; Xiao, L.; Ji, W.; Zhang, Y.; Wang, X. Current Application of Beta-Tricalcium Phosphate in Bone Repair and Its Mechanism to Regulate Osteogenesis. *Front. Mater.* **2021**, 8:698915. DOI: 10.3389/fmats.2021.698915

[28]. Gao, J.; Feng, L.; Chen, B.; Fu, B.; Zhu, M. The role of rare earth elements in bone tissue engineering scaffolds - A review, *Composites, Part B*, **2022**, 235, 109758. DOI: 10.1016/j.compositesb.2022.109758.

[29]. Cacciotti, I. Cationic and Anionic Substitutions in Hydroxyapatite. In *Handbook of Bioceramics and Biocomposites*, 1st ed.; Springer, Cham, 2016; pp. 145-211. DOI. 10.1007/978-3-319-12460-5_7

[30]. Jin, P.; Liu, L.; Cheng, L.; Chen, X.; Xi, S.; Jiang, T. Calcium-To-Phosphorus Releasing Ratio Affects Osteoinductivity and Osteoconductivity of Calcium Phosphate Bioceramics in Bone Tissue Engineering. *BioMed. Eng. OnLine*, **2023**, 22 (1). DOI: 10.1186/s12938-023-01067-1.

[31]. Cary, R. L.; Waddell, S.; Racioppi, L.; Long, F.; Novack, D. V.; Voor, M. J.; Sankar, U. Inhibition of $Ca2^{+}$/calmodulin-dependent Protein Kinase Kinase 2 Stimulates Osteoblast Formation and Inhibits Osteoclast Differentiation. *J. Bone Mineral Res.* **2013**, 28, 1599–1610. DOI: 10.1002/jbmr.1890

[32]. Hu, H.; Zhao, P.; Liu, J.; Ke, Q.; Zhang, C.; Guo, Y.; Ding, H. Lanthanum phosphate/chitosan scaffolds enhance cytocompatibility and osteogenic efficiency via the Wnt/β-catenin pathway. *J Nanobiotechnol.* **2018**, 16, 98. DOI: 10.1186/s12951-018-0411-9

[33]. Liao, F.; Peng, X. Y.; Yang, F.; Ke, Q. F.; Zhu, Z. H.; Guo, Y. P. Gadolinium-doped mesoporous calcium silicate/chitosan scaffolds enhanced bone regeneration ability, Mater. Sci. Eng. C, 2019, 104, 109999. DOI: 10.1016/j.msec.2019.109999.

[34]. Novitskaya, E.; Manheim, A.; Herrera, M.; Graeve, O. A. Effect of oxygen vacancies on the mechanoluminescence response of magnesium oxide. *J. Phys. Chem. C* **2021**, *125* (1) 854–864. DOI: 10.1021/acs.jpcc.0c07674

[35]. Novitskaya, E., Kelly, J. P., Bhaduri, S., Graeve, O. A. A review of solution combustion synthesis: An analysis of parameters controlling powder characteristics. *Int. Mater. Rev.* **2021**, *66* (3), 188–214. DOI: 10.1080/09506608.2020.1765603

[36]. Kanakala, R.; Escudero, R.; Rojas-George, G.; Ramisetty, M.; Graeve, O. A. Mechanisms of combustion synthesis and magnetic response of high-surface-area hexaboride compounds. *ACS Appl. Mater. Interfaces* **2011**, *3* (4), 1093–1100. DOI: 10.1021/am1012276

[37]. Kanakala, R.; Rojas-George, G.; Graeve, O. A. Unique preparation of hexaboride nanocubes: A first example of boride formation by combustion synthesis. *J. Am. Ceram. Soc.* ***2010****, 93 (10),* 3136–3141. DOI: 10.1111/j.1551-2916.2010.03853.x

[38]. Sinha, K.; Pearson, B.; Casolco, S. R.; Garay, J. E.; Graeve, O. A. Synthesis and consolidation of $BaAl_2Si_2O_8$:Eu. Development of an integrated process for luminescent smart ceramic materials. *J. Am. Ceram. Soc.* **2009**, *92* (11), 2504–2511. DOI: 10.1111/j.1551-2916.2009.03242.x

[39]. Graeve, O. A.; Varma, S.; Rojas-George, G.; Brown, D. R.; Lopez, E. A. Synthesis and characterization of luminescent yttrium oxide doped with Tm and Yb. *J. Am. Ceram. Soc.* ***2006****, 89 (3),* 926–931. DOI: 10.1111/j.1551-2916.2006.00845.x

[40]. Lopez, O. A.; McKittrick, J.; Shea, L. E. Fluorescence properties of polycrystalline Tm^{3+}-activated $Y_3Al_5O_{12}$ and Tm^{3+}-Li^+ co-activated $Y_3Al_5O_{12}$ in the visible and near IR ranges. *J. Lumin.* **1997**, *71* (1), 1–11. DOI: 10.1016/S0022-2313(96)00123-8

[41]. Shea, L. E.; McKittrick, J.; Lopez, O. A.; Sluzky, E.; Phillips, M. L. F. Advantages of self-propagating combustion reactions for synthesis of oxide phosphors. *J. Soc. Inf. Disp.* **1997**, *5* (2**),** 117–125. DOI: 10.1889/1.1985140

[42]. Shea, L. E.; McKittrick, J.; Lopez, O. A.; Sluzky, E. Synthesis of red-emitting, small particle size luminescent oxides using an optimized combustion process. *J. Am. Ceram. Soc.* **1996**, ***79*** (12), 3257–3265. DOI: 10.1111/j.1151-2916.1996.tb08103.x

[43]. Dorenbos, P. Energy of the first $4f^7 \rightarrow 4f^6 5d$ transition of Eu^{2+} in inorganic compounds. *J. of Lumin.* ***2003****,* 104 (4), 239-260. DOI: 10.1016/S0022-2313(03)00078-4

[44]. Du, P.; Yu, J. S. Photoluminescence and cathodoluminescence properties of Eu3+ ions activated AMoO4 (A=Mg, Ca, Sr, Ba) phosphors. *Mater. Res. Bull.* **2015**, 70, 553-558. DOI: 10.1016/j.materresbull.2015.05.022

[45]. Ghamami, S.; Anari, S. K.; Bakhshi, M.; Lashgari, A.; Salgado-Morán, G.; Glossman-Mitnik, D. Preparation and Characterization of Cerium (III) Doped Captopril

Nanoparticles and Study of their Photoluminescence Properties. *Open Chem.* **2016**, 14 (1), 60-64. DOI: 10.1515/chem-2016-0008

[46]. Kobylinska, N. G.; Dudarko, O.; Melnyk, I. V.; Seisenbaeva, G. A.; Kessler, V. G. Luminescence performance of Cerium(III) ions incorporated into organofunctional mesoporous silica. *Microporous and Mesoporous Mater*. **2020**, 305, 110331. DOI: 10.1016/j.micromeso.2020.110331

[47]. Silversmith, A. J.; Boye, D. M.; Brewer, K. S.; Gillespie, C. E.; Lu, Y.; Campbell, D. L. $^5D_3 \rightarrow {}^7F_J$ emission in terbium-doped sol–gel glasses. *J. Lumin.* **2006**, 121 (1), 14–20. DOI: 10.1016/j.jlumin.2005.09.009

[48]. Zhao, W.; An, S.; Fan, B.; Li, S. Cathodoluminescence properties of Tb3+-doped Na3YSi2O7 phosphors. *Appl. Phys. A: Mater. Sci. Process.* **2013**, 111 (2), 601–604. DOI: 10.1007/s00339-012-7271-1

[49]. Zavala, L. A.; Fernández, P.; Novitskaya, E.; Díaz, J. N.; Herrera, M.; Graeve, O. A. Interconfigurational and intraconfigurational transitions of Yb2+ and Yb3+ ions in hydroxyapatite: A cathodoluminescence study. *Acta Mater*. **2017**, 135, 35-43. DOI: 10.1016/j.actamat.2017.06.003

[50]. Palache, C.; Berman, H.; Frondel, C. *Dana's system of mineralogy*, 7th ed., II, 1124, John Wiley and Sons, New York. 1951.

[51]. Calvo, C.; Gopal R. The crystal structure of Whitlockite from the Palermo Quarry, *Am. Mineral.* **1975**, 60, 120-133. http://www.minsocam.org/ammin/AM60/AM60_120.pdf (accesed 2023-01-26)

[52]. Zavala-Sanchez, L. A.; Hirata, G. A.; Novitskaya, E.; Karandikar, K.; Herrera, M.; Graeve, O. A. Distribution of Eu2+ and Eu3+ Ions in Hydroxyapatite: A Cathodoluminescence and Raman Study, *ACS Biomater. Sci. Eng.* **2015**, 1 (12), 1306-1313. DOI: 10.1021/acsbiomaterials.5b00378

[53]. Frasnelli, M.; Sglavo, V. M. Flash sintering of tricalcium phosphate (TCP) bioceramics. *J. Eur. Ceram. Soc*. **2018**, 38 (1), 279–285. DOI: 10.1016/J.JEURCERAMSOC.2017.08.004

[54]. Kannan, S.; Goetz-Neunhoeffer, F.; Neubauer, J.; Ferreira, J. M. F. Ionic Substitutions in Biphasic Hydroxyapatite and β-Tricalcium Phosphate Mixtures: Structural Analysis by Rietveld Refinement. *J. Am. Ceram. Soc.* **2017**, 91 (1), 1–12. DOI: 10.1111/j.1551-2916.2007.02117.x

[55]. Ardanova, L. I.; Get'Man, E. I.; Loboda, S. N.; Prisedsky, V. V.; Tkachenko, T. V.; Marchenko, V. I.; Antonovich, V. P.; Chivireva, N. A.; Chebishev, K. A.; Lyashenko, A. S. Isomorphous substitutions of rare earth elements for calcium in synthetic hydroxyapatites. *Inorg. Chem.* **2010**, 49 (22), 10687–10693. DOI: 10.1021/ic1015127

[56]. Fleet, M. E.; Liu, X.; Pan Y. Site Preference of Rare Earth Elements in Hydroxyapatite [Ca10(PO4)6(OH)2], *J. Solid State Chem.* **2000**, 149 (2), 391-398, DOI: 10.1006/jssc.1999.8563.

[57]. Phatai, P.; Futalan, C. M.; Utara, S.; Khemthong, P.; Kamonwannasit, S. Structural characterization of cerium-doped hydroxyapatite nanoparticles synthesized by an ultrasonic-assisted sol-gel technique. *Results in Phys*. **2018**, 10, 956–963. DOI: 10.1016/J.RINP.2018.08.012

[58]. Vinicius Beserra dos Santos, M.; Bastos Nogueira Rocha, L.; Gomes Vieira, E.; Leite Oliveira, A.; Oliveira Lobo, A.; de Carvalho, M.A.M.; Anteveli Osajima, J.; Cavalcanti Silva-Filho, E. Development of Composite Scaffolds Based on Cerium Doped-Hydroxyapatite and Natural Gums—Biological and Mechanical Properties. *Materials*, **2019**, 12, 2389. DOI: 10.3390/ma12152389

[59]. Ciobanu, C.S.; Nica, I. C.; Dinischiotu, A.; Iconaru, S. L.; Chapon, P.; Bita, B.; Trusca, R.; Groza, A.; Predoi, D. Novel Dextran Coated Cerium Doped Hydroxyapatite Thin Films. *Polymers.* **2022**, 14, 1826. DOI: 10.3390/polym14091826

[60]. Hosseini, S. M.; Drouet, C.; Al-Kattan, A.; Navrotsky, A. Energetics of lanthanide-doped calcium phosphate apatite. *Am Miner*. **2014**, 99, 2320-2327. DOI: 10.2138/am-2014-4930

[61]. Ignjatović, N. L.; Mančić, L.; Vuković, M.; Stojanović, Z.; Nikolić, M. G.; Škapin, S.; Jovanović, S.; Veselinović, L.; Uskoković, V.; Lazić, S.; Marković, S.; Lazarević, M. M.; Uskoković, D. P. Rare-earth (Gd^{3+},Yb^{3+}/Tm^{3+}, Eu^{3+}) co-doped hydroxyapatite as magnetic, up-conversion and down-conversion materials for multimodal imaging. *Sci Rep*. **2019**, 9, 16305. DOI: 10.1038/s41598-019-52885-0

[62]. Kim, Y. I.; Jeong, M.; Byun, J.; Yang, S.-H. .; Choi, W.; Jang, W.-S. .; Jang, J.; Lee, K.; Kim, Y.; Lee, J.; Lee, E.; Kim, Y.-M. . Atomic-Scale Identification of Invisible Cation Vacancies at an Oxide Homointerface. *Mater. Today Phys.* **2021**, 16, 100302. DOI: 10.1016/j.mtphys.2020.100302.

[63]. Wu, H.; Pi, J.; Zhou, D.; Wang, Q.; Long, Z.; Qiu, J. Effect of Cation Vacancy on Lattice and Luminescence Properties in CsPbBr3 Quantum Dots. *Ceram. Int.* **2022**, 48 (3), 3383–3389. DOI: 10.1016/j.ceramint.2021.10.114.

[64]. Muhammad, R.; Khesro, A. Influence of A-Site Nonstoichiometry on the Electrical Properties of BT-BMT. *J. Am. Ceram. Soc.* **2016**, 100 (3), 1091–1097. DOI: 10.1111/jace.14684

[65]. Wiglusz, R. J.; Pozniak, B.; Zawisza, K.; Pazik, R. An up-converting HAP@β-TCP nanocomposite activated with Er^{3+}/Yb^{3+} ion pairs for bio-related applications. *RSC Adv*. **2015**, 5 (35), 27610–27622. DOI: 10.1039/c5ra00675a

[66]. Orlova, A.I.; Orlova, M.P.; Solov'eva, E.M. Loginova, E. E.; Demarin, V. T.; Kazantsev, G. N.; Samoilov, S. G.; Stefanovskii, S. V. Lanthanides in phosphates with the structure

of whitlockite mineral [analog of β-Ca3(PO4)2]. *Radiochemistry*, **2006**, 48 (6), 561–567. DOI: 10.1134/S1066362206060038

[67]. Piccirillo, C.; Alessio Adamiano; David Maria Tobaldi; Montalti, M.; Manzi, J.; Paula; Panseri, S.; Montesi, M.; Sprio, S.; Tampieri, A.; Iafisco, M. Luminescent Calcium Phosphate Bioceramics Doped with Europium Derived from Fish Industry Byproducts. *J. Am. Ceram. Soc.* **2017**, 100 (8), 3402–3414. DOI: 10.1111/jace.14884.

[68]. Silva, F. R. O.; Lima, N. B.; Yoshito, W. K.; Bressiani, A. H. A.; Gomes, L. Development of Novel Upconversion Luminescent Nanoparticle of Ytterbium/Thulium–Doped Beta Tricalcium Phosphate. *J. Lumin.* **2017**, 187, 240–246. DOI: 10.1016/j.jlumin.2017.03.029

[69] Salmon, R.; Parent, C.; Hagenmuller, P.; Lazoriak, B.I.; Golubev, V.N. Distribution of Eu3+ ions in whitlockite-type Ca3-xEu2x/3(PO4)2 orthophosphates. *Eur. J. Solid State Inorg. Chem.* **1989**, 26 (4), 455-463.

[70]. ASTM International. *Standard Practice for Assessment of Hemolytic Properties of Materials*; ASTM F756-00; West Conshohocken, PA, 2010. DOI: 10.1520/F0756-00

[71]. Zhang, M.; Ma, S.; Xu, K.; Chu, P.K. Corrosion resistance of praseodymium-ion-implanted TiN coatings in blood and cytocompatibility with vascular endothelial cells. *Vacuum*, **2015**, 117, 73–80. DOI: 10.1016/j.vacuum.2015.04.014.

[72]. Laranjeira, M. S.; Moço, A.; Ferreira, J.; Coimbra, S.; Costa, E.; Santos-Silva, A.; Ferreira, P. J.; Monteiro, F. J. Different hydroxyapatite magnetic nanoparticles for medical imaging: Its effects on hemostatic, hemolytic activity and cellular cytotoxicity. *Colloids Surf. B*, **2016**, 146, 363–374. DOI: 10.1016/j.colsurfb.2016.06.042

[73]. Barbosa, A. A.; Júnior, S. A.; Mendes, R. L.; de Lima, R. S.; de Vasconcelos Ferraz, A. Multifunctional Hydroxyapatite with Potential for Application in Theranostic Nanomedicine. *Mater. Sci. Eng. C*, **2020**, 116, 111227. https://doi.org/10.1016/j.msec.2020.111227.

[74]. Shapira, Y.; Vaturi, M.; Sagie, A. Hemolysis associated with prosthetic heart valves: a review. *Cardiol . Rev*. **2009**, 17 (3), 121–124. DOI: 10.1097/CRD.0b013e31819f1a83

[75]. Zhao, X.; Yu, Y.; Zhao, L.; Xu, J.; He, T.; Lin, Z.; Zhang, Y. The red blood cell damage after long-term exposure to shear stresses. *J. Artif. Organs*. **2022**, 25 (4), 298–304. DOI: 10.1007/s10047-022-01326-3

[76]. Frumosu, F.; Iconaru, S.L.; Predoi, D. Europium concentration effect of europium doped hydroxyapatite on proliferation of osteoblast cells. *Dig. J. Nanomater. Biostruct.* **2011**, 6, 1859–1865.

[77]. Sathishkumar, S.; Louis, K.; Shinyjoy, E.; Gopi, D. Tailoring the Sm/Gd-Substituted Hydroxyapatite Coating on Biomedical AISI 316L SS: Exploration of Corrosion Resistance, Protein Profiling, Osteocompatibility, and Osteogenic Differentiation for

Orthopedic Implant Applications. *Ind. Eng. Chem. Res.* **2016**, 55 (22), 6331–6344. DOI: 10.1021/acs.iecr.5b04329.

[78]. Albalwi, H. A.; El-Naggar, M. E.; Taleb, M. A.; Kalam, A.; Alghamdi, N. A.; Mostafa, M. S.; Salem, S.; Afifi, M. Medical application of Ternary Nanocomposites of Hydroxyapatite/ ytterbium oxide/graphene oxide: potential bone tissue engineering and antibacterial properties. *J. Mater. Res. Technol.* **2022**. 4834-4845 DOI: 10.1016/j.jmrt.2022.04.106.

[79]. Li, F.; Wang, M.; Pi, G.; Lei, B. Europium Doped Monodispersed Bioactive Glass Nanoparticles Regulate the Osteogenic Differentiation of Human Marrow Mesenchymal Stem Cells. *J. Biomed. Nanotechnol.* **2018**, 14 (4), 756–764. DOI: 10.1166/jbn.2018.2504

[80]. Duan, P.; Bonewald, L. F. The role of the wnt/β-catenin signaling pathway in formation and maintenance of bone and teeth, *Intl. J. Biochem. Cell. Biol.* **2016**, 77 (A), 23-29. DOI: 10.1016/j.biocel.2016.05.015.